Doctoral theses at NTNU, 2018:321

Sathiyaraj Kandhasamy

Molten Carbonate Electrolyte Based Thermocell for High Temperature Waste Heat Recovery

NTNU
Norwegian University of
Science and Technology

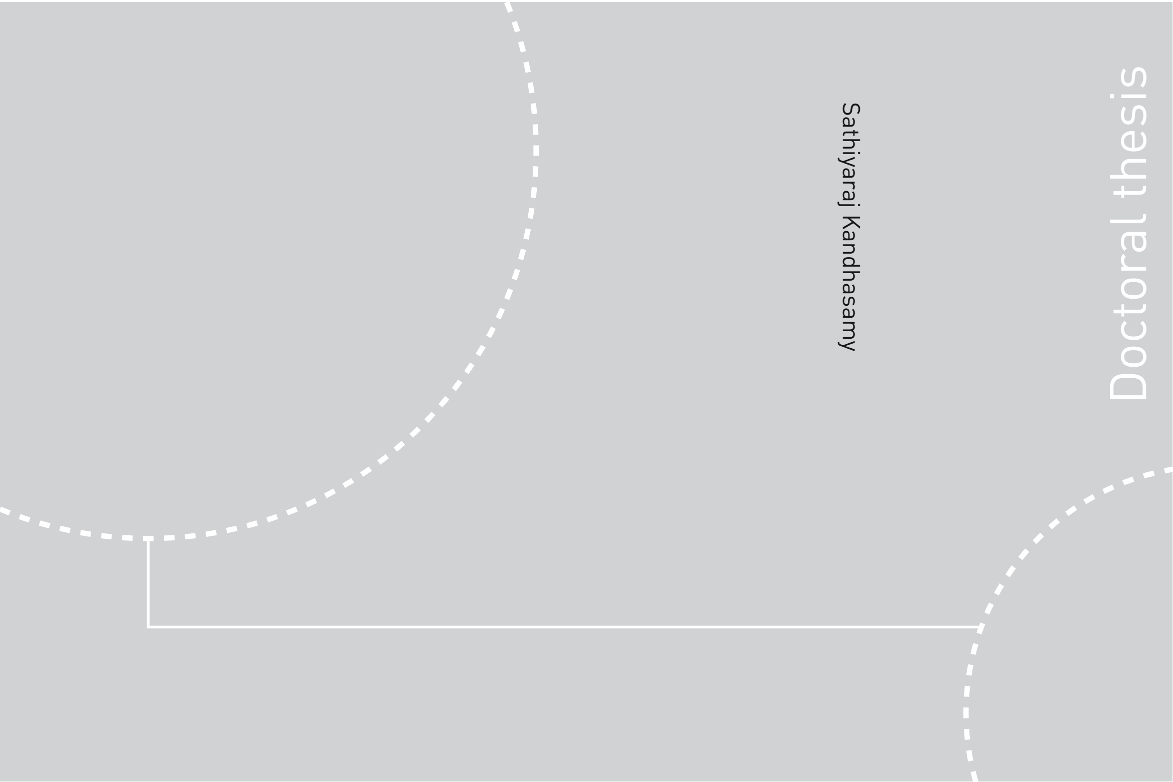

Doctoral theses at NTNU, 2018:321

NTNU
Norwegian University of Science and Technology
Thesis for the Degree of
Philosophiae Doctor
Faculty of Natural Sciences
Department of Materials Science and
Engineering

NTNU

ISBN 978-82-326-3432-3 (printed ver.)
ISBN 978-82-326-3433-0 (electronic ver.)
ISSN 1503-8181

NTNU
Norwegian University of
Science and Technology

Sathiyaraj Kandhasamy

Molten Carbonate Electrolyte Based Thermocell for High Temperature Waste Heat Recovery

Thesis for the Degree of Philosophiae Doctor

Trondheim, October 2018

Norwegian University of Science and Technology
Faculty of Natural Sciences
Department of Materials Science and Engineering

NTNU
Norwegian University of
Science and Technology

NTNU
Norwegian University of Science and Technology

Thesis for the Degree of Philosophiae Doctor

Faculty of Natural Sciences
Department of Materials Science and Engineering

© Sathiyaraj Kandhasamy

ISBN 978-82-326-3432-3 (printed ver.)
ISBN 978-82-326-3433-0 (electronic ver.)
ISSN 1503-8181

Doctoral theses at NTNU, 2018:321

Printed by NTNU Grafisk senter

Preface

This thesis has been submitted to the Department of Materials Science and Engineering, Faculty of Natural Sciences, Norwegian University of Science and Technology (NTNU) in partial fulfilment for the degree of Philosophiae Doctor (PhD). This thesis contains the results of the research carried out at the Department of Materials Science and Engineering at the Norwegian University of Science and Technology (NTNU) from 2015 to 2018. The presented research was performed under supervision of Geir Martin Haarberg (Professor, NTNU) as main supervisor, and Signe Kjelstrup (Professor, NTNU) and Asbjørn Solheim (Senior Scientist, SINTEF) as co-supervisors. This work was funded by the Research Council of Norway as a part of the research project "Sustainable and Energy Efficient Electrochemical Production and Refining of Metals (SUPREME)" project no. 228296 under ENERGIX program. This project was also supported by the industrial partners Hydro Aluminium, Boliden, Glencore, and Permascand.

The thesis is written as a collection of papers, with some already published and others are intended for publication at a later stage. But all the work has been presented at various international conferences and at meetings where industry partners attended. The list of co-authors contributed to the work has been mentioned in all the individual papers in Chapter 3. All the experimental work was conducted by me, except the Laser Flash Analysis (LFA) included in paper 3 (Chapter 3.3). The LFA analysis was performed by Anne Støre (Research Engineer, SINTEF). All the writings and data processing have been performed by myself. The co-authors have contributed by regular scientific discussions and provided input and strong comments to improve the manuscripts.

Trondheim, 3rd October 2018
Sathiyaraj Kandhasamy

Acknowledgements

I would like to express my sincere appreciation to all those who have contributed to this thesis.

First, I would like to express my sincere gratitude to my main supervisor Prof. Geir Martin Haarberg, for believing in me and offering this PhD opportunity. Beside his excellent guidance and scientific discussions, I have also enjoyed the trips with him. Also, a special thank goes to him for providing me the chances to take part in several conferences. I would like to extend my thanks to my co-supervisors Prof. Signe Kjelstrup and Dr. Asbjørn Solheim for valuable contributions, suggestions, and discussions, which helped me to be ever progressive. I should also say a big thank you to all my supervisors for their trust and freedom to execute my ideas, meantime they never forgot to share their experience and to provide the essential inputs.

I wish to thank Anne Støre for extensive support in performing the Laser Flash Analysis.

I would like to express appreciation to members of my research group Wenting Xu, Babak Khalaghi and Mats Jensen for both scientific and social discussions, and timely help in the laboratory.

I am thankful to Marit Takla Børset, former PhD at the Department of Chemistry for sharing her experience in handling the experiment. I must also thank Prof. Odne Stokke Burheim for his discussions at the initial stage of this project.

I want to thank the technical and administrative staff, present and former, at the Department of Materials Science and Engineering, and technical staff at SINTEF industries for the support during this PhD study. I would also like to thank all my colleagues and friends at the Department of Materials Science and Engineering. I wish to appreciate the staffs at the mechanical and glass workshops for their valuable contribution to fabricate the experimental setup.

I wish to acknowledge the Research Council of Norway for financial support of the research project "Sustainable and Energy Efficient Electrochemical Production and Refining of Metals (SUPREME)" project no. 228296. My sincere thanks to the industrial partners Hydro Aluminium, Boliden, Glencore and Permascand for supporting this project and the plant tours during the project meetings.

To my friends scattered around the world, I express my gratitude for standing my side during the hard times of my life with unconditional friendship and well-wishes. I grateful to my former professors for constant support and advice.

Last but not least, I express my deepest gratitude to my beloved family. My parents, without their support and dedication I could not have come this far. To my wife, Sathyapriya for her encouragement and patience throughout the studies, which made me productive. My little daughter, Retanya for blasting away my stress and cheering me up with smiles and fun.

Summary

Industrial processes for the production of metals and alloys by metallurgical and electrochemical methods generate a lot of waste heat due to irreversible losses. This waste heat could be used as a power source to produce electricity. An inexpensive molten carbonate electrolyte based thermocell demonstrated the possibility to use this waste heat as a power source. A thermocell is an electrochemical cell with two symmetrical electrodes placed in an electrolyte solution, but a difference in temperature is established between the electrodes. The temperature difference creates a potential difference between the electrodes by ion migration in the electrolyte, and electrical energy may be generated. The ion-conducting molten carbonate electrolyte with two symmetrical gas ($CO_2|O_2$) electrodes in the thermocell delivers a high Seebeck coefficient (~ 1 mV/K). It shows the advantage to harvest industrial waste heat at high temperatures and utilize the available CO_2 rich off-gases from metal producing industries. In this thesis, the molten carbonate thermocell components were further optimized to enhance the Seebeck coefficient and power conversion efficiency, which was not studied systematically before.

First, the flow rate of the gas supply to the electrodes and content of solid oxide in the molten electrolyte mixture were optimized. The dispersion of solid oxide in the molten carbonate was found to reduce the heat flux and enhance the conditions for thermoelectric conversion. The change in Seebeck coefficient was reported for various ratios of eutectic $(Li,Na)_2CO_3$ and dispersed solid oxide MgO and for varying gas ($CO_2|O_2$) flow rates to the electrode/electrolyte interfaces.

The surface charge of the dispersed solid oxide plays a crucial role in thermocell behavior. So, the change in electrical and thermal conductivities of the electrolyte mixtures dispersed with a different surface area of MgO were measured. AC impedance spectroscopy technique was used to measure the electrical conductivity (σ) of the electrolyte mixture at 550 °C by constructing a conductivity cell with capillary electrodes. A simple heat flux DSC was used to measure the thermal conductivity (λ) of molten electrolyte with solid oxide mixture for the first time. The determined thermal and electrical conductivities and thermocell Seebeck coefficient were used to estimate the figure of merit. The electrolyte mixture dispersion with a larger surface area of solid MgO provides a better (σ/λ) ratio and enhanced figure of merit (ZT) of 1.1. The ZT was comparable to the semiconductor thermoelectric materials.

The thermocell performance was also investigated with various selected solid oxides dispersed in the electrolyte mixture. The thermal and chemical stability of the dispersed solid oxides and the electrolyte mixtures were systematically analyzed. The solid oxides of Al_2O_3 and $LiAlO_2$ showed a significant chemical reactivity to the carbonate melt compared to MgO and CeO_2, and subsequent changes on the thermocell Seebeck coefficient was experienced. The electrolyte containing the MgO and $LiAlO_2$ gave a Seebeck coefficient of -1.8 mV/K at Soret equilibrium (after 100 h), which are -1.6 (MgO) and -0.9 ($LiAlO_2$) mV/K at initial time. Thus, the solid MgO with larger surface area offered the better conditions for the thermoelectric conversion and high chemical stability.

The thermo-physical and physicochemical properties of the electrolyte mixture may be tuned to reduce the liquidus temperature to ~ 400 °C in order to operate the molten carbonate thermocells below 500 °C (liquidus temperature of $(Li,Na)_2CO_3$). The multi-component (ternary and quaternary) carbonates mixtures were studied to achieve a low liquidus temperature, by mixing the molten (K and Ca) carbonate and LiF additives into binary $(Li,Na)_2CO_3$. Still, the Seebeck coefficient of the thermocells remains larger (-1.5 mV/K) for the multi-component carbonates electrolyte mixture.

In the above mentioned preliminary experiments, a metallic gold was used as the current collector for the gas ($CO_2|O_2$) electrodes to avoid the formation of interference oxide layers during operation. Finally, for further reduction in energy generation cost, an inexpensive and stable alternative metal current collector was identified to replace the gold. The present compositions of the electrolyte mixture and electrode gas of the thermocell were analogous to the cathode side half-cell of the molten carbonate fuel cell (MCFC). So, in this study the suitability of the MCFC's nickel-based cathodes to operate the molten carbonate thermocell was investigated. Thus, in this thesis a thermocell with non-critical and inexpensive molten carbonate-based electrolyte mixtures with reversible ($CO_2|O_2$) gas electrodes was demonstrated to recover the high temperature (> 400 °C) waste heat to produce electricity.

Contents

Chapter 1 Introduction..1

1.1 Thermocell 1

1.2 Importance of molten salt thermocell 2

1.3 Molten salt thermocells – A literature review 3

1.3.1 Materials selection for molten salt thermocells 3
1.3.2 Electrolytes for molten salt thermocell 4
1.3.3 Electrodes for Molten salt thermocell...21
1.3.4 Molten salt thermocell design...23
1.3.5 Evaluation of the molten salt thermocell performance 24
1.3.6 Summary...26

1.4 Aim and outline of the thesis...26

Chapter 2 Experimental 29

2.1 Laboratory thermocell operation...29

2.1.1 Gas electrode fabrication 29
2.1.2 Electrolyte preparation..32
2.1.3 Thermocell setup...32
2.1.4 Seebeck coefficient measurement...33
2.1.5 Power output measurement...34

2.2 Materials characterization 35

2.2.1 Structural and phase analysis - XRD 35
2.2.2 Melting point and thermal stability – DSC/TGA...37
2.2.3 Solid oxide particle size 37
2.2.4 Surface area of the solid oxides – BET...38
2.2.5 Electrode surface morphology – SEM 39
2.2.6 Solid oxides distribution in the electrolyte mixture – EDS............................40

2.3 Transport properties........*41*

2.3.1 Thermal conductivity – DSC........41

2.3.2 Thermal conductivity - LFA........42

2.3.3 Electrical conductivity - AC impedance spectroscopy........43

Chapter 3 Results and Discussion........47

3.1 Paper 1........*47*

Influence of Electrode Gas Flow Rate and Solid Oxide Ratio in Electrolyte on the Seebeck Coefficient of Molten Carbonate Thermocell........47

3.1.1 Introduction........48

3.1.2 Theoretical considerations........49

3.1.3 Experimental........50

3.1.4 Results and discussion........52

3.1.5 Conclusions........59

3.2 Paper 2........*61*

Electrolyte Melt Compositions for Low Temperature Molten Carbonate Thermocell........61

3.2.1 Introduction........62

3.2.2 Experimental........63

3.2.3 Results and discussion........66

3.2.4 Conclusions........75

3.2.5 Supporting information........76

3.3 Paper 3........*79*

Thermocell Electrolyte Mixture with Molten Carbonates and Solid MgO. Seebeck Coefficient and Figure of Merit........79

3.3.1 Introduction........80

3.3.2 Experimental........81

3.3.3 Results and Discussion........86

3.3.4 Conclusions........97

3.3.5 Supporting information........98

3.4 Paper 4........*101*

Thermocell Performance and Physicochemical Properties of the Molten Carbonate Electrolyte Mixtures Dispersed with Different Solid Oxides........101

3.4.1 Introduction........102

3.4.2 Experimental........103

3.4.3 Results and discussion........105

3.4.4 Conclusions ... 119

3.5 Paper 5 ... 121

Gas Electrodes with Nickel Based Metallic Current Collector for Molten Carbonate Electrolyte Thermocells ... 121

3.5.1 Introduction ... 122

3.5.2 Experimental ... 124

3.5.3 Result and discussion ... 127

3.5.4 Conclusions ... 136

3.5.5 Supporting information ... 137

Chapter 4 Suggestions for Future Work ... 139

Chapter 5 Conclusions ... 141

Bibliography ... 143

List of Figures ... 157

List of Tables ... 161

Conferences and Publications ... 163

Appendix A ... 165

Theory of molten carbonate thermocells ... 165

Chapter 1 Introduction

The constant increase in global requirement of electrical energy, demands to use all the renewable energy sources for electricity generation. The abundant availability of the waste heat in the environment may have a significant effect on the global warming. However, this heat can be used in thermoelectric conversion to produce power. The *thermoelectric conversion* is known since the discovery of *Seebeck effect* in 1821 [1]. A thermal regenerative system arranged with two identical electrodes at different temperatures in an electrolyte solution could facilitate this purpose, is called as *thermogalvanic / thermocell / thermo-electrochemical / non-isothermal cells*.

1.1 Thermocell

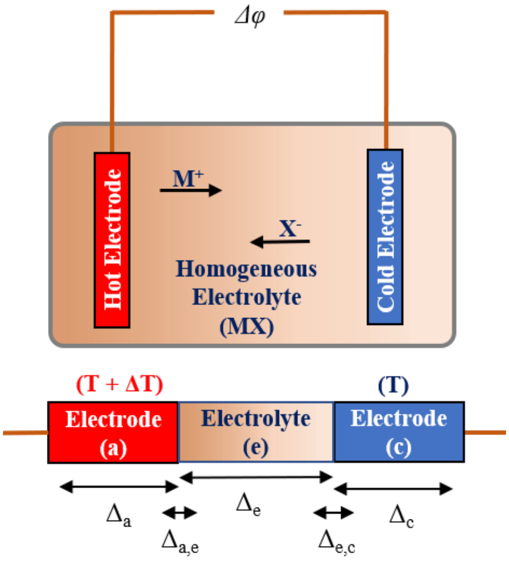
Δφ
Hot Electrode
M+
X-
Homogeneous Electrolyte (MX)
Cold Electrode
(T + ΔT)
(T)
Electrode (a)
Electrolyte (e)
Electrode (c)
Δa
Δa,e
Δe
Δe,c
Δc

Figure 1.1.1 (Top) Schematic representation of thermocell and **(bottom)** five subsystems of thermocell and the notation used for transport properties.

A thermocell is identical to an electrochemical cell, where two symmetrical electrodes are maintained at different temperatures but placed in the same electrolyte solution (**Figure 1.1.1**). General representation of the thermocell is $\mathrm{Electrode(T)|Electrolyte|Electrode(T + \Delta T)}$, where (T) is the average cell temperature and $(\Delta\mathrm{T})$ the temperature difference between the electrodes [2, 3]. The temperature difference between the electrodes set up an ionic diffusion in the electrolyte to create a concentration gradient, which leads to a potential difference between the electrodes and is called *thermoelectric potential* $(\Delta\varphi)$ [4]. Upon the establishment of the temperature difference the diffusion of the ions available near to the hot electrode is spontaneous, this immediate potential difference is an *initial state thermoelectric potential*. However, the ions located away from the hot electrode will respond slowly and take a long time to attain the steady state concentration gradient in the homogeneous electrolyte [4, 5]. The ionic inter-diffusion to reach the steady concentration gradient (no flux of matter then) in the electrolyte is *Soret effect* [6]. The steady state is called as *Soret equilibrium*. The *steady state thermoelectric potential* will differ from the initial state potential.

The measured thermoelectric potential (equation 1.1) is the sum of the potential contributed by all the five subsystems (**Figure 1.1.1**) of the thermocell.

$$\alpha_S = \left(\frac{\Delta\varphi}{\Delta T}\right) = \left(\frac{\Delta_a\varphi + \Delta_c\varphi}{\Delta T}\right) + \left(\frac{\Delta_{a,e}\varphi + \Delta_{e,c}\varphi}{\Delta T}\right) + \left(\frac{\Delta_e\varphi}{\Delta T}\right) \qquad (1.1)$$

This can be classified as follows. The potential difference due to the ionic diffusion in the homogeneous electrolyte is the *homogeneous thermoelectric potential*. This homogeneous thermoelectric potential depends on the charge carrier concentration. The potential difference due to the electrode reactions at the electrolyte interface is the *heterogeneous thermoelectric potential* [2, 3]. The measured potential difference and the respective temperature gradient gives the *thermocell Seebeck coefficient* $\left(\frac{\Delta\varphi}{\Delta T}\right)$ [7, 8]. The thermocell Seebeck coefficients mainly depend on the transported entropy of the charge carriers. The thermoelectric potential usually has the sign of the hot electrode. A negative Seebeck coefficient means the hot electrode is negative concerning the cold electrodes [9, 10].

1.2 Importance of molten salt thermocell

Initially, these thermal regenerative thermocells are established with the liquid electrolytes. The electrolyte selection depends on the compatibility of the electrically active and thermally stable temperature window to the temperature range of the heat source. Categorized merely as an aqueous and organic electrolyte for low temperature (< 100 °C), ionic liquids for intermediate temperature (100 - 200 °C) and molten salts (fused salts) for higher temperature ranges [2, 4, 11-13]. In 1950's, the thermoelectric generator with solid semiconductor materials attained much attraction due to the difficulty in devising the liquid electrolyte thermocells, particularly at high temperatures. Also, the figure of merit and power output of the semiconductor thermoelectric generators is comparatively higher than for the liquid electrolyte thermocells. However, the thermal stability, materials cost and safety of the semiconductor thermoelectric generators at high temperature are still challenging. Meanwhile the development of high temperature devices like fuel cells, thermal energy storage, and thermal battery with molten salts provides a suitable material design and engineering for the liquid electrolyte thermocells at high temperature. The power output determines the energy efficiency of any power source than the dimensionless figure of merit. The power output can be amplified by series stacking of cells, even the molten salt thermocells will remain cheaper and safer than the semiconductor thermoelectric generators. These advantages increased the interest to investigate the high temperature molten salt thermocells over the past few decades [2, 4, 11, 12].

1.3 Molten salt thermocells – A literature review

Reviews in the field of molten salt thermocells were reported long ago, before 1972. Mostly they summarized the thermocells reported with single pure molten salt electrolyte [3, 7-10, 14-19]. Whereas, the recent developments are well far from the beginning, the Seebeck coefficients are increased a lot. In this chapter, it is planned to summarize the existing literature, considering the single molten salt and expand to molten salt composite electrolyte thermocells. However, this review is limited to the molten salt electrolyte thermocells reported in the molten phase, i.e., operated above the melting temperature of the molten salt electrolyte. For effective representation the available results are digitized as new comparative figures and tabulated by numerical values. Digitizing may slightly affect the accuracy of the original data.

1.3.1 Materials selection for molten salt thermocells

The basic operation of thermocell illustrates that the stable temperature difference and constant flow of ions between the electrodes can deliver a continuous and sizeable thermocell potential. It defines the requirement of the thermocell electrolytes to exhibit a low thermal conductivity with high ionic conductivity. These requirements complement the consideration of using the molten salts as an electrolyte in thermocells. The molten salts show an increase in ionic mobility and reduction in thermal conductivity on increasing temperature beyond the melting point. In semiconductor thermoelectric materials, the transport mechanism of heat and charge carriers is coupled directly. The diffusion of electrons through the lattice supports both the electrical and thermal conduction which leads to reduced thermoelectric power. However, the molten salts have a different transport mechanism; the electrical conduction is due to physical transport of ionic charge carriers, and the thermal conduction is due to the drift of particles from high to low energy region [3, 9]. The molten salts also offer wide temperature window between the melting and decomposition point with excellent chemical stability. The ready availability of a wide variety of molten salts with different melting temperature makes the thermocell operation possible at any temperature by the right choice of electrolyte. The molten salt electrolyte reacts fast with the electrode material of the same ion as in the melt, which simplifies the identification of a suitable electrode [10, 17].

1.3.2 Electrolytes for molten salt thermocell

Electrolytes with single pure molten salts:

The molten halides (MX) are extensively investigated as thermocell electrolytes, where M is the metal cation and X is the halogen anion (F, Cl, Br, I), but the experimental difficulties have limited investigations with the corrosive fluorides. Thermocell Seebeck coefficient of various single molten salt electrolytes is grouped by the electrodes nature (**Table 1.3.1** solid metal and **Table 1.3.2** gas electrodes).

Table 1.3.1 Seebeck coefficient of thermocells with various single molten salt electrolytes and metal electrodes.
$(T)M|MX|M(T+\Delta T)$

Electrode M	Electrolyte MX	Electrolyte Melting Point (°C)	Thermocell Average Temperature (°C)	Seebeck Coefficient (mV/K)	References
Ag	AgF	435	435-550	-0.38	[18]
	AgCl	605	500-900	-0.375	[10, 20]
	AgBr	432	700	-0.434	[21]
	AgI	558	727	-0.481	[22]
	Ag_2SO_4	652	657	-0.31	[23]
	$AgNO_3$	212	307	-0.344	[9]
Cu	CuCl	426	495-580	-0.434	[24]
	CuBr	492	801	-0.494	[25]
	CuI	606	727	-0.499	[22]

The general representation of *thermocells with metal electrodes* is $(T)M|MX|M(T+\Delta T)$, identical metal electrodes (M) same as the cation (M) in the electrolyte (MX). In metal electrodes thermocell the cationic diffusion from the hot to the cold electrode is predominant than the anions in the opposite direction [2, 14, 19]. Since the cations are the predominant charge carrier, this thermocell potential is termed as *cationic thermoelectric potential* [2]. The continuous operation will lead to the removal of the metal ions from the hot electrode and transport through the electrolyte to grow as dendrite on the cold electrode surface.

The theoretical expression of Seebeck coefficient of the metal electrodes thermocell is:

$$\alpha_S = \left(\frac{\Delta\varphi}{\Delta T}\right)_M = (S_M^* + S_{X^-}^*) - (S_{MX} - S_M) = S_M + S_M^* - S_{M^+}^* \qquad (1.2)$$

where (S_M) is the thermodynamical molar entropy of M in MX, (S_M^*) the entropy transported through the metal, and $(S_{M^+}^*)$ the entropy transported through the electrolyte. In a single molten salt system with identical valances of cations and anions the thermal flux is negligible due to the same concentration of oppositely charged ions [8]. Thus, the temperature gradient remains stable for a long time in the single molten salt electrolytes.

However, the growth of dendrite on the cold electrode and loss of ions from the hot electrode leads to short circuit and cell breakdown. Cornwell [3] proposed that the corrosive effect can be overcome by reversing the hot and cold electrodes periodically. However, in reality, completely filling back of the removed material to the electrode surface at the electrolyte interface is not possible (defines the metal electrodes are stationary) [14]. In some cases, the melting point of the suitable metal electrode is lower than the melting point of the respective molten salt electrolyte, and this unstable electrode phase makes the experimental condition difficult for the thermocell operation.

Gaseous electrode thermocells $(\mathrm{X(T)|MX|X(T + \Delta T)})$ are explored to overcome the above-mentioned corrosive effect on the hot metal electrode. The gas electrode can be a non-stationary electrode, because of the gas flow continuously on metal current collector surface [14].

Table 1.3.2 Seebeck coefficient of thermocells with various single molten salt electrolytes and gas electrodes.
$\mathrm{(T)X|MX|X(T + \Delta T)}$

Electrode X	Electrolyte MX	Electrolyte Melting Point (°C)	Thermocell Average Temperature (°C)	Seebeck Coefficient (mV/K)	References
Cl_2|C	LiCl	605	650,750	-0.534	[26]
	NaCl	801	850	-0.483	[26]
	KCl	770	800	-0.504	[26]
	RbCl	718	750	-0.544	[26]
	CsCl	645	700	-0.533	[26]
	AgCl	455	480, 580, 680	-0.667	[26]
	$PbCl_2$	501	550	-0.587	[26]
	$ZnCl_2$	290	347-580	-0.65	[18]
Br_2|C	AgBr	432	480-670	-0.701	[18]
I_2|C	AgI	558	600-700	-0.859	[15]
Cl_2|Pt	AgCl	605	500-900	-0.664	[10]
	$CdCl_2$	564	617-751	0.6	[27]
	$PbCl_2$	501	529-594	0.349	[27]
	$CdBr_2$	568	594-701	0.846	[27]

Usually, the electrode gas (X) will be similar to the anion (X) of the electrolyte (MX) for a favorable electrode reaction. The chlorine gas for chloride melts, oxygen for an oxide containing electrolyte and carbon dioxide for molten carbonate mixtures [10, 17]. The electrode gas gets ionized at one electrode and the resultant ion transported through the electrolyte to the opposite electrode where the reverse electrode reaction occurs. Here, anions diffusion contribute to the thermoelectric potential rather than the cations, so it is termed as *an anionic thermoelectric potential* [2].

In **Table 1.3.2**, the gas electrodes show a larger Seebeck coefficient than the solid metal electrodes (**Table 1.3.1**). The entropy due to the gas to liquid phase transition of the electrode gas contribute to the large Seebeck coefficient [28].

The theoretical Seebeck coefficient expression for the gas electrode thermocell is:

$$\mathrm{\alpha_S} = \left(\frac{\Delta\varphi}{\Delta \mathrm{T}}\right)_X = \left(S_M^* - S_{M^+}^*\right) - \left(S_{MX} - \frac{1}{2} S_{X_2}\right) \tag{1.3}$$

where (S_M^*) is the entropy transported through the metal, ($S_{M^+}^*$) the entropy transported through the electrolyte, (S_{MX}) the molar entropy of salt MX and (S_{X_2}) the molar entropy of X in MX.

However, the gas flow from the low temperature external source creates an additional temperature difference between the electrodes surface. Then the lag in establishment of perfect three-phase boundary at the electrode-gas-electrolyte interface will affect the potential measurement [15]. The Seebeck coefficient is dependent on temperature, and it increases with the increase in thermocell operating temperature [26]. The significant change in the Seebeck coefficient with temperature is reported as least square equations for various single molten salt thermocells with identical solid or gas electrodes [15].

Table 1.3.3 Calculated heat of transport for thermocell with chlorine gas electrodes [26]. $\mathrm{(T)Graphite|Cl_2|MCl|Cl_2|Graphite(T + \Delta T)}$

Electrolyte MCl	Thermocell Average Temperature (°C)	Seebeck Coefficient (mV/K)	Transported Entropy of Cl	Transported Entropy of M	Heat of Transport
LiCl	607	-0.534	79.4	60.8	0.7 ± 0.9
NaCl	800	-0.483	88.1	82.6	-0.1 ± 0.9
KCl	771	-0.504	85.5	91.1	2.3 ± 1.0
RbCl	722	-0.544	80.8	104.6	6.1 ± 0.9
CsCl	645	-0.533	80.3	108.0	5.1 ± 0.7
AgCl	455	-0.667	63.2	102.8	9.4 ± 1.2
$PbCl_2$	498	-0.587	72.1	103.0	4.6 ± 2.4

Fischer [26] extended the investigation to determine the heat of transfer in the single molten salt electrolyte, for the first time (**Table 1.3.3**). The experimental Seebeck coefficient $\left(\frac{\Delta\varphi}{\Delta \mathrm{T}}\right)$ is used to calculate the transported entropy of the charge carrier ($S^*_{Cl^-}$) by using equation (1.4) with the molar entropy $\left(-\frac{1}{2}S_{X_2}\right)$ of the ion.

$$\mathrm{F}\left(\frac{\Delta\varphi}{\Delta\mathrm{T}}\right) = S^*_{Cl^-} \left(-\frac{1}{2}S_{X_2}\right) - S^*_e \tag{1.4}$$

where F is the Faraday constant and S^*_e is the transported entropy of the electron in the metal current collector (usually negligible).

Table 1.3.4 The transported entropy of ions in single molten salt electrolytes thermocells with both metal and gas electrode pairs.

Electrode	Electrolyte	Thermocell Average Temperature (°C)	Transported Entropy of M (cal/mole-deg)	Transported Entropy of X (cal/mole-deg)	Absolute molar entropy of MX (cal/mole-deg)	References
Ag	AgCl	500 - 900	26.7	16.6	43.3	[10]
Cl_2|Pt	AgCl	500 - 900	23.3	20	43.5	[10]
Ag	Ag_2SO_4	657	21.05	54.1	96.2	[23]
Ag	$AgNO_3$	307	21.8	35.2	---	[29]

The sum of the cations ($S^*_{M^+}$) and anions ($S^*_{Cl^-}$) transported entropy (**Table 1.3.4**) will be equal to the absolute molar entropy (S_{MX}) of the salt [10, 23]. So, the transported entropy ($S^*_{M^+}$) of the cations in the electrolyte melt is estimated by the following expression,

$$S^*_{Cl^-} = S_{MX} - S^*_{M^+} \tag{1.5}$$

The partial molar entropy (S_{Cl^-}) of the anion is estimated with the correction factor of the mass ratio $\left(\frac{3}{2}\ R \ln\frac{m_+}{m_-}\right)$.

$$S_{Cl^-} = \frac{1}{\nu+1}\left(S_{MX} - \frac{3}{2}\ R\ln\frac{m_+}{m_-}\right) \tag{1.6}$$

$$S^*_{Cl^-} = \frac{q^*}{T} + S_{Cl^-} \tag{1.7}$$

where $\nu = z_+$, the heat of transfer (q^*) and the average temperature (T) of the thermocell. By using equations (1.6 and 1.7), the equation (1.4) can be rewritten with the term for heat of transfer.

$$\mathrm{F}\left(\frac{\Delta\varphi}{\Delta\mathrm{T}}\right) = \frac{q^*}{T} + \frac{1}{\nu+1}\left(S_{MX} - \frac{3}{2}\ R\ln\frac{m_+}{m_-}\right) - \frac{1}{2}S_{X_2} \tag{1.8}$$

Table 1.3.3 shows the calculated heat of transport for different single molten salts with chlorine gas electrodes. The transported entropy of ions can be assumed to be same for different molten salts with similar molar entropies and ionic valency. For example, the charge carrier's transported entropy of the AgCl electrolyte (Cl_2 electrodes) can be assumed for the thermocell with CuCl electrolyte (Cl_2 electrodes) [10].

A formation cell $\mathrm{M(T)|MX|X(T+\Delta T)}$, is a combination of the two of thermocells discussed above, i.e., with solid metal electrode on one side and gas electrode at the other side. The electrodes are not symmetrical to each other, then this could not be a thermocell, can simply called as *chemical / isothermal cell*.

The Reinhold equation (1.9) relates these different cells to validate the accuracy of the Seebeck coefficient [10, 26].

$$\left(\frac{\Delta\varphi}{\Delta\mathrm{T}}\right)_{\mathrm{X}} - \left(\frac{\Delta\varphi}{\Delta\mathrm{T}}\right)_{\mathrm{M}} = \left(\frac{\Delta\varphi}{\Delta\mathrm{T}}\right)_{\mathrm{Chem}} - \left(\frac{\Delta\varphi}{\Delta\mathrm{T}}\right)_{\mathrm{M-C}} \qquad (1.9)$$

where the subscripts denote the cell type, (X) gas electrode thermocell, (M) metal electrode thermocell, (Chem) the chemical/formation cell and ($\mathrm{M-C}$) the connector lead junction. The last term in the equation (1.9) is usually negligible.

The accuracy of the Seebeck coefficient of the AgCl thermocells is determined by using the values from two different studies [10, 26] at the same temperature is identical with an acceptable range of error. Also, it is possible to estimate the Seebeck coefficient of the thermocell (metal electrode) if the values are known for the other two types of cells (gas electrode thermocell and chemical cell) [7, 10, 18, 24, 26].

Electrolytes with binary/ternary molten salt mixture:

Seebeck coefficient of the thermocells reported with binary molten salt electrolyte mixtures is also categorized by the type of electrodes (**Table 1.3.5 a** - metal and **b** - gas electrodes) as in the previous section. The addition of the second salt reduces the melting point due to the change in lattice energy and the binary salt mixture shows a possible lowest melting point at the eutectic composition [30-32]. Thus, the binary electrolyte mixture permits to operate the thermocell at a low temperature than corresponding to the single salt electrolyte.

As specified earlier, the thermal flux is negligible for the single molten salt electrolyte, but in the case of multi-component electrolyte mixture it is significant [2, 6, 30, 33]. So, the potential changes with time due to the Soret effect and differ from the initial time potential. The Seebeck coefficient of the binary electrolyte mixtures can be interrelated to the Soret effect along with various transport properties. Such as diffusion coefficient, heat transfer, transported entropy, and the ions transport number [6, 30, 33-35]. To make an explicit discussion, another sub-grouping will be used such as binary electrolyte mixtures comprising (i) common anion with different cations, and (ii) common cation with different anions.

Table 1.3.5 Seebeck coefficient of thermocells with binary electrolyte mixtures (common anion and different cations)

(a) Silver metal electrodes. $(\mathrm{M_1(T)|M_1X - M_2X|M_1(T + \Delta T)})$

Electrolyte (Ag,M$_2$)X		Seebeck Coefficient (mV/K)						Thermocell Average Temperature (°C)	References
		The mole fraction of AgX							
X	**M$_2$**	**1**	**0.8**	**0.6**	**0.4**	**0.2**	**0.05**		
Cl	Li	-0.397	-0.38	-0.372	--	-0.374	-0.4	800	[36]
	Na	-0.397	-0.361	--	-0.354	-0.369		800	[36]
	K	-0.397	-0.341	--	-0.331	-0.328	-0.414	800	[20]
	Rb	-0.397	-0.333	-0.324	--	-0.324	-0.384	800	[36]
	Cs	-0.397	-0.323	-0.316	--	-0.32	-0.355	800	[36]
Br	Li	-0.434	-0.381	-0.362	-0.36	-0.335	--	700	[21]
	Na	-0.434	-0.366	-0.348	-0.357	-0.4	--	700	[21]
	K	-0.434	-0.366	-0.342	-0.34	-0.346	--	700	[21]
	Rb	-0.434	-0.365	-0.345	-0.33	-0.369	-0.477	700	[21]
	Cs	-0.434	-0.362	-0.318	-0.306	-0.343	-0.444	700	[21]
I	Na	-0.481	-0.435	--	-0.391	-0.41	-0.492	727	[22]
	K	-0.481	-0.41	--	-0.355	-0.363	-0.451	727	[22]
	Rb	-0.481	-0.431	--	-0.36	-0.37	-0.438	727	[22]
	Cs	-0.481	-0.429	--	-0.356	-0.371	-0.44	727	[22]
NO$_3$	Li	-0.33	-0.344	-0.365	--	-0.458	-0.562	340	[37]
	Na	-0.33	-0.333	-0.33	--	-0.36	-0.462	340	[37]
	K	-0.332	-0.313	-0.276	-0.273	--	-0.349	360	[37]
	Rb	-0.355	-0.378	-0.374	-0.37	-0.442	--	340	[33]
	Cs	-0.355	-0.373	-0.336	-0.34	--	--	340	[33]
SO$_4$	Li	-0.31	--	-0.361	--	-0.348	--	590-750	[38]

(b) Chlorine gas electrodes. $(\mathrm{X(T)|M_1X - M_2X|X(T + \Delta T)})$

Electrolyte (Pb,M)Cl$_2$	Seebeck Coefficient (mV/K)					Thermocell Average Temperature (°C)	References
	The mole fraction of PbCl$_2$						
M	**1**	**0.75**	**0.5**	**0.25**	**0**		
Li	-0.570	-0.540	-0.536	-0.500	-0.534	727	[39]
Na	-0.570	-0.540	-0.491	-0.480	-0.483	727	[39]
K	-0.570	-0.495	-0.450	-0.440	-0.504	727	[39]
Cs	-0.570	-0.530	-0.470	-0.470	-0.533	727	[39]

The change in initial state Seebeck coefficient for different concentrations of AgCl in the electrolyte with other molten chlorides is shown in **Figure 1.3.1**. Here the electrolyte mixture contains common Cl^- anion and different cations. The Seebeck coefficient of the pure AgCl electrolyte remains stable with increasing temperature. But the substitution of a second chloride salt (LiCl) into the AgCl electrolyte shifts the Seebeck coefficient to a positive value by increasing the temperature (**Figure 1.3.1 a**).

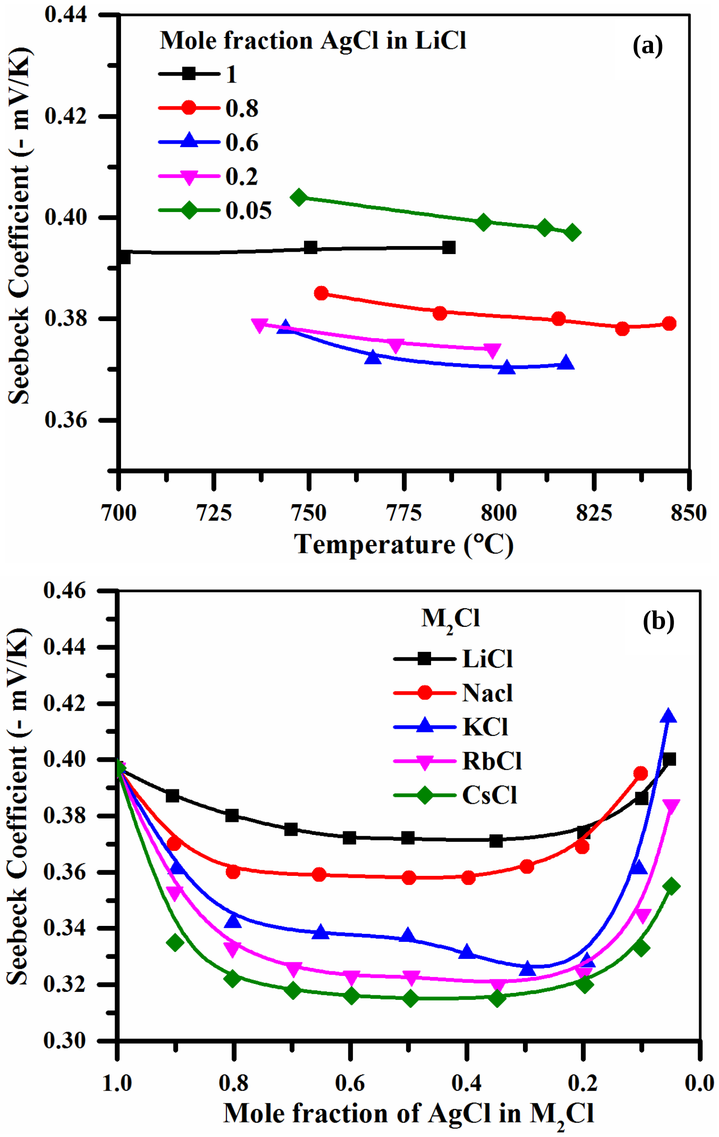

Figure 1.3.1 The change in the Seebeck coefficient of binary AgCl – LiCl electrolyte with Ag electrodes **(a)** function of temperature and **(b)** function of AgCl concentration at 800 ºC [36].

At the same time (**Figure 1.3.1 b**) the reduction in AgCl concentration shows a positive deviation at the concentrations close to pure AgCl. Then, it follows a constant plateau at the equimolar regain and shows a negative deviate at the low AgCl concentrations. The less reactivity of Ag metal electrodes in a molten salt with an almost negligible concentration of AgCl (< 0.005 AgCl) limits the experimental possibility. The authors have extrapolated the

Seebeck coefficient for this region [36], but difficulties in digitization limits to produce the data here. The profile is also identical for the other similar electrolyte mixtures ($(\mathrm{M_1} - \mathrm{M_2})\mathrm{X}$) in **Table 1.3.5 a**. Like the Ag electrodes in AgCl electrolyte mixture, less feasibility of the Cu metal electrode in electrolyte mixtures with low Cu^+ concentration is also reported [22]. However, the Seebeck coefficient changing trend differs for the binary electrolyte mixture with a common divalent anion (NO_3, SO_4) and different monovalent cations (**Table 1.3.5 a**) [6, 33, 35, 37, 38, 40].

The Seebeck coefficient changing trend due to the different cation concentration in electrolyte mixtures with the chlorine gas electrodes is identical to the trend observed with solid metal electrodes in similar electrolyte composition (**Table 1.3.5 b**) [39]. The change in anion-cation lattice chemical energy and the electrode reactivity influence the transported entropy. The Seebeck coefficient of binary electrolyte mixtures with the gas electrodes is larger than the metal electrodes, as observed for the single molten salt electrolyte thermocells. Also, the less practical feasibility of the metal electrode in electrolyte mixture with the low concentration of the corresponding cation may be resolved by using the gas electrodes. Since the gas electrodes reaction dependent on the anions in the electrolyte, so the thermocell measurement is possible for the entire concentration range (**Table 1.3.5 b**). Even though, substitution of different cations in the electrolyte will not affect the gas electrode reaction. But the Seebeck coefficient gets altered by the change in anionic diffusion due to the difference in anion-cation lattice energy.

Pezzati *et al.* [20-22, 36, 39] showed the possibilities to determine the other transport properties of the binary electrolyte mixtures from the measured initial Seebeck coefficient. This was similar to the approach implemented by Fischer [26] for the single molten salt electrolyte thermocells (equation 1.4 to 1.8). Here, a function (ψ) is calculated by using the initial Seebeck coefficient, transport number of cations and excess entropy (transported entropy) to determine the heat of transfer. The experimental (ψ) function is compared with a linear (ψ) function calculated theoretically by applying a set of ideal conditions as matching the experimental situation. The conditions considered for linearity are, the excess entropy is zero, the heat of transport of ions remain constant on the change in concentration, and the transport number of the two cations being equal to their ionic fractions. However, the experimental (ψ) function calculated from the initial Seebeck coefficients shows both positive or negative deviations over the expected ideal (ψ) function. Because the heat flux in the binary molten salt mixture is not negligible as in a single salt electrolyte.

Haase *et al.* [6] considered the heat flux by using the initial and steady state Seebeck coefficients for the calculation of the transport properties, which results in better accuracy and shows the possibility to relate the Soret coefficient. In **Figure 1.3.2**, the calculated transport properties and the measured Seebeck coefficients are shown as a function of $AgNO_3$ concentration in $LiNO_3$ electrolyte mixture.

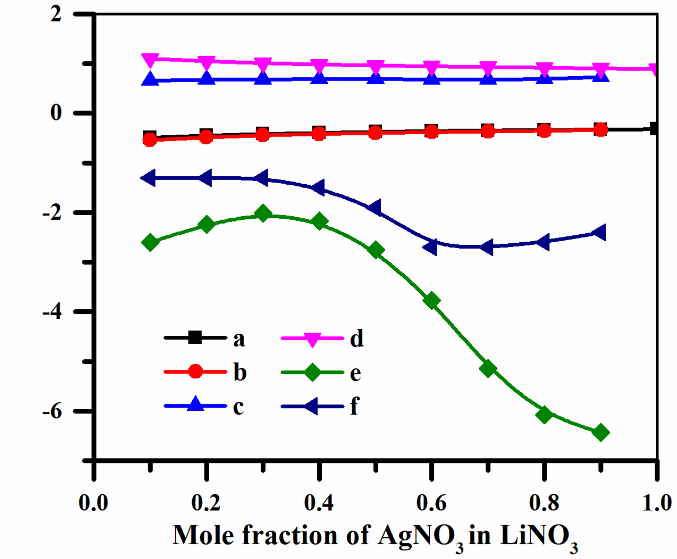

Figure 1.3.2 The transport phenomenon of $AgNO_3$ - $LiNO_3$ electrolyte mixture with Ag electrodes at 260 ºC [6].

Seebeck coefficient **(a)** initial and **(b)** steady state (mV/K); Transported entropy **(c)** Li and **(d)** Ag cations (102 J/K.mol); **(e)** Difference in heat of transfers (Li-Ag) ions (103 J/mol); **(f)** Soret coefficient (103 J/mol)

The Seebeck coefficient of a metal electrodes thermocell $M_1(T)|M_1X - M_2X|M_1(T + \Delta T)$ with common anion and different cations binary electrolyte mixture at the initial time is:

$$\left(\frac{\Delta\varphi}{\Delta T}\right)_{j\to 0,t\to 0} = \alpha_{S,0} = -\frac{1}{F}\left[S_{M_1} + S^*_{M_1} - S^*_{M_1+} + \frac{1}{2}t_{M_2^+}\frac{q^*}{T}\right] \qquad (1.10)$$

The Seebeck coefficient of the same thermocell in Soret equilibrium state is:

$$\left(\frac{\Delta\varphi}{\Delta T}\right)_{j\to 0,t\to \alpha} = \alpha_{S,\alpha} = -\frac{1}{F}\left[S_{M_1} + S^*_{M_1} - S^*_{M_1+}\right] \qquad (1.11)$$

where, S_j is the entropy of component j at the average temperature (T) and, the terms $S^*_{M_1}$ and $S^*_{M_1+}$ are the transported entropy of M_1 ion. The transference coefficient of M_2 is ($t_{M_2^+}$) and the ratio $\frac{q^*}{T}$ may be interpreted in terms of enthalpy changes across the layer. The last term in the initial time (1.10) will disappear at the Soret equilibrium state (1.11).

Ito *et al.* [41] demonstrated the thermocells with ternary electrolyte mixture containing the same anion and different cations. Thermocells operated with Ag metal electrodes for AgCl-LiCl-KCl and Cu for CuCl-LiCl-KCl electrolyte mixture. In **Figure 1.3.3 a**, the initial Seebeck coefficient for the two different thermocells shows a same linear dependence on the electrolyte composition. The slopes are almost the same (0.198 for Ag|AgCl and 0.2 for Cu|CuCl).

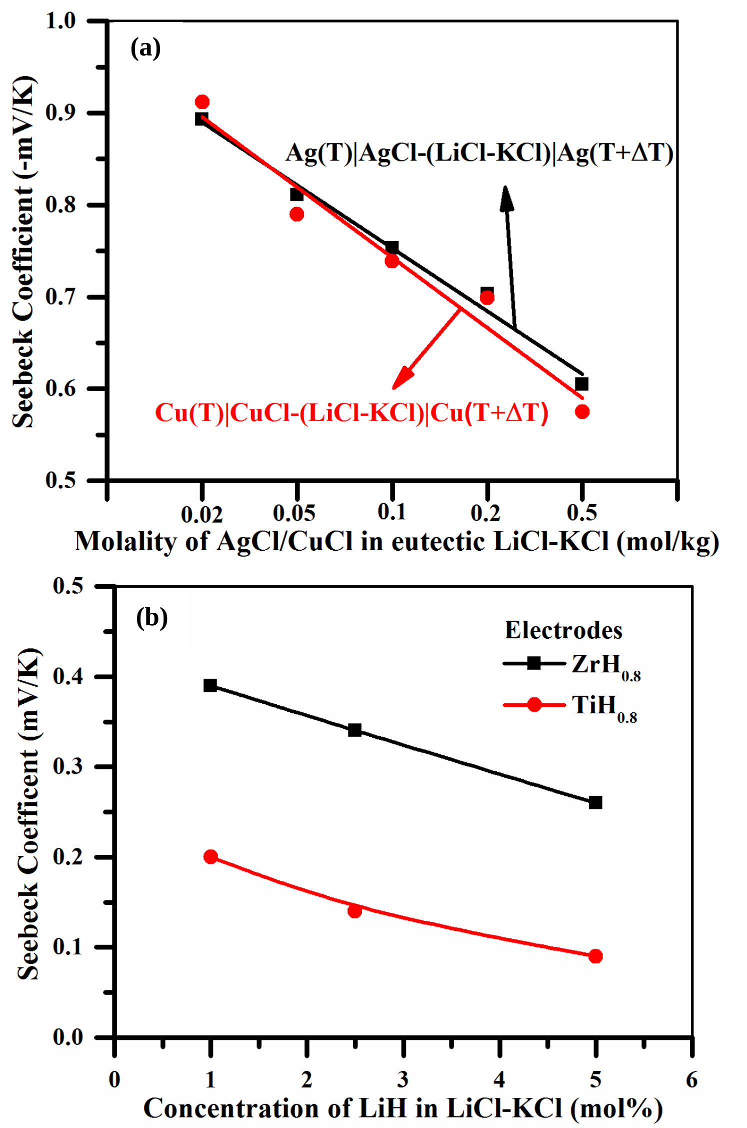

Figure 1.3.3 Thermocell Seebeck coefficient for eutectic (LiCl-KCl) electrolyte mixture with a different concentration of **(a)** silver or copper **c**hloride [41] and **(b)** lithium hydride [42].

But in **Figure 1.3.3 b**, the Seebeck coefficients display a constant difference between the two different thermocells having same electrolyte mixture with different electrode pairs [42]. This confirms that the Seebeck coefficient is significantly influenced by the electrode-electrolyte reactivity.

Table 1.3.6 Seebeck coefficient of the electrolyte mixture with common cations and different anions [43, 44].
$\mathrm{M(T)|MX_1 - MX_2|M(T + \Delta T)}$

Electrolyte Mixture		**Thermocell Average Temperature (°C)**	**Mole Fraction MX_1**	**Seebeck Coefficient (mV/K)**	**Transported Entropy (cal/mole-deg)**			
MX_1	**MX_2**				**M**	**X_1**	**X_2**	**Total X**
AgBr	AgCl	541-616	0	-0.391	25.48	--	15.68	15.68
			0.2	-0.399	25.74	19.72	16.01	16.75
			0.52	-0.418	26.15	18.76	15.71	17.3
			0.7	-0.429	26.38	18.4	15.76	17.61
			0.8	-0.445	26.52	17.92	16.67	17.67
			1	-0.445	26.77	16.91	--	16.91
AgCl	$AgNO_3$	235-298	0	-0.335	21.01	--	32.98	32.98
			0.1	-0.345	21.33	13.13	32.87	30.9
			0.2	-0.355	21.63	11.46	32.8	28.53
			0.35	-0.38	22.11	9.87	32.74	24.73
AgI	AgBr	531-618	0	-0.442	26.63	--	17.05	17.05
			0.2	-0.445	26.89	24.09	17.31	18.67
			0.5	-0.461	27.25	21.47	18.1	19.78
			0.8	-0.482	27.65	20.17	19.41	20.01
			1	-0.498	27.88	19.54	--	19.54
AgCl	AgI	556-616	0	-0.498	27.83	--	19.59	19.59
			0.2	-0.466	27.37	17.41	20.4	19.8
			0.5	-0.433	26.65	16.51	22.01	19.26
			0.8	-0.419	25.94	15.84	25.49	17.77
			1	-0.391	25.48	15.68	--	15.68

Thermocells operated with binary molten salt electrolyte mixtures of *common cation and different anions* are shown in **Table 1.3.6** with silver metal electrodes. The initial Seebeck coefficient shows a linear dependence on the electrolyte concentration and cell temperature as observed in the previous electrolyte mixtures [43, 44]. This behavior is similar to the binary electrolyte mixture with the common anions and different cations.

Ishida *et al.* [43] related the measured initial Seebeck coefficient to the electrical conductivity behavior of the electrolyte mixture. Both the parameters display the same changing tendency on the increase in temperature and for different electrolyte compositions. They concluded that the change in the charge carrier activation energy could alter the thermocell Seebeck coefficient.

Electrolytes with molten salt and molten metal/semiconductor mixture:

The thermocells with the electrolyte mixture containing a mixture of molten salts and molten metals with a pair of graphite electrodes are shown in **Table 1.3.7** [45, 46].

Table 1.3.7 Transport quantities of molten metal – molten salt electrolyte thermocells [45, 46].
$C(T)|Bi - BiX_3|C(T + \Delta T)$ where X = Cl, Br, I
(a) Electrolyte mixture with different Bi mol% in $BiBr_3$ at a 550 °C.

Bi (mol%)	Seebeck Coefficient Bi + $BiBr_3$ (μV/K)		Difference between Initial and Steady State Seebeck Coefficient			Electronic Transport Number		
	Initial	Steady	Bi + $BiBr_3$	Bi + $BiCl_3$	Bi + BiI_3	Bi + $BiBr_3$	Bi + $BiCl_3$	Bi + BiI_3
10	-26	-214	189	244	826	0.43	0.41	0.49
20	-17	-182	165	215	248	0.61	0.55	0.76
30	5	-55	60	152	19	0.79	0.71	0.92
40	45	41	3	--	2	0.95	--	0.97
50	31	31	0	--	3	1	--	1
60	--	--	--	--	1	--	--	1

(b) Electrolyte mixture with 30 mol % Bi in $BiBr_3$ at different temperatures.

Thermocell Average Temperature (°C)	Seebeck Coefficient (μV/K)		Difference between Initial and Steady State Seebeck Coefficient		Electronic Transport Number	
	Initial	Steady State	Bi + $BiBr_3$	Bi + BiI_3	Bi + $BiBr_3$	Bi + BiI_3
300	-132	-278	154	--	0.01	--
350	-112	-238	146	--	0.06	--
400	-69	-200	136	--	0.16	--
450	-69	-178	125	42	0.36	0.81
500	-13	-132	109	31	0.52	0.87
550	5	-55	60	19	0.79	0.92

Usually the metals will dissolve in their own molten salts to form a true solution and change the molten salt properties [47]. The molten metal-molten salt dissolution can be categorized as metallic and non-metallic solution. In this Bi+BiX_3 systems at the molten salt-rich concentration, the Bi dissolution is non-metallic due to the chemical reactivity with BiX_3 [48]. Whereas at the molten metal-rich concentration it is metallic, thus the system transforms from non-metallic to metallic and changes the transport mechanism. So, the electrolyte mixture exposes the possibility of mixed charge carriers with ions and electrons. Thus, they believed that the change in the dominant charge carrier due to the difference in concentration of molten salt and molten metal in the electrolyte could affect the Seebeck coefficient. Therefore, based on the electrolyte composition the system was divided and the transport behaviors are explained further.

They used different transport mechanisms to explain the diffusion process in the electrolyte mixture at different compositions. Hopping and scattering electronic transport mechanisms are used from the molten salt-rich region till the intermediate regions with mixed charge carriers. Beyond the intermediate region until the high electron mobility molten metal-rich region the Faber-Ziman theory was used.

The steady state Seebeck coefficient of Bi-BiI_3 electrolyte moves from -1098 to 121 μV/K for the molten salt-rich region to molten metal-rich region. A maximum of ~170 μV/K found in the intermediate region with the mixed charge carriers [45]. The time to reach the steady state was also relay on electrolyte composition (5-12 h for molten salt-rich composition and 3-5 days in the intermediate region). However, the electrolytes with the molten metal-rich concentration show no distinguishable difference between initial and steady state conditions. It shows that the molten metal-rich concentration (electrons are the only charge carriers) achieves the steady state in short time than the other region with ionic charge carriers.

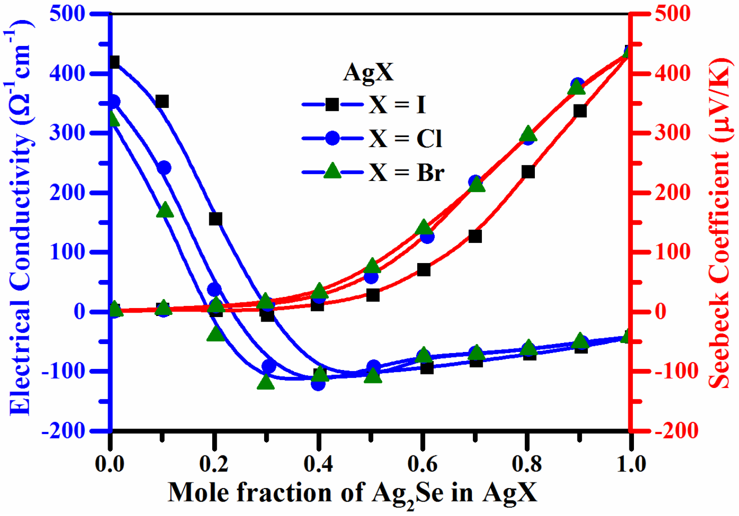

Figure 1.3.4 The Seebeck coefficient and electrical conductivity as a function of Ag*X* (*X* = I, Cl, Br) concentration in Ag_2Se at 900 ºC [49, 50].

$$Ag/C(T) \mid AgX(1-c) - Ag_2Se(c) \mid Ag/C(T+\Delta T)$$

Electrodes were sliver for electrolyte mixture ($c \leq 0.6$) while graphite for ($c \geq 0.7$)

Ohno *et al.* [49-56] investigated the thermocells consisting electrolyte mixture of molten halides (*MX* where *M* = Ag, Ni, Cu; *X* = I, Cl, Br) with molten semiconductors (*MS*; *M* = Ag, Ni, Cu; S = Se, S, Te). The stoichiometric liquid metal alloys (*MS* where *M* = Ag, Ni, Cu; *S* = Se, S, Te) displays a semiconductor behavior with short-range order. Thus, they were referred to as zero bandgaps liquid semiconductor, but an unusual negative dependency on temperature was observed [49, 57, 58]. However, the addition of molten halides to the molten semiconductor decreases the electric conductivity due to the increase in the conduction bandgap [49, 50, 52, 56]. **Figure 1.3.4** displays the change in thermoelectric behavior and electrical conductivity for change in electrolyte composition.

In liquid phase (> 400 K) [31, 32], all these mixtures exhibition a superionic conduction behavior around the mole fraction (c = ~ 0.4) in **Figure 1.3.4**. Where the metal cations became a predominant charge carrier, this refers to the p-n transition by considering the corresponding change in the electrical conductivity [49, 55]. **Figure 1.3.4** shows that the change in conductivity behavior could influence the thermoelectric behavior to a certain extent. For a favorable electrode reaction the Ag metal electrodes are exchanged by graphite electrodes beyond the mole fraction of 0.6 until 1 (**Figure 1.3.4**). Similar to the molten metal - molten salt mixture discussed above, different mechanisms are used to explain the transport behavior at different concentration region of the molten salt - molten semiconductor mixture [49].

Electrolytes with molten salt and solid oxide mixture:

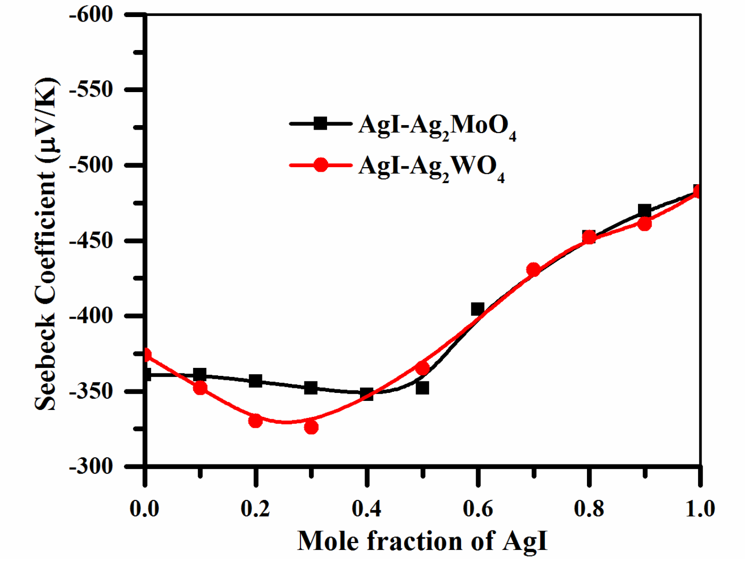

Figure 1.3.5 The Seebeck coefficient as a function of AgI concentration in the electrolyte mixture at 1000 K [59].

The high Ag^+ ionic mobility in AgI mixture with solid oxides like Al_2O_3 and Ag_2O-B_2O_3 suggests that they may be suitable solid electrolytes for thermoelectric cells [60, 61]. Schiraldi *et al.* [59] shown the thermocells with such electrolyte mixtures in both solid and liquid phases. The liquid phase Seebeck coefficient of the electrolyte mixture is shown in **Figure 1.3.5**. In the electrolyte mixture, the Ag_2XO_4 (X = Mo, W) is dispersed as glass matrix and it lower the liquidus temperature of the AgI in the mixture, whereas the pure AgI melts at 305 °C. Also, it provides high ionic mobility because the molten AgI ions migrate along the surface of the dispersed Ag_2XO_4 particles. These change in the thermal and transport properties delivers a better Seebeck coefficient than the pure AgI. Investigation of the thermoelectric potential of the solid-liquid phase transition region shows a discontinuity (less than 10%) for the electrolyte mixture (AgI in Ag_2WO_4). This supports the previous link of the thermocell behavior with the electrical conductivity, thus the change in charge carrier concentration in electrolyte melt has an impact on both behaviors.

Table 1.3.8 Seebeck coefficient of thermocells with molten carbonates and solid oxide electrolyte mixture with gas electrodes.

Electrolyte Mixture		**Gas Electrodes**		**Thermocell Average Temperature (°C)**	**Seebeck Coefficient (mV/K)**	**References**
Solid Oxide (55 wt%)	**Molten Salt (45 wt%)**	**Gas mixture**	**Current Collector**			
MgO	$(Li,Na)_2CO_3$	$0.62\ CO_2, 0.38\ O_2$	Pt	527 - 877	-1.18	[62]
		$0.65\ CO_2, 0.35\ O_2$			-1.17	
		$0.65\ CO_2, 0.35\ O_2$			-1.14	
	$(Li,Na,K)_2CO_3$	$0.67\ CO_2, 0.33\ O_2$			-1.14	
		$0.65\ CO_2, 0.35\ O_2$			-1.20	
	$(Li,Na)_2CO_3$	$0.50\ CO_2, 0.50\ CO$		777 - 877	-0.66	
	$(Li,K)_2CO_3$	$0.55\ CO_2, 0.45\ CO$			-0.64	
	$(Li,Na,K)_2CO_3$	$0.50\ CO_2, 0.50\ CO$			-0.63	
--	Li_2CO_3	$0.67\ CO_2, 0.33\ O_2$	Au	750	-0.88	[28]
MgO	Li_2CO_3				-1.04	[63]
	$(Li,Na)_2CO_3$				-1.13	
	$(Li,K)_2CO_3$				-1.25	
CeO_2	Li_2CO_3				-1.05	[28]
$LiAlO_2$	Li_2CO_3				-1.00	

In 1977 Jacobsen and Broers [62] used the thermocells to study the single electrode heat balance and temperature gradient created by non-symmetrical heat evolution at the electrodes. The thermocell consisted of an electrolyte mixture having molten carbonates and solid MgO (**Table 1.3.8**). They believed that the addition of solid oxide into the molten carbonates improves the viscosity of the electrolyte for easy handling. However, research in molten carbonate fuel cells with a similar electrolyte mixture provides the detailed transport mechanism.

In this mixture, the carbonate ions will be the major charge carriers because the negative surface charge of the solid MgO attracts the positively charged cation and hinder their diffusion [64]. Even though the electrical conductivity is higher for the molten carbonates without MgO, the reduction in the thermal convection on addition of solid MgO delivers a higher Seebeck coefficient [63-65]. In 2015, Børset *et al.* [28, 63] investigated similar thermocells with CO_2 rich gas electrodes. The transported entropy of the carbonate ions was calculated for a better understanding of the transport phenomenon in the electrolyte mixtures (**Table 1.3.8**). Changing the Pt current collectors with Au metal has no significant change of the Seebeck coefficient for identical thermocells. The Li_2CO_3 electrolyte mixture with and without MgO at 750 ºC, shows an increase (more negative) in the Seebeck coefficient from -0.88 to -1.04 mV/K on the addition of MgO. This increase in Seebeck coefficient follows a decrease in the transported entropy of the carbonate ion [63].

The initial Seebeck coefficient of the electrolyte mixture containing molten carbonates dispersed with solid MgO and ($CO_2|O_2$) gas electrodes is:

$$\alpha_{S,0} = -\frac{1}{F}\left[\frac{1}{2}\,S_{CO_2} + \frac{1}{4}\,S_{O_2} + S_e^* - \frac{1}{2}\,S_{CO_3^{2-}}^* + \left(\frac{t_2}{x_2} - \frac{t_1}{x_1}\right)\frac{q^*}{T}\right] \qquad (1.12)$$

where S_j is the entropy of component j at the average temperature of the electrodes T and pressure p_j. Terms S_e^* and $S_{CO_3^{2-}}^*$ are the transported entropy of the electron and carbonate ion. Generally, the entropies and the transported entropies are functions of temperature. The gas entropies are expected to be larger than the transported entropies. These terms have then a negative contribution to the Seebeck coefficient. Then t_1, t_2 are the transference coefficient and x_1, x_2 are the mole fractions of Li_2CO_3 and M_2CO_3. The ratio $\frac{q^*}{T}$ may be interpreted in terms of enthalpy changes across the layer.

The steady-state (Soret equilibrium) Seebeck coefficient of the thermocell is:

$$\alpha_{S,\alpha} = -\frac{1}{F}\left[\frac{1}{2}\,S_{CO_2} + \frac{1}{4}\,S_{O_2} + S_e^* - \frac{1}{2}\,S_{CO_3^{2-}}^*\right] \qquad (1.13)$$

Addition of Na_2CO_3 into Li_2CO_3-MgO mixture increases the Seebeck coefficient further, while the addition of K_2CO_3 has an opposite effect. This confirms the influence of the cation-anion lattice energy on the diffusion of carbonate ion and transported entropy [28]. Also the heat of transfer was calculated by using the measured initial and steady state Seebeck coefficients in equations (1.12 and 1.13). A small value was obtained for the term $\left(\frac{t_2}{x_2} - \frac{t_1}{x_1}\right)\frac{q^*}{T}$ containing the heat of transfer (q^*), and this could be due to the transference coefficient in the term, not because of (q^*) [63]. This binary electrolyte mixtures enable the cell to operate from 550 ºC. Here, the Seebeck coefficient found to increase with an increase in cell temperature, while Jacobsen *et al.* haven't observed such temperature dependence [28, 62, 63]. The change in the Seebeck coefficient and transported entropy of the Li_2CO_3 electrolyte mixture with different solid oxides (MgO, CeO_2, $LiAlO_2$) confirms that the solid oxide surface charge and the interface effect influences the thermocell transport behavior.

The NaF-AlF_3-Al_2O_3 electrolyte mixture used in the aluminum electrowinning electrolyte is studied in thermocell (**Figure 1.3.6**) [66]. The thermocell is demonstrated with two different pairs of electrodes, liquid aluminum metal and oxygen gas electrodes.

The expression for Seebeck coefficient of the thermocell $(T)Al(l)|NaF, AlF_3, Al_2O_3|\,Al(l)(T + \Delta T)$, with liquid aluminum electrodes at steady state (Soret equilibrium) is

$$\alpha_{S,\alpha} = \frac{1}{F}\left[S^*_{Al} + \frac{1}{3}\,(1 - t_{el})\left(S_{Al} - S^*_{Al^{3+}}\right) + t_{el}S^*_{el}\right] \tag{1.14}$$

The left-hand side electrode reaction of the cell is

$$\frac{1}{3}Al(l) = \frac{1}{3}Al^{3+} + e^- \tag{1.15}$$

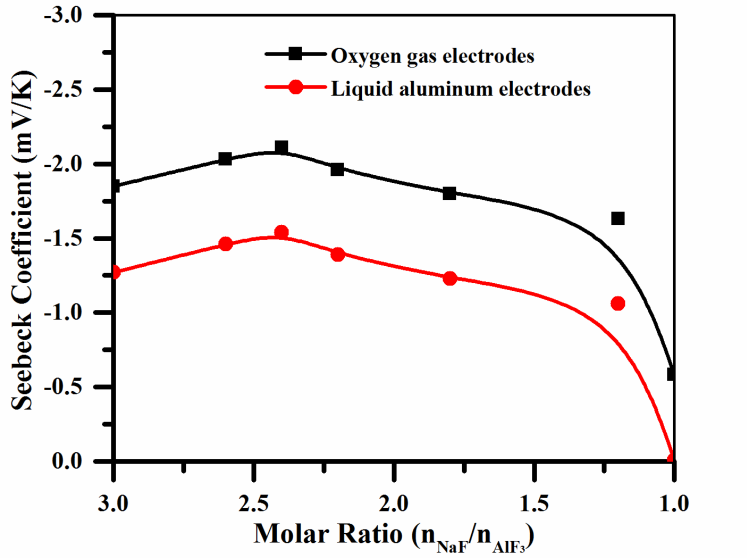

Figure 1.3.6 Thermocell Seebeck coefficient of electrolyte mixtures with **(a)** $PbCl_2$-LiCl and **(b)** NaF-AlF_3-Al_2O_3 in the presence of liquid metal or gas electrodes [66].

The steady state (Soret equilibrium) Seebeck coefficient of the thermocell $(T)Pt - O_2(g)|NaF, AlF_3, Al_2O_3|Pt - O_2(g)(T + \Delta T)$ with O_2 gas electrodes is

$$\alpha_{S,\alpha} = \frac{1}{F}\left[-\frac{1}{4}\,S_{O_2} + S^*_{pt} + \frac{1}{2}S^*_{O^{2-}}\right] \tag{1.16}$$

The left-hand side electrode reaction of the cell is

$$\frac{1}{2}O^{2-} = \frac{1}{4}O_2(g) + e^- \tag{1.17}$$

As shown in (1.10) and (1.11), the term $\left(t_{Na^+}\frac{q^*}{T}\right)$ is disappeared the steady state as shown in (1.14) and (1.16). A significant change in the Seebeck coefficient was reported for the change in the molar ratio (NaF/AlF_3) from 1.2 to 1.0, due to a loss in one degree of freedom at this composition. **Figure 1.3.6** shows that this change is observed in both thermocells irrespective of its electrode type (liquid Al metal or O_2 gas electrode).

1.3.3 Electrodes for Molten salt thermocell

Solid metal electrodes:

As discussed before the metal electrodes limit the thermocell durability due to the corrosion effect on the hot electrode. The electrode can be reversed periodically (i.e. hot to cold side or vice versa) to overcome this limitation, but complete filling back of the corroded material back into the metal is impossible [17]. Also, metal electrodes require a favorable ionic concentration in the electrolyte mixture for high electrode reactivity.

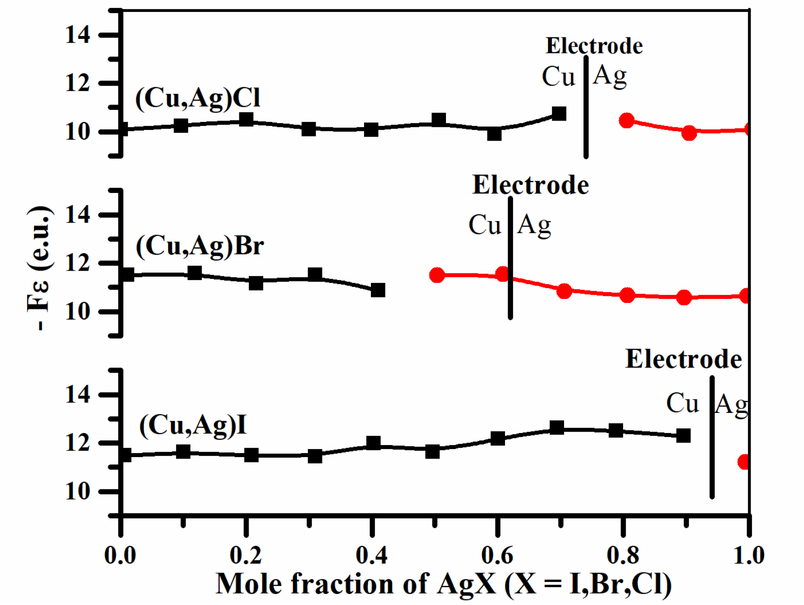

Figure 1.3.7 Initial thermoelectric power of the electrolyte mixture (Cu,Ag)X where X = I, Br, Cl with copper or silver electrodes [67].

Schiraldi *et al.* [67] tried a theoretical approach to determine suitable metal electrodes for the different cationic concentrations in the electrolyte mixture (vertical solid line in **Figure 1.3.7**). The theoretical estimation considers the thermodynamic activity, standard potential and phase diagram of both the electrolyte mixtures and metal electrodes. The suitability of Ag and Cu electrodes in the electrolyte mixtures with iodides and chlorides follows from the theoretical estimation. But, the bromide electrolyte mixture shows a shift of 10 mol% due to the contribution of the excess entropy of the ions, the theoretical prediction differs in the experimental condition. However, both the theory and experiment confirm that the electrode reactivity has an impact on the Seebeck coefficient.

In some cases, the low melting point of solid metal electrodes than the suitable molten salts electrolyte limits the thermocell operation. Thus, more reports are available with Ag, and Cu metal electrode thermocells contains corresponding silver and molten copper halide electrolytes rather than using low melting metals like tin, zinc, and lead [68].

Liquid metal electrodes:

In 1969, Trolle *et al.* [69] reported the possibility of the thermocells with the low melting point metal electrodes. They employed the metals in molten phase as liquid metal electrodes. In **Figure 1.3.8** shown the Seebeck coefficient of the thermocell with liquid Pb metal electrodes in the electrolyte mixture containing different concentration of $PbCl_2$ in LiCl. Blinov *et al.* [70] also investigated the same electrolyte mixture with liquid Pb electrodes and explained the transport behavior of the thermocell. The transported entropy of the reacting metal ion of the electrode is linked to the chemical potential of the polarized metal atom at the electrode surface under adiabatic condition.

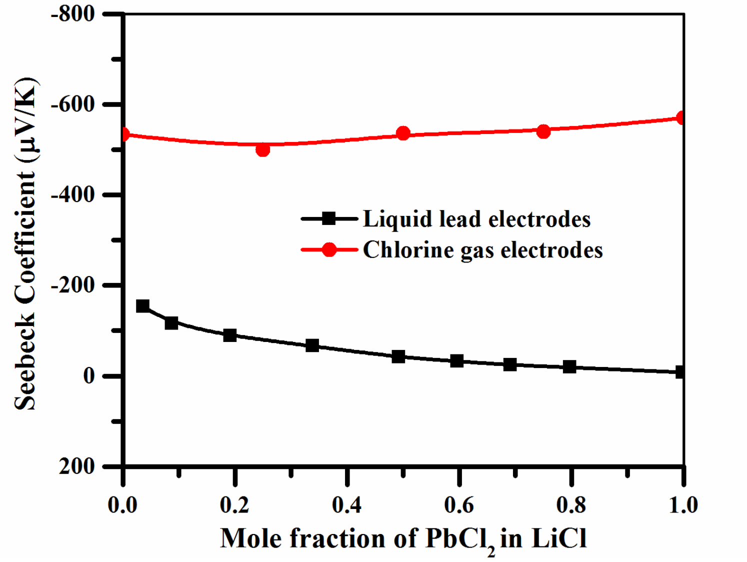

Figure 1.3.8 Seebeck coefficient of thermocells with $PbCl_2$-LiCl electrolyte mixtures and with both liquid metal or gas electrodes [39].

The Seebeck coefficient of the liquid metal electrode thermocells in both electrolyte mixtures (**Figure 1.3.6** and **Figure 1.3.8**) remains smaller (less negative) than for gaseous electrodes [17, 39, 66]. Thus, the Seebeck coefficient of the gas electrodes thermocell is large, irrespective of the phase of the metal electrode (solid or liquid). In equations (1.4, 1.12, 1.13, 1.16) the Seebeck coefficient depends on the transported entropy of electrode gas, it confirms that the gas to liquid phase transition entropy influences a lot.

Gas electrodes:

Even though the gas electrodes overcome the drawback of metal electrodes and deliver a larger Seebeck coefficient. There are few possible factors that could affect the reliability and interrupt the potential measurements. Since the electrode gas is supplied from the low-temperature external source, it can add an extra cooling effect and insufficient electrode contact area due to the imperfect three-phase boundary (electrode-gas-electrolyte interface). There are very few reports optimized the conditions to establish a well-equilibrated three-phase interface for better thermoelectric conversion. Meissner *et al.* [71] reported an increase in the thermoelectric potential for reduction in electrode gas pressure from 1 to 0.1 atm. Kang *et al.* [63] studied the effect of the partial pressure of electrode gas mixture ($CO_2|O_2$). They maintained the total pressure to 1 atm by appropriate addition of He gas. The change in electrode gas composition alters the thermocell Seebeck coefficient due to the electrode gas reaction rate to the $(Li,Na)_2CO_3$-MgO electrolyte mixture. The Seebeck coefficient increases with a decrease in the partial pressure of the CO_2 and O_2 in the electrode gas mixture.

1.3.4 Molten salt thermocell design

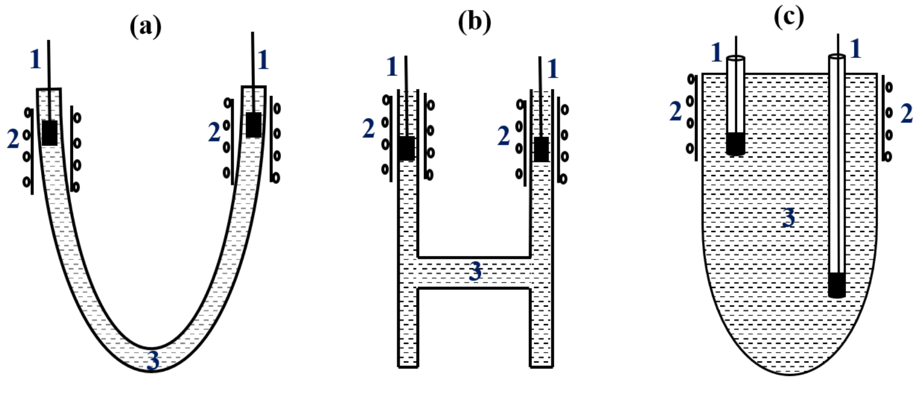

Figure 1.3.9 Schematic of the different thermocell setups with molten salt electrolyte. (1- electrodes, 2- heating filaments, and 3- molten salt electrolyte)

Due to the high influence of convection in aqueous electrolytes, the orientation of electrodes in thermocell has been thoroughly investigated in many studies to overcome the convention effect for better performance. However, the possibility of convection or gravitational forces is less in molten salt electrolytes, so no dedicated research is available to understand the impact of the cell design in the performance of molten salt thermocells [30]. The Seebeck coefficient of molten carbonate thermocell with identical electrolyte composition and operating condition, but with different electrodes orientation reported in two different studies are indistinguishable [28, 62, 63].

At the preliminary stage, most experimental cells of the molten salt thermocells are U or H shape vertical cells (**Figure 1.3.9 a** and **b**) made of quartz or glass [9, 10, 22, 23, 26, 44]. This provides the two arms to hold the two identical electrodes and the individual heating filament at each arm aid to establish the required temperature difference between the electrodes. The ionic diffusion between the electrodes happens through the bottom of the cell, like a salt bridge. Later reports have thermal insulating fire bricks or glass sleeves in between the two arms to maintain a stable and large temperature gradient between the electrodes.

Then a vertical cylindrical alumina crucible is used in a single vertical tube furnace, the different heat zones between the heating coils possess a small temperature difference [28, 63, 66, 71]. By positioning the two electrodes at different heat zone, the required temperature gradient of the thermocell measurement is established (**Figure 1.3.9 c**). Also, the use of the alumina cell components provides a stable operation at high temperature with molten salt electrolytes. The addition of the solid oxides into the molten salt electrolyte reduces the heat flux along with the easy handling of liquid electrolytes. It provides a stable temperature gradient and establishes the conditions for improved thermoelectric conversion [28, 63].

1.3.5 Evaluation of the molten salt thermocell performance

Almost all the available reports about the molten salt thermocells have carefully investigated only the fundamental parameters, such as Seebeck coefficient, transported entropy of the charge carriers, the heat of transport and Soret coefficient. However, the solid semiconductor thermoelectric generators and low temperature thermocells have been evaluated further in order to know the *power conversion efficiency*. The most common and basic parameter to find the suitability of semiconductor thermoelectric material is the *figure of merit* (ZT). The expression for thermoelectric generator power conversion efficiency is dependent on ZT [72].

$$\text{Dimensionless figure of merit (ZT)} = \frac{\sigma\,\alpha_s{}^2 T}{\lambda} \qquad (1.18)$$

where (σ) is electrical conductivity, (α_s) Seebeck coefficient, (T) cell average temperature and (λ) thermal conductivity.

In 1968 Cornwell [3] approximated this dimensionless figure of merit (~0.0001) for various single molten salt electrolytes. Then Kang *et al.* [63] has reported the figure of merit (0.05) of the molten carbonates electrolyte mixture dispersed with solid MgO for the thermocells with

($CO_2|O_2$) gas electrodes. The electrical and thermal conductivity of the electrolyte mixture was roughly estimated by using the weight fraction and the conductivity values of the individual molten carbonates and MgO. The molten salt thermocell figures of merits are comparatively negligible compared to the figure of merits (~1) of the solid semiconductor thermoelectric generators. This massive difference is mainly due to the physical transport of ions in the molten salt electrolyte [73].

The transport behavior of the liquid electrolytes thermocells is not identical to the solid semiconductor thermoelectric generators. The liquid electrolytes possess a net transfer of materials between the electrodes, which is not the case for solid semiconductors. Also, the electrical conductivity of the liquid electrolytes is not necessary to be constant and ohmic (linear I-V relationship). So, in the liquid electrolyte thermocells, it is suggested to directly determine the power conversion efficiency through a DC measurement, instead of using the dimensionless figure of merit [4, 11, 13].

The DC measurement can be performed by connecting a variable external load resistance in parallel to the thermocell. By using Ohm's law, the measured closed-circuit potential and the applied known load resistance are used to obtain a current vs voltage curve. The internal resistance of the thermocell will be equal to the applied external load resistance exactly at the half of the open-circuit potential.

Plotting the calculated current density against the power output density will result in a semicircle plot. The maxima of the semicircle is the maximum possible power output (P_{max}) of the thermocell at that experimental condition. Then the power conversion efficiency can be determined by the following expression containing P_{max}, instead of the figure of merits,

$$\text{Power conversion efficiency } (\eta) = \frac{P_{max}}{\lambda A\left(\frac{\Delta T}{\Delta x}\right)} \tag{1.19}$$

where (λ) is the thermal conductivity of the electrolyte mixture, (A) surface area of the electrodes, (ΔT) temperature gradient and (Δx) distance between the electrodes. Also, the power conversion efficiency can be related to the possible Carnot efficiency of the system,

$$\eta_r = \frac{\eta}{1-\left(\frac{T}{T+\Delta T}\right)} \tag{1.20}$$

where the denominator $\left(1-\left(\frac{T}{T+\Delta T}\right)\right)$ is the Carnot efficiency, temperature of cold (ΔT) and hot ($T + \Delta T$) electrodes. This approach used in the low temperature thermocells can be adapted to the high temperature molten salt thermocells, since the electrolyte transport behaviors are identical. Applicability of any power supply system relays on its power output than any other parameters. So, like other electrochemical energy devices, summing up the thermocells in series could deliver the required power.

1.3.6 Summary

The discrete developments in the electrolyte mixtures and electrode materials for the molten salt thermocells enhance its possibilities for high temperature thermal energy harvesting. Comparing the reports in this thermocells from the single molten salt electrolytes to molten salt composite electrolyte mixtures, the Seebeck coefficient improved to ~ -1.5 mV/K with gas electrodes and molten salt - solid oxide electrolyte mixtures. Also, the gas electrodes provide continuous operation and low maintenance compared to metal electrode thermocells. The progress in the molten salt thermocells suggests that the real-time applications of the high temperature thermocells are not too far away.

1.4 Aim and outline of the thesis

The literature review is considered as a reference point to proceed the research further on the high temperature molten salt thermocells. In this thesis, the thermocells with gas electrodes and molten carbonate-based electrolyte mixture will be investigated for more understanding and possible improvements.

The candidates proposed for investigation in this thesis are,

- Electrodes - gas flow rate and inexpensive metal current collector;
- Electrolyte mixture - solid oxide to molten carbonate ratio (vol%), molten carbonate composition, and various suitable solid oxides;
- A suitable approach to estimate the power conversion efficiency and the required parameters to compute it.

This thesis is a collection of 5 papers, which are included in Chapter 3 (results and discussion). A comprehensive experimental procedure is presented in Chapter 2. The Chapter 4 and 5 have the suggestions for future work and concluding remarks of the work. Based on non-equilibrium thermodynamics the detailed theoretical derivation for the Seebeck coefficient of the thermocell containing molten carbonate electrolyte mixture and gas electrodes is shown in Appendix A.

Paper 1: The electrode gas flow rate at the electrolyte interface was optimized to establish a well-equilibrated condition at the three-phase (electrode-gas-electrolyte) interface for a reliable potential measurement. Then studied the electrolyte mixture to identify the effective ratio of solid MgO to binary (Li,Na) carbonate. The stability and distribution of the dispersed solid MgO in the electrolyte mixture was analysed by using the XRD and EDS.

Paper 2: Using the optimizations from Paper 1, here the molten carbonate composition of the electrolyte mixture was tuned to operate the thermocell at low temperatures. Targeted to access the dual sources, like waste heat (~ 450 °C) and CO_2-rich off-gas (as electrode gas) from industrial aluminum production. The binary molten carbonate electrolytes are inactive below 500 °C due to its solid phase, so the possibilities of the ternary and quaternary carbonate mixtures were considered. The liquidus temperature and thermal stability of the electrolyte mixtures were studied by suitable thermal analysis.

Paper 3: The effect of the solid MgO surface area on the thermocell Seebeck coefficient and the figure of merits (ZT) were demonstrated. Both the initial and steady state (after 90 h) Seebeck coefficient were reported to show the long-term stability. In addition to the Seebeck coefficients, the thermal and electrical conductivity of the electrolyte mixtures were measured to compute the ZT. The thermal conductivity of the high temperature melts was measured by the simple heat flux DSC, for the first time. The accuracy in measuring the electrical conductivity of the electrolyte melt was improved by constructing a conductivity cell with capillary electrodes for AC impedance spectroscopy analysis.

Paper 4: Suitability of various selected solid oxides for the molten carbonate thermocell electrolyte mixture was studied. The phase and chemical stability of the solid oxides at the different stages of the thermocell operation was examined by XRD analysis. Also, the long-term stability of different solid oxides in the thermocell was shown by measuring the Seebeck coefficient at constant temperature difference at least for 90 h. The power output density of the thermocells were determined by DC measurement. Also, the power conversion efficiency was computed from power output density and thermal conductivity (reported in Paper 3).

Paper 5: Considering all the optimizations from Paper 1 - 4, in Paper 5 an alternate and inexpensive current collector to replace the gold current collector in the gas electrode was studied. The present compositions of the electrolyte mixture and electrode gas of the thermocell were analogous to the cathode side half-cell of the molten carbonate fuel cell (MCFC). So, in this study the suitability of the MCFC’s nickel-based cathodes to operate the molten carbonate thermocell was investigated.

Chapter 2 Experimental

Details pertaining to the laboratory play in setting-up and investigating the high temperature molten carbonate thermocells are described in this chapter. The physical, thermal and chemical characterizations considered to interpret the properties of the electrolyte mixtures and the electrode of the different thermocells are included. Also, the basic concepts and working principles of characterization instruments are briefly summarised.

2.1 Laboratory thermocell operation

2.1.1 Gas electrode fabrication

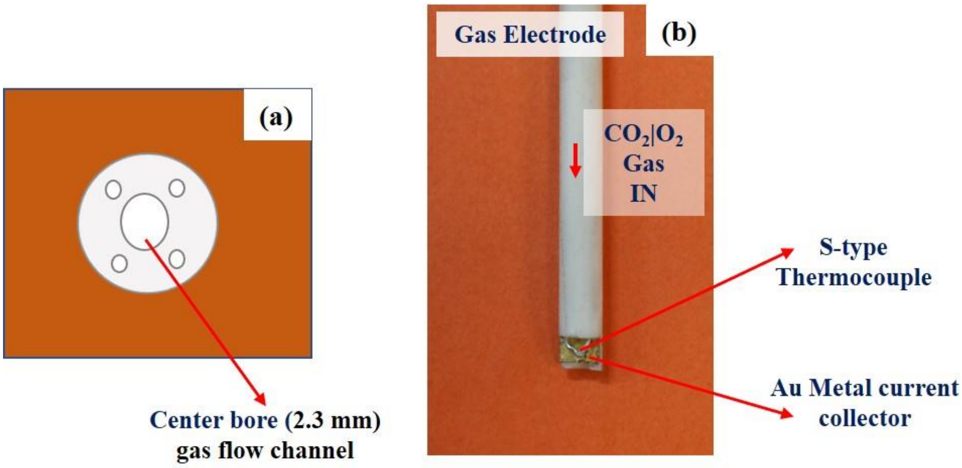
(a)
Center bore (2.3 mm) gas flow channel
Gas Electrode
(b)
$CO_2|O_2$ Gas IN
S-type Thermocouple
Au Metal current collector

Figure 2.1.1 The gas electrode fabrication **(a)** 5-bored alumina tube and **(b)** the metal current collector and S-type thermocouple arrangement in the alumina tube.

Figure 2.1.1 shows the gas electrodes employed in the high temperature thermocells. The sintered alumina components are highly stable in the corrosive molten carbonates melt at such high temperatures. So, the alumina components obtained from MTC Haldenwanger, Germany was used to assemble the entire thermocell. The gas electrodes were prepared by using an alumina tube (5 mm outer diameter and 550 mm length) with one center bore of diameter 2.3 mm and four other bores with 0.75 mm diameter (**Figure 2.1.1 a**). Pure gold, platinum and platinum with 10% rhodium (in the form of a wire 0.5 mm dia and sheet 0.5mm thick) from K.A. Rasmussen, Norway was used to fabricate the electrode current collector and thermocouples. Later, nickel-based current collectors were also fabricated by using the pure nickel (sheet 0.5 mm thickness and wire 0.5 mm dia) obtained from Alfa Aesar.

In **Figure 2.1.1 b**, the alumina tubes were machined to have a narrow groove cut to hold the metal current collector along the gas channel, i.e. the center bore (2.3 mm dia) of the alumina tube. Then the wire lead to the metal current collector was inserted into the center bore (diameter 2.3 mm). A detailed fabrication of the metal current collector will be discussed below. An S-type thermocouple was inserted into two holes (diameter 0.75 mm) and the junction was positioned as near as possible (without touching) to the metal current collector surface. The S-type thermocouples were made by welding the pure Pt and Pt10%Rh wires. Thermocouples were calibrated at various temperatures between 500-700 °C using a standard reference thermocouple. An intermediate copper external reference junction (as cold junction compensation) connects the thermocouples to the measuring unit. For each experiment a new pair of electrodes was used to fabricate thermocells with different electrolyte mixtures to prevent contamination. The required electrode gas was obtained from AGA, Norway, as a pre-made mixture containing 34% oxygen mixed with carbon dioxide. The pre-made gas mixture was supplied through the alumina tube and continuously bubbled over the current collector surface at the electrolyte interface.

The gold metal current collector:

Here the gold metal current collector was fabricated by the gold sheet (5 x 5 mm) spot-welded to the gold connecting wire leads. During the spot-welding, the metal sheet and connecting wire lead were fused by a hammer punch after melting them partially in oxyhydrogen gas flame.

Nickel-based metal current collector:

As-purchased nickel sheet was spot-welded to the gold wire in a similar way as mention above. Then the fabricated nickel current collector was converted into nickel oxide (NiO) or lithiated nickel oxide ($Li_xNi_{1-x}O$) phase before fixing it to the alumina tubes.

(i) Ni to NiO conversion: The nickel current collector was heated at 700 °C (heating rate of 200 °C/h) for 4 h in a tube furnace under synthetic air. Then it was cooled naturally in the same atmosphere to avoid the quenching effect and formation of impurities.

(ii) Ni to $Li_xNi_{1-x}O$ conversion: High purity (> 99%) carbonates of lithium and potassium were mixed (by hand in a mortar) in eutectic composition and dried in a hot air oven for 48 h at 200 °C. Then, a 90 g sample of the prepared eutectic $(Li,K)_2CO_3$ was melted at 650 °C for 24 h in a flat-bottomed alumina crucible (**Figure 2.1.2**) placed inside the vertical cylindrical furnace under N_2 atmosphere. A pair of Ni metal current collectors supported by alumina tubes was inserted into the melt. A separate alumina tube was used to supply the oxidizing gas mixture at a flow rate of 21 ml/min and the melt temperature was monitored by an S-type thermocouple placed in the electrolyte.

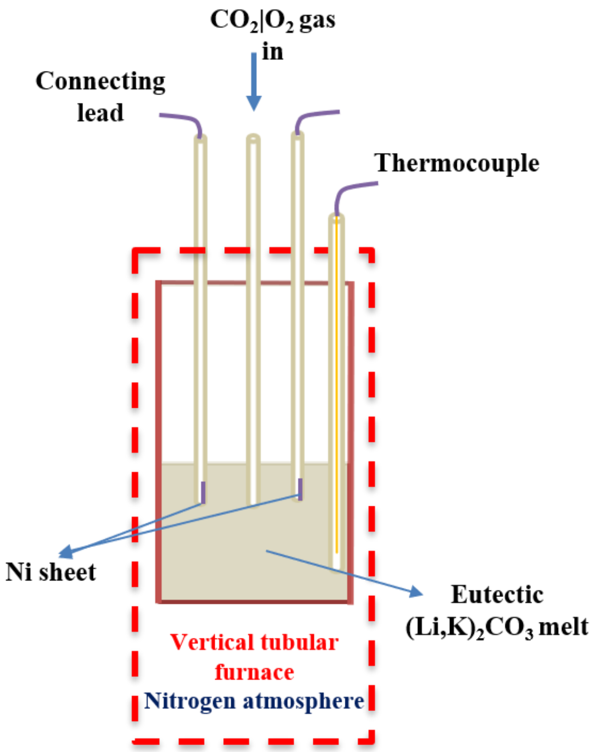

Figure 2.1.2 In-situ lithiation of the Ni electrodes to attain $(Li_xNi_{1-x}O)$ phase.

This in-situ lithiation process was continued for 100 h. Then the gas mixture flow was stopped and the metal current collectors were pulled out from the melt. But the metal current collectors were held inside the furnace at 650 °C for 4 h before cooling, to facilitate the electrolyte melt to completely drop down from its surface.

2.1.2 Electrolyte preparation

For preparing the electrolyte mixtures, all the required chemicals were purchased in high purity (> 99%) grade. The lithium, sodium, potassium and calcium carbonates; lithium fluoride and solid oxides (MgO, CeO_2, $LiAlO_2$ and Al_2O_3) were bought from Sigma-Aldrich. The MgO powders were also bought from Fluka and Acros organics for different particle sizes. As-purchased chemicals were used without any further purification.

The chemicals were mixed thoroughly by hand in a mortar with the appropriate weight to make up the exact eutectic composition of molten carbonates and certain volume percent of the solid oxide. To remove the moisture, the prepared electrolyte mixtures were dried in a hot air oven for 48 h at 200 ºC. The detailed electrolyte mixture composition can be found in the respective short experimental section (each paper) available in Chapter 3.

2.1.3 Thermocell setup

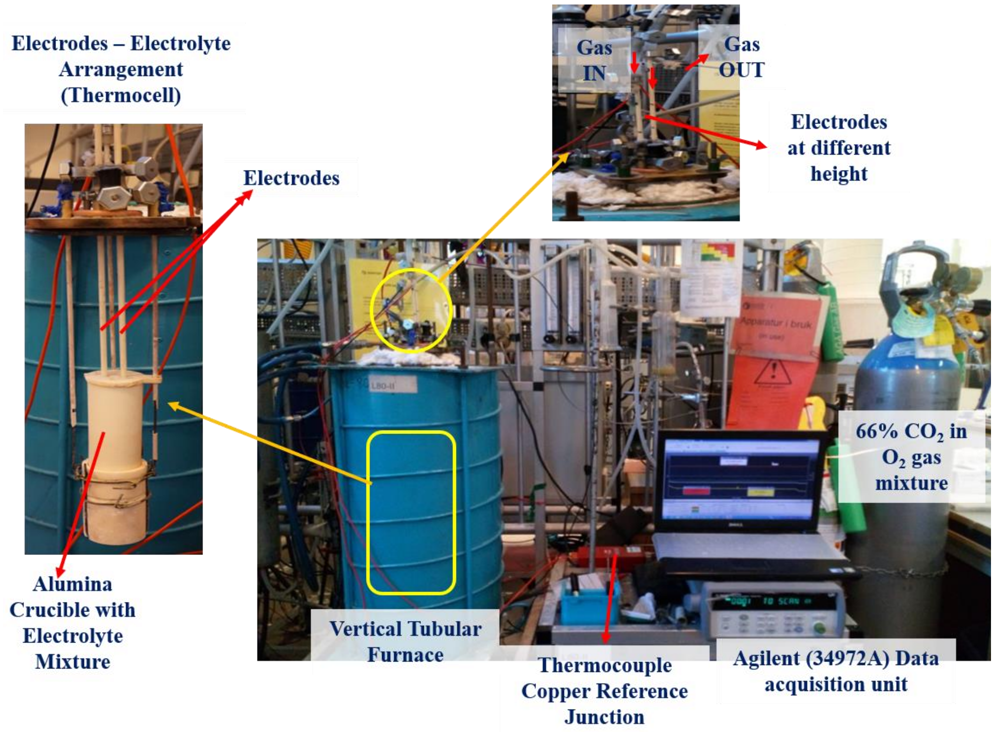
Electrodes – Electrolyte Arrangement (Thermocell)
Gas IN
Gas OUT
Electrodes at different height
Electrodes
66% CO_2 in O_2 gas mixture
Alumina Crucible with Electrolyte Mixture
Vertical Tubular Furnace
Thermocouple Copper Reference Junction
Agilent (34972A) Data acquisition unit

Figure 2.1.3 The laboratory thermocell construction and apparatus.

Approximately 120 g of the dried electrolyte mixture was filled in a cylindrical crucible (inner diameter of 38 mm with 200 mm length). Then, two Al_2O_3 tubes with the electrode arrangement were placed in the crucible as shown in **Figure 2.1.3**. The constructed thermocell was transferred to a standard laboratory vertical cylindrical furnace under N_2 atmosphere.

The copper leads closing the furnace tubes were specially designed to match the thermocell electrode arrangement and gas flow. The electrode supporting alumina tubes were held by a piece of silicone hose to facilitate the repositioning of the electrodes during operation, a high vacuum grease was applied to seal the gas leak. Cold water was continuously circulated over the furnace walls and copper leads during the operation. First, the electrolyte mixture was melted at the average cell temperature at least for 48 hours to ensure the homogeneous melt condition.

Then the electrode gas was supplied to the alumina tubes holding the current collectors through a pair of flowmeters from Brooks instrument Sho-Rate meters (± 5% accuracy) at flow rate of 21 ml/min. An Agilent (34972A) data acquisition unit recorded the temperature of the electrodes and the cell potential continuously (interval of 10 sec). The temperature of the electrodes was measured through a copper (cold) compensation junction box.

2.1.4 Seebeck coefficient measurement

After the melting step for 48 h and supplying the electrode gas mixture, the thermocell was ready for the Seebeck coefficient measurement. Initially, both electrodes were positioned at the average cell temperature (same height) to determine the bias potential for $\Delta T = \sim 0$ °C. Then the electrodes were repositioned to different locations to establish a systematic temperature gradient (ΔT in step of 5 between -20 and 20 °C) as shown in **Figure 2.1.4**.

Placing the electrodes at different heights creates the temperature gradient (ΔT) due to the difference in heating zones between heating coils of the furnace. However, the average cell temperature was maintained to be constant at all ΔT, i.e. $(T_h + T_c)/2 = 550$ °C, where T_h and T_c are the temperatures of hot and cold electrodes.

The initial 15-20 min was considered as an equilibrium time to establish a steady temperature gradient. So, the potential ($\Delta\varphi$) was measured at least for 20 min after the equilibrium time at each ΔT to determine the Seebeck coefficient $\left(\frac{\Delta\varphi}{\Delta T}\right)$. Therefore, the recordings were made over some 50 minutes for each temperature difference to make sure that the measured potential was stable. Even then, it was considered being an initial time measurement in a short time after establishing the required temperature gradient. To determine the Seebeck coefficient at (long-term) Soret equilibrium state, the potential was recorded at a certain temperature gradient at-least for 90 h.

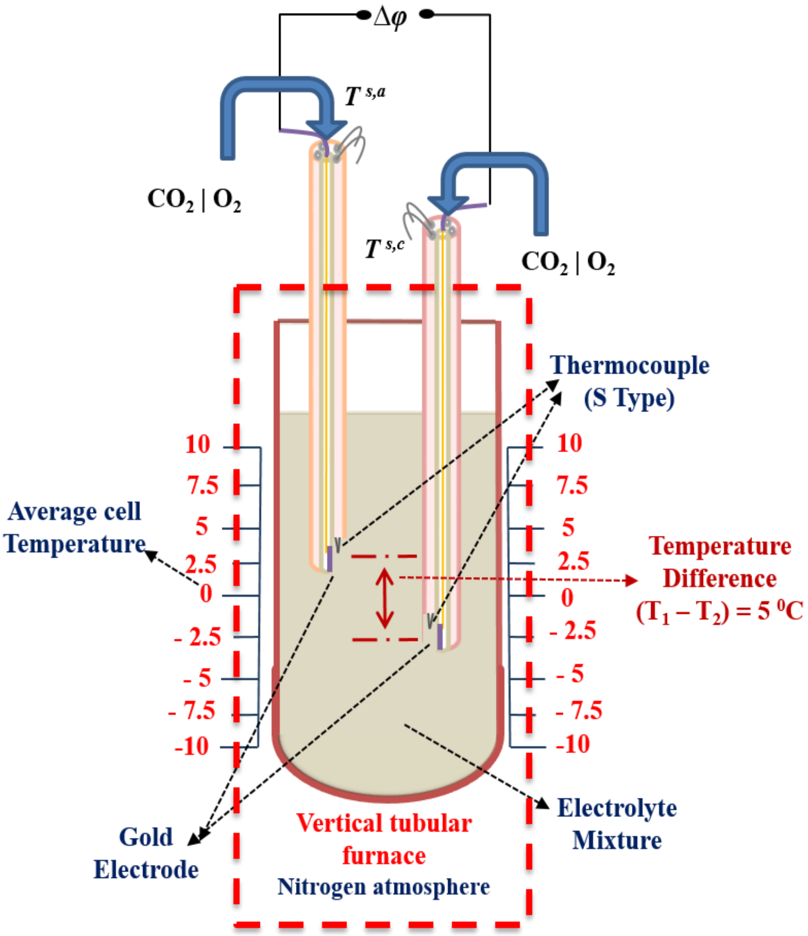
Δφ
$T^{s,a}$
$T^{s,c}$
CO_2 | O_2
CO_2 | O_2
Thermocouple (S Type)
Average cell Temperature
Temperature Difference
$(T_1 - T_2) = 5\ ^0C$
10
7.5
5
2.5
0
- 2.5
- 5
- 7.5
-10
Gold Electrode
Electrolyte Mixture
Vertical tubular furnace
Nitrogen atmosphere

Figure 2.1.4 The cross-sectional schematic representation of the molten carbonate thermocell. The electrodes are positioned to establish the temperature gradient of 5 °C.

2.1.5 Power output measurement

After the long-term Soret equilibrium state measurements, the power output of the thermocell was measured by a direct current (DC) measurement. For the DC measurement, a variable load resistance (R_{ext}) was introduced in parallel to the thermocell and the measuring unit (**Figure 2.1.5**).

The external load resistance was decreased from 10 MΩ to 1 Ω and the corresponding change in potential was recorded after 30 sec from the time of the change in each resistance point.

Later these measured potentials and applied known resistance loads were used to estimate the current according to the Ohm's law and then converted into power output.

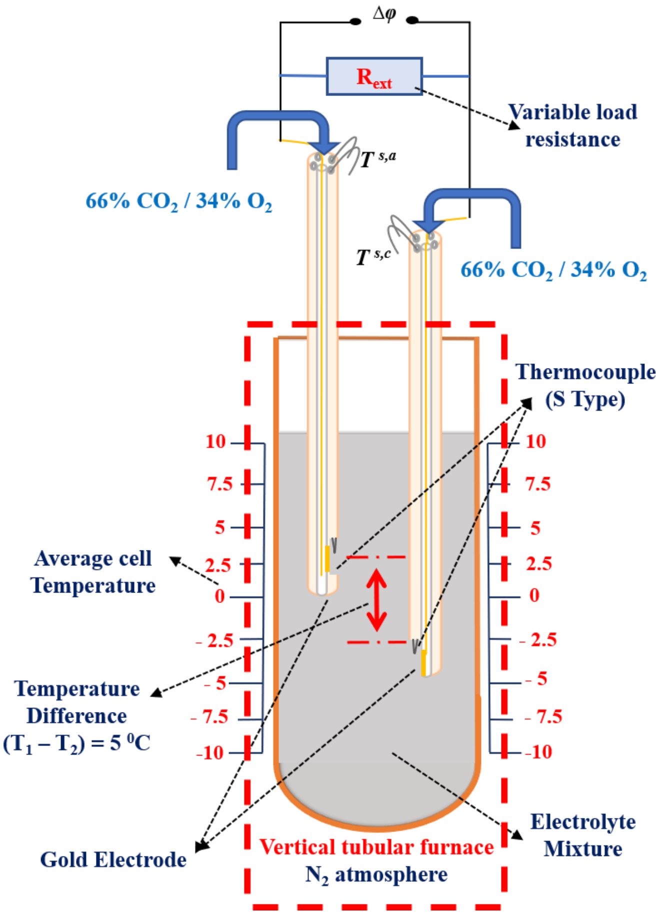
Δφ
R_{ext}
Variable load resistance
$T^{s,a}$
66% CO_2 / 34% O_2
$T^{s,c}$
66% CO_2 / 34% O_2
Thermocouple (S Type)
10
7.5
5
2.5
0
- 2.5
- 5
- 7.5
-10
Average cell Temperature
Temperature Difference ($T_1 - T_2$) = 5 °C
Gold Electrode
Vertical tubular furnace
N_2 atmosphere
Electrolyte Mixture

Figure 2.1.5 The cross-sectional schematic representation of the thermocell connected with external resistance in parallel for power output measurement.

2.2 Materials characterization

2.2.1 Structural and phase analysis - XRD

The chemical and phase stability of the electrolyte mixtures and electrodes at different stages of the thermocell operation was inspected in D8 Advance X-ray diffractometer (XRD) from Bruker.

Principle:

A primary X-rays source is made to fall on the sample, due to the wave-like nature the X-ray gets diffracted to a certain angle. The diffraction beam angle will differ from the angle of the incident beam. This difference in angle gives the information regarding the crystal nature of the sample. The basic of diffraction is the *Bragg's law* ($n\lambda = 2d \sin\theta$), where λ is the wavelength of the X-ray beam, d is the spacing between the planes in the atomic lattice, θ is the angle between the incident ray and the scattering plane and n is an integer. When the Bragg's law condition is satisfied, the scattered beams from different planes interact constructively and result in an intense reflected wave (diffracted beam).

Sampling and measurement:

The XRD analysis requires a precise and careful sample preparation to obtain the diffraction pattern with minimal error. The electrolyte mixtures and nickel-based current collectors were subjected to XRD analysis at different steps of the thermocell measurements.

(i) Electrolyte mixtures: Powders of the as-prepared electrolyte mixtures (i.e. before the thermocell measurement) was packed into the XRD powder sample holders. An adequate amount of powder was used to fill exactly to match the holder surface. Then the upper surface was carefully flattened without altering the random distribution of lattice orientations.

Also, the re-solidified electrolyte mixtures after the thermocell measurements were collected from different regions and ground to obtain a fine powder. Then the powder was prepared for the XRD analysis as mentioned above. In certain cases, the re-solidified electrolyte mixture was washed with distilled water to wash out the molten carbonates. After three washing cycles (centrifugation - discard - redispersion) the sediment was dried at 200 °C for 24 h and the sample was subjected to XRD analysis.

(ii) Nickel-based current collectors: Like the electrolyte mixtures, the nickel-based current collector was also subjected to XRD analysis at different steps of the thermocell measurement. The as-purchased Ni sheet, after NiO conversion in synthetic air, lithiated Ni phase and the current collectors after the thermocell measurements were analyzed. Preparation of metal sheets for XRD analysis also requires a flat surface and was levelled exactly to the height of the sample holder. So, the metal sheets were mounted over a clay, as the clay was not exposed to the X-ray. Since the metallic gold was highly stable in this molten carbonate melts the gold electrodes were not subjected to XRD analysis.

All the samples were exposed to a CuKα source of $\lambda = 1.5406$ Å and the diffraction patterns were recorded between 15° and 75° (2θ) at a scan rate of 2°/min. The obtained XRD patterns were matched with the standard JCPDS reference patterns by using the EVA software for detailed phase analysis.

2.2.2 Melting point and thermal stability – DSC/TGA

The thermal stability and liquidus/solidification temperature of the electrolyte mixtures were determined by TGA and DSC thermal analysis (NETZSCH STA449C Jupiter).

Principle:

In thermal analysis, the changes in the physical properties of the sample by the application of heat or thermal energy is detected and correlated to the thermal properties.

(i) Thermogravimetric Analysis (TGA): The change in sample weight is measured while heated at a constant rate (or at constant temperature). Here the equilibrium of the micro-balance gets affected by the change in sample mass, and to recover equilibrium it generates an additional electromagnetic force. The amount of additional electromagnetic force will be proportional to the change in the mass of the sample. TGA is an effective quantitative analysis of the thermal reactions accompanying the change in mass. Such reactions are evaporation, decomposition, gas absorption, desorption and dehydration.

(ii) Differential Scanning Calorimeter (DSC): Here the sample and a reference material are heated or cooled simultaneously at a constant rate. The difference in temperature between them is proportional to the difference in heat flow (from the heating source i.e. furnace) between the two materials. This technique determines the melting point, glass transition temperature, and endothermic and exothermic behavior.

Sampling and measurement:

The NETZSCH STA449C Jupiter facilitates simultaneous TGA & DSC measurement and records both the heat flow (DSC) and the weight changes (TGA) in a sample as a function of temperature or time. Both the analyses were performed by heating the as-prepared electrolyte mixture in a standard DSC alumina pan. Here, approximately 20 mg of the electrolyte mixture was gently pressed in the alumina pan and heated in reference with a similar empty alumina pan, under N_2 atmosphere. Before measuring the electrolyte mixtures, a blank measurement was performed with two similar empty alumina pans for background correction. Both the blank and real measurements were carried out with the same measurement program and under same atmosphere. The alumina pan was reused after a thorough clean in distilled water and acetone. The measurement program for each set of samples is specified in Chapter 3.

2.2.3 Solid oxide particle size

The particle size distributions of the as-purchased solid oxide powders were determined by using the HORIBA, LA-960 laser diffraction particle size analyzer. Laser diffraction was one of the reliable methods for estimating the particle size of powders, particularly in the range from 0.5 to 1000 μm.

Principle:

The powder sample subjected to the analysis was dispersed in a suitable liquid medium. A laser beam is allowed to scatter by the particles, the angle of light scattering is inversely proportional to particle size (i.e. smaller particle size gives a large angle of scattering). The angular scattering data calculate the particles size by using the Mie theory of light scattering. Here the refractive index of the particles, the dispersion media and the imaginary part of the refractive index of the particles are used to estimate the particle size as a volume equivalent sphere diameter.

Sampling and measurement:

For this analysis, a small quantity of the solid oxide powder was directly dispersed in the sample cell of the apparatus by using a suitable liquid (**Table 2.2.1**). The powder was mechanically and ultrasonically stirred before the measurement, to disperse the powder more homogeneously. A slow stirring was maintained during the measurement to keep the particles in suspension. Each sample was repeatedly analysed at least for three times to confirm the consistency of the obtained results. The refractive index of the solid oxides and the respective liquid medium used in the analysis are in **Table 2.2.1**. Solid MgO may slightly dissolve in water while other oxides are highly stable, so the MgO was dispersed in ethanol to prevent its solid-state for the analysis.

Table 2.2.1 Details of the samples subjected to laser particle size analyzer.

Solid Oxide	Refractive index of the solid oxide	Dispersant Liquid Medium	Refractive index of the medium
MgO	1.74	Ethanol	1.36
Al_2O_3	1.76	Distilled water	1.31
$LiAlO_2$	1.62		
CeO_2	2.2		

2.2.4 Surface area of the solid oxides – BET

The specific surface area of the as-purchased different MgO powders was determined by Brunauer-Emmett-Teller (BET) method using TriStar 3000 surface area and porosity analyzer.

Principle:

The gas adsorption analysis is one of the traditional approaches to determine the surface area and porosity of solid materials. Here the solid sample is exposed to a gas at a certain condition and the amount of gas absorbed by the sample determines the surface area (m^2/g). The specific surface area determined by BET relates the total surface area (reactive surface) including pores in the surface.

Nitrogen is commonly used as the gas probe in BET analysis and the investigation is performed at liquid nitrogen conditions (i.e. 77 K). The surface area of the solids is evaluated from the monolayer capacity in the known cross-sectional area (16.2 $Å^2$/molecule) of the nitrogen molecules.

Sampling and measurement:

The solid MgO powder samples (~ 0.5 g) were first degassed to remove the gases and vapours that physically adsorbed on the surface. Then the degassed samples were preserved in vacuum at 200 °C for 12 h and subjected in BET analysis, and a filler rod was used in the sample glasses to reduce the measurement error. The nitrogen gas adsorption isotherm was recorded to calculate the specific surface area.

2.2.5 Electrode surface morphology – SEM

The change in the surface morphology of the gold and nickel-based current collectors after experiments was detected by a Hitachi S-3400N Scanning electron microscope (SEM).

Principle:

In this technique, an electron beam focused by electromagnetic lenses scans the sample surface, and all the essential components and the entire beam path is organized in a high vacuum chamber. The incoming electron beam interacts with the sample surface and get scattered as backscattered electrons (reflected) due to elastic collision or releases secondary electrons due to inelastic collision. The scattered electron is fed to the detector and then into a cathode ray tube through an amplifier to obtain the magnified the images of the sample surface. The secondary electrons (SE) produce a high-quality image with the great possibility of magnification. Whereas the backscattered electrons (BE) produce a worse quality image but reveal the information about sample composition. So, the most common SEM mode is the detection of SE emitted by atoms excited by the electron beam. By scanning the sample and collecting the SE that are emitted using a special detector, an image displaying the topography of the surface is created.

Sampling and measurement:

The nickel sheet was subjected to SEM analysis after the different processes, such as the as-purchased Ni sheet, after lithiation ($Li_xNi_{1-X}O$), NiO phase after being oxidized in synthetic air. The Ni current collector after the thermocell measurements was also analyzed to explain the surface corrosion. In some cases, the gold current collectors after thermocell measurements with different electrolyte mixtures were also subjected to SEM analysis.

All the above-mentioned samples had a suitable dimension (5 x 5 mm) for the SEM analysis, so they were analyzed without any further sampling. The samples were fixed on the sample supporters (stubs) by a conductive double-sided adhesive carbon tape. Since these metal samples are electrically conductive, no additional conductive coating was applied. The secondary electrons (SE) were detected, and the surface morphology of the samples were pictured in identical and comparable magnifications.

2.2.6 Solid oxides distribution in the electrolyte mixture – EDS

Energy Dispersive X-ray Spectroscopy (EDS or EDX) systems are typically integrated with SEM apparatus. In this study, an EDS system from Oxford instrument Aztec attached to the Hitachi S-3400N SEM was used to study the elemental composition of the re-solidified electrolyte mixtures.

Principle:

Since EDS was integrated with SEM, the same primary electron beam is used to interact with the sample. In addition to the backscattered (BE) and secondary (SE) electron as mentioned in SEM, it also causes the emission of X-ray fluorescence lines. The characteristic X-ray lines are named according to the shell in which the initial vacancy occurs and the shell from which an electron drops to fill that vacancy. These lines provide the qualitative and quantitative information on the chemical composition of the sample.

Sampling and measurement:

The re-solidified electrolyte mixtures were collected from various regions of the thermocell after the short time Seebeck coefficient measurements. A pinch of the re-solidified mixture (powder) was sprinkled gently on the carbon tape stacked on the sample stub. It was then tapped to remove the loosely held powder before transferring the samples to the SEM chamber. The front beryllium window in the detector absorbs low-energy X-rays. Thus, EDS cannot detect the presence of elements with atomic number less than 5 which includes Li. So other than Li, all other possible elements in the electrolyte mixture could be detected.

2.3 Transport properties

2.3.1 Thermal conductivity – DSC

In section 2.2.2, the Netzsch STA-449C Jupiter Thermo-microbalance was explained to estimate thermal properties by DSC and TGA analysis. Here the same DSC approach was employed to estimate the thermal conductivity of the electrolyte mixtures with a slightly modified experimental procedure.

Principle:

As mentioned earlier, the DSC measures the difference in heat flow (from the heating source i.e. furnace) to the sample. But to estimate the thermal conductivity it was essential to know both the heat flow into and out of the sample. The heat flow out of the sample can be indirectly determined by placing a pure metal (reference metal) above the sample. The change in melting behavior (shift in melting point) of the pure metal can reveal the heat flow out of the sample. So, knowing the heat flow into and out of the sample, gives the delay in heat flow i.e. thermal conductivity of the sample.

Sampling and measurement:

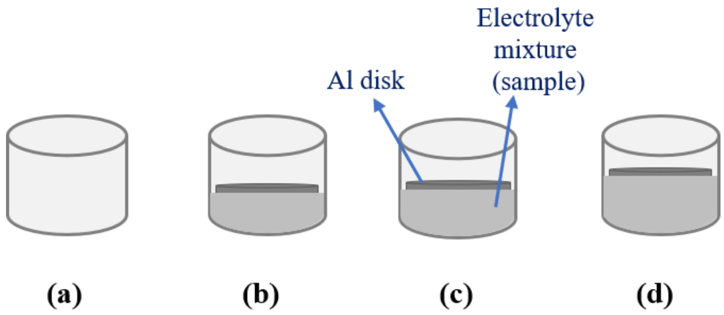

Figure 2.3.1 The DSC sampling for the thermal conductivity measurement **(a)** blank measurement, **(b,c,d)** with different quantity of electrolyte mixtures (30, 45, 60 mg).

The equipment was calibrated by measuring the melting point of selected high temperature DSC standard metals. Here pure aluminum metal was chosen as reference metal to monitor the heat flow out of the sample, and it was machined as flat surfaced disks (5 mm dia and 1 mm thick). The dried as-prepared electrolyte mixture was packed (gently pressing) in a cylindrical alumina pan (~ 5.8 mm inner-dia) and an Al disk was pressed softly over the sample (**Figure 2.3.1**). A blank measurement was performed before measuring the samples. Then an empty pan was replaced by the pan loaded with the sample. The heat flow through the sample was recorded as a function of temperature concerning the empty pan in the other compartment. The measurements with blank and samples were performed under the nitrogen atmosphere. A new pan and Al disk were used for each measurement, and the disks were machined symmetrically to each other (weight of 52.8 mg with ± 0.3 error).

Table 2.3.1 The DSC temperature program used for thermal conductivity measurement.

Segment	Mode	Temperature (°C)	Rate (°C/min)	Hold Time (min)	Time Required (min)
1	Dynamic (Heating)	30 - 515	20	---	24
2	Isothermal	515	---	15	15
3	Dynamic (Cooling)	515 - 410	20	---	5
4	Dynamic (Heating)	410 - 515	20	---	5
5	Isothermal	515	---	15	15
6	Dynamic (Cooling)	515 - 410	20	---	5
7	Dynamic (Heating)	410 - 650	20	---	12
8	Dynamic (Heating)	650 - 690	5	---	8
9	Dynamic (Cooling)	690 - 30	20	---	33

The melting behavior of the Al disk was the only essential data to estimate the thermal conductivity. The samples were heated by a slow heating rate (5 °C/min) in this particular temperature range. However, the heating/cooling rates were relatively fast (20 °C/min) in other temperature ranges (**Table 2.3.1**) to shorten the analysis time. The measurement was carried out for the same electrolyte mixture in three different quantities (30, 45 and 60 mg) for accuracy (**Figure 2.3.1**).

2.3.2 Thermal conductivity - LFA

A Netzsch 457 MicroFlash was used to measure the thermal conductivity of binary eutectic $(Li,Na)_2CO_3$ electrolyte in a mixture with 55 vol% of MgO. To compare the reliability of the above stated DSC approach, the thermal conductivity of such mixtures was measured.

Principle:

A laser pulse of 1 ms width or less momentarily heats the front side of the sample, and the subsequent change in temperature on the other side of the sample is measured by an infrared detector. The rise in temperature at backside get stable after attaining a uniform temperature distribution in the sample. The half-time ($t_{1/2}$ - time value of half signal height) to reach the equilibrium and the sample thickness reveals the thermal diffusivity (α).

Sampling and measurement:

A special sample container (Pt 10% Rh) with the top lid from Netzsch was used to analyse the molten carbonate mixture above its melting point 500 °C. The outer surface of the container was coated with a thin layer of graphite to avoid laser reflection at the container surface. A specific amount of the sample (0.2 g) was used to fill the container to establish a constant contact between the container-sample-lid. It may avoid the circumstance of empty interface layer and perturbation in result accuracy. The electrolyte mixture (sample) was compacted into a circular disk (10 mm diameter) in a hydraulic press with a load of 250 kg. Then the sample was heated to the required analysis temperature in the LFA apparatus under nitrogen atmosphere. After establishing the required temperature, the sample was exposed to 5 successive laser shots with an interval of 1 min between each successive shot. The LFA analysis was repeated with the same mixture to confirm the reliability of the results.

The estimated thermal diffusivity (α) in the LFA measurement was converted into thermal conductivity (λ) by the expression ($\lambda = \alpha.\rho.\mathrm{Cp}$). The heat capacity ($C_p$) was estimated by the direct conversion method from the DSC measurement in section 2.2.2. The density (ρ) of the electrolyte mixture at the higher temperatures was calculated from the thermal expansion data measured by a push rod dilatometer.

Thermal expansion - Push rod dilatometer:

The thermal expansion of the electrolyte mixture was measured by heating it in a pushrod dilatometer DIL 402 C from Netzsch. For dilatometer analysis, a cylindrically shaped pellet (5 mm dia) was prepared with ~ 0.25 g of the sample powder by applying a load of 250 kg in a hydraulic press. The pushrod dilatometer apparatus is compatible only with analysis of the solid-state samples. So, in this study the maximum temperature of the heating was limited to 300 °C (sample melts at ~ 495 °C), i.e. restricted to at least 100 K below the melting point. A standard alumina sample was used in blank measurement for background correction. Here a slow rate (2 K/min) was used for both heating and cooling, and the measurement was performed under nitrogen atmosphere. The measured thermal expansion was used to calculate the change in density. Then the estimated density at the solid-state was extrapolated to the higher temperature and approximated the density for the melt phase.

2.3.3 Electrical conductivity - AC impedance spectroscopy

The electrical conductivity of the electrolyte mixtures with different solid MgO particles was estimated by AC impedance spectroscopy. A conductivity cell with capillary electrodes was constructed to attain the measurement in melt phase at 550 °C, under the controlled current path. The PARSTAT 4000+ potentiostat from the Princeton Applied Research, controlled by VersaStudio software was used to perform the AC impedance spectroscopy.

Principle:

An alternating signal of small amplitude (5 to 20 mV) was applied to the electrochemical cell, and the corresponding current response is measured by varying the frequency of the applied signal. Since the disturbance by the potential (ΔE) is sinusoidal then the current (ΔI) in response will also be sinusoidal at the same frequency but differ in phase by comparing the applied signal. The initial disturbance and the response of the electrode is determined by comparing the phase shift and amplitude change between the current and voltage signals. Thus, the impedance (Z) measures the relationship between ΔE and ΔI. These factors depend on the rates at which physical processes in the electrochemical cell respond to the oscillating stimulus. Different frequencies can separate different processes that have different timescales. At lower frequencies, there is time for diffusion or slow electrochemical reactions to proceed in response to the alternating polarization of the cell. At higher frequencies, the applied field changes direction faster than the chemistry responds, so the response is dominated by capacitance from the charge and discharge of the double layer.

Sampling and measurement:

The conductivity cell with two capillary electrodes (**Figure 2.3.2**) was fabricated by using alumina components. The electrodes were made of a gold sheet (2 x 3 mm) point-welded to the gold wire (0.5 mm thick) and inserted into the alumina tube of outer diameter 4 mm. To implement the capillary effect, an alumina tube was extended to 3 cm above the tube holding the electrode (**Figure 2.3.2**). The inner diameter (4 mm) of the outer tube was chosen to be same as the outer diameter of the tube with the gold electrode. A separate alumina tube holding the thermocouple (S-type: Pt-Pt10%Rh) measured the electrolyte temperature. The electrolyte mixture was loaded into the cylindrical crucible, also packed into the electrode capillary space which was partially inserted into the electrolyte mixture. Then the assembled conductivity cell was transferred into a cylindrical furnace maintained with N_2 atmosphere, to perform the AC impedance spectroscopy at 550 °C.

First, the electrolyte mixture was melted at 550 °C for 48 h before inserting the capillary electrodes further down into the molten electrolyte. The impedance spectroscopy measurement was performed after 2 h from positioning the electrodes. A small sinusoidal voltage of 5 mV was applied to the cell in the frequency range of 5 MHz to 0.1 Hz, at the OCP ~ 0 V. The recorded spectrums were analyzed in the EIS spectrum analyzer software by fitting a suitable equivalent circuit to determine the resistance of the electrolyte mixture. Then the estimated resistance of the electrolyte mixture was used to estimate the electrical conductivity (σ) from the relation ($\sigma = (1/R_s)\ (l/A)$). Here, R_s is the electrolyte resistance measured by EIS, the l is the distance between the electrodes and A is the cross-sectional area of the current path. The ratio between the cell geometry (l/A) is generally known as the cell constant.

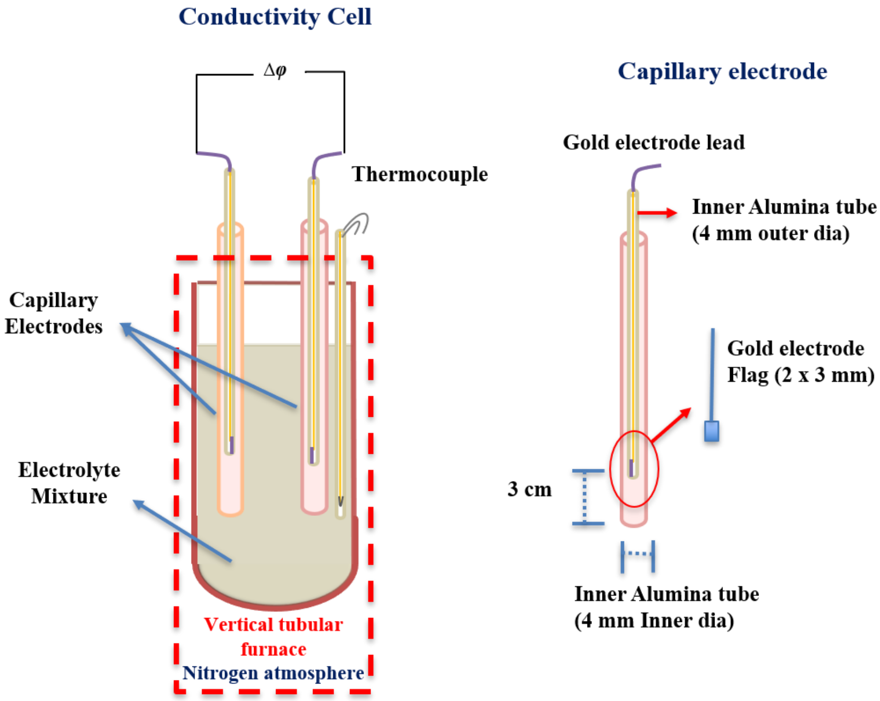
Conductivity Cell
Δφ
Thermocouple
Capillary Electrodes
Electrolyte Mixture
Vertical tubular furnace
Nitrogen atmosphere
Capillary electrode
Gold electrode lead
Inner Alumina tube (4 mm outer dia)
Gold electrode Flag (2 x 3 mm)
3 cm
Inner Alumina tube (4 mm Inner dia)

Figure 2.3.2 Schematic of the conductivity cell and capillary electrode used to measure the conductivity of the electrolyte mixtures by AC impedance spectroscopy.

The cell constant of the conductivity cell was determined by measuring the pure Li_2CO_3 at 750 °C. The electrical conductivity of Li_2CO_3 was well known and from the measured Li_2CO_3 electrolyte resistance, the cell constant was determined. The alumina cell components and gold electrodes are highly corrosion-resistant in the molten carbonate melts at high temperature and remain stable. The same cell components were used to measure all the electrolyte mixtures after a thorough wash in 10% HCl and water. Also, the capillary electrodes were inserted into the electrolyte mixture at the same height. By establishing the identical cell condition, the same cell constant was used to estimate the electrical conductivity of all the electrolyte mixtures.

Chapter 3 Results and Discussion

3.1 Paper 1

Influence of Electrode Gas Flow Rate and Solid Oxide Ratio in Electrolyte on the Seebeck Coefficient of Molten Carbonate Thermocell

S. Kandhasamy[a], L. Calandrino[b], O.S. Burheim[c], A. Solheim[d], S. Kjelstrup[e], and G.M. Haarberg[a]

[a] *Department of Materials Science and Engineering, Norwegian University of Science and Technology (NTNU), Trondheim, Norway*
[b] *Department of Mechanical and Industrial Engineering, University of Brescia, Brescia, Italy*
[c] *Department of Electrical Engineering and Renewable Energy, NTNU, Trondheim, Norway*
[d] *SINTEF Materials and Chemistry, SINTEF, Trondheim, Norway*
[e] *Department of Chemistry, NTNU, Trondheim, Norway*

Abstract

Thermocells represent a promising way to utilize heat as a power source. The aim of this work is to develop a thermocell with identical gas electrodes using molten carbonate-based electrolytes. The cell can generate power from waste heat and can also utilize the CO_2 *rich off-gas available in metal producing industries. The flow rate of the gas supply to the electrodes needs to be optimized. Its effect on the Seebeck coefficient was not studied systematically before. The addition of solid oxide to the molten carbonate melt alters also the system's Seebeck coefficient. We report measurements where we vary the content of solid oxide in the liquid eutectic electrolyte mixture as well as the electrode gas flow rate. The Seebeck coefficient is reported for various ratios of eutectic* $(Li,Na)_2CO_3$ *molten carbonate and dispersed solid oxide MgO, and for varying gas* $(CO_2|O_2)$ *flow rates to the electrode interfaces.*

J Electrochem. Soc., 164 (2017) H5271. DOI:10.1149/2.0391708jes

3.1.1 Introduction

Thermoelectric systems converting heat into electricity are well known since their discovery of the Seebeck effect in 1821 [1]. The thermoelectric power was first demonstrated for aqueous thermogalvanic cells, Quickenden *et al.* [4] summarized many similar systems in a review. However, because of their low figure of merit, due to the high thermal conductivity of water and their low operating temperature, they were not further investigated. Industrial metal production is associated with production of large amounts of thermal energy and high CO_2 emissions. Large amounts of heat are wasted by dissipation in the surroundings. Thermoelectric converters based on semiconductor materials may be used to generate electricity from such waste heat and Seebeck coefficients of 0.8 mV/K are typical [74]. However, the materials used in these devices are often scarce and expensive. The use of an ion-conducting electrolyte and gas electrodes offers possibilities of achieving high Seebeck coefficients [3, 62, 75]. Electrolytes such as ionic liquids and molten salts offer possibilities of higher stable operating temperatures and larger Seebeck coefficients than semiconductor thermoelectric materials [76, 77]. Experimental studies of electrochemical cells with inexpensive components such as molten carbonate electrolyte and $CO_2|O_2$ gas electrodes have been reported earlier. Seebeck coefficients in the range of -1.25 mV/K at average cell temperature of 750 ºC were obtained [28, 63].

A thermocell is an electrochemical system with identical electrodes placed at different temperatures in an electrolyte solution. In multicomponent mixtures, thermal diffusion is set up due to the temperature gradient between the electrodes. Ion transport between the electrodes due to the thermal driving force leads to a potential difference [4]. At steady state condition, a Soret equilibrium is achieved after a certain time. Seebeck coefficients are determined by measuring the initial as well as the steady state potential when a negligible current is passing through the cell.

A thermocell was demonstrated with different cell components, as metal/gas electrodes with liquid/solid electrolytes [2]. A small Seebeck coefficient was observed with metal electrodes M, in the thermocell $\mathrm{M(T)\mid MX\mid M(T+\Delta T)}$, here MX is the electrolyte with ions M^+ and X^-. Here T is the left hand side temperature and ΔT is the temperature difference between the electrodes. Dendrite growth, corrosion, and polarization may affect the thermoelectric conversion under operation. Gaseous electrodes X like in the thermocell $\mathrm{X(T)\mid MX\mid X(T+\Delta T)}$ are free from the above-mentioned deficiencies. Furthermore, the use of gas electrodes, include larger reaction entropies. Such electrodes may therefore deliver a higher electric potential than a thermocell with metal electrodes [10, 78]. The Seebeck coefficient of thermocells depends on the change in entropy of the half-cell reaction. The gas at the hot electrode, ionize and the cation is transported through the electrolyte to the cold electrode where the reverse reaction happens. The entropy change of the half-cell reaction is large, mainly because gas molecules disappear or appear. Important aspects for selection of electrolyte are the boiling point, a low vapor pressure, high electrical conductivity, low thermal conductivity and fast kinetics of the gas electrode. In favourable cases, the electrolyte mixture contains a reaction product of the electrode gas. This means chlorine from chloride melts, oxygen from an oxide containing electrolyte and carbon dioxide from molten carbonate mixtures [14, 17].

In this study, a gas mixture of $CO_2|O_2$ is used in the electrode gas to obtain a reversible electrode reaction. The reaction introduces the carbonate ion in a molten carbonate electrolyte mixture with solid-state MgO dispersed. The use of solid MgO in a molten carbonate was first reported by Jacobsen *et al.* [62]. Addition of a certain quantity of Al_2O_3 in molten AgI was reported to increase the ionic conductivity and the thermoelectric power [79]. The presence of a solid phase oxide matrix may reduce the heat flux between the electrodes. The so-called "figure of merit" is related to the thermoelectric power generation efficiency. It increases with an increasing Seebeck coefficient, a decreasing thermal conductivity and a decreasing electrical resistivity [4]. The use of non-critical and non-poisonous materials and the prospective of a high thermoelectric efficiency, as well as the availability of CO_2 gas, may be advantageous for the thermocell compared to semiconductor thermoelectric devices. The change in the Seebeck coefficient for similar thermocells with different carbonate melt compositions, electrode gas mixture, current collector, solid-state oxide and various average cell temperature has been reported before [28, 62, 63]. The content of the solid MgO phase and the flow velocity of electrode gas may influence the thermoelectric potential. This was not reported before and was systematically investigated in this work.

3.1.2 Theoretical considerations

The electrochemical cell with gas electrodes, reversible to the carbonate ion, held at different temperatures can be represented as:

$$\mathrm{Au}(T^{s,a}) \mid \mathrm{CO_2(g),O_2(g)} \mid \mathrm{(Li, Na)_2CO_3(l),MgO(s)} \mid \mathrm{CO_2(g),O_2(g)} \mid \mathrm{Au}(T^{s,c})$$

The electrochemical reaction at the left-hand side electrode is:

$$2\mathrm{CO_3^{2-}(l)} \rightarrow 2\mathrm{CO_2(g)} + \mathrm{O_2(g)} + 4\mathrm{e^-} \tag{3.1.1}$$

The reverse reaction takes place at the right-hand side. The Seebeck coefficient for the cell with uniform (homogeneous electrolyte) melt composition (short time) is:

$$\alpha_S = \left(\frac{\Delta\varphi}{(T^{s,c} - T^{s,a})}\right)_{j=0,t=0}$$

$$= -\frac{1}{F}\left[\frac{1}{2}\,S_{CO_2} + \frac{1}{4}\,S_{O_2} + S_e^* - \frac{1}{2}\,S_{CO_3^{2-}}^* + \left(\frac{t_2}{x_2} - \frac{t_1}{x_1}\right)\frac{q^*}{T}\right] \tag{3.1.2}$$

where S_j is the entropy of component j at average temperature of the electrodes T and pressure p_j. The terms S_e^* and $S^*_{CO_3^{2-}}$ are the transported entropy of the electron and carbonate ion, respectively. The entropies and the transported entropies are generally functions of temperature. The gas entropies are expected to be larger than the transported entropies. These terms have then a negative contribution to the Seebeck coefficient. Then t_1, t_2 are the transference coefficient and x_1, x_2 are the mole fractions of Li_2CO_3 and M_2CO_3. The ratio $\frac{q^*}{T}$ may be interpreted in terms of enthalpy changes across the layer, but it is difficult to interpret the sign of this last term. If the term is positive, the Seebeck coefficient at initial times is more negative than at infinite time, when the last term disappears. A detailed theoretical derivation of the equation based on non-equilibrium thermodynamics is explained in our previous work [28, 63].

3.1.3 Experimental

Table 3.1.1 Electrode gas flow rate and MgO to carbonate ratio used in the experiments.

Cell Label		$CO_2\vert O_2$ Flow rate		Weight %		Volume %	
		Scale Reading (NML/M)	Scale Conversion (ml/min)	MgO	Eutectic Mixture $Li_2CO_3 + Na_2CO_3$	MgO	Eutectic Mixture $Li_2CO_3 + Na_2CO_3$
Electrode Gas Flow Rate	A	40	14.7	55	45	44.3	55.7
	B	50	16.1				
	C	60	18.6				
	D	70	21.0				
	E	80	23.4				
Differential Ratio of MgO in Electrolyte	D	70	21.0	55	45	44.3	55.7
	F			65	35	54.7	45.3
	G			75	25	66.1	33.9
	H			85	15	78.7	21.3

Lithium carbonate (Li_2CO_3), sodium carbonate (Na_2CO_3) and magnesium oxide (MgO) were purchased from Sigma-Aldrich with purity > 99 %. The MgO powder has the average particle size of ~2.8 µm, measured in a laser scattering particle size distribution analyzer. Pre-made electrode gas mixtures containing 34% oxygen mixed with carbon dioxide were obtained from AGA, Norway. Gold sheet and wire for the electrodes and wires of platinum, platinum with 10% rhodium for thermocouple fabrication were obtained from K.A. Rasmussen, Norway. Alumina tubes (5 mm outer diameter and 550 mm length) with one center bore of diameter 2.3 mm and four other bores with 0.75 mm diameter and a tubular crucible (inner diameter of 38 mm with 200 mm length) were obtained from MTC Haldenwanger, Germany. The flow rate of electrode gas supplied through the ceramic tubes was controlled by a pair of Brooks Instrument Sho-Rate meters with ± 5% accuracy, both the scale reading and appropriate flow conditions for the gas used are shown in **Table 3.1.1**. The temperature of the electrodes and the cell potential were recorded every 10 seconds by using Agilent, 34972A data acquisition unit.

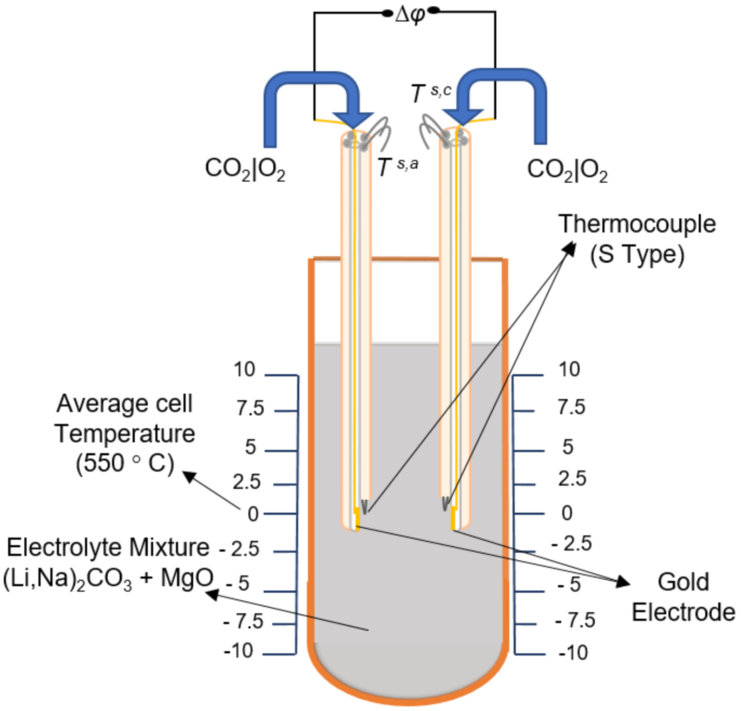

Figure 3.1.1 Cross sectional view of the thermocell with reference scale for positioning the electrode to create the required temperature gradient.

(Electrode positions for ΔT of 20 ºC was $T^{s,a}$ and $T^{s,c}$ at 10 and -10 position respectively, vice versa for ΔT of -20 ºC).

The thermocell was placed inside a standard laboratory vertical tubular furnace as shown in **Figure 3.1.1**. The cell consisted of an Al_2O_3 tubular crucible, with two electrodes immersed in a molten carbonate electrolyte mixture. In each alumina tube, the gold wire was inserted into the center bore (diameter 2.3 mm) of a 5-bore Al_2O_3 tube and the gold sheet (5 x 5 mm) was spot-welded to the wire. The thermocouple (Pt-Pt10%Rh) was inserted into two of the other holes (diameter 0.75 mm) and the junction was positioned as near as possible to the gold sheet. $CO_2|O_2$ gas was supplied through the bores of the ceramic tube. The electrolytes mixture was prepared by mixing the molten carbonates and MgO by hand in a mortar. The mixture was dried for more than 48 hours at 200 ºC. Then the electrolyte was melted under a nitrogen atmosphere at 550 ºC in the vertical tube furnace at least for 48 hours to ensure stable conditions. The ratio of Li_2CO_3 and Na_2CO_3 eutectic mixture and the dispersed solid MgO in the electrolyte mixture, as well as the $CO_2|O_2$ gas flow rate at the electrode/electrolyte interface, are listed in **Table 3.1.1** for the different cells.

A temperature difference (ΔT) was established between the electrodes by positioning them at different heights in the crucible. The average cell temperature was kept at 550 ºC and the temperature difference was always smaller than 20 ºC. The cell potential was measured as a function of the temperature difference, after an equilibration period of 15-20 min followed by a measurement with a new temperature difference. Recordings were made over some 50 minutes time at a certain temperature difference to make sure that the measured potential was stable. This is then taken as an initial time measurement. The cell measurements were performed using the same procedure as in our previous reports [28, 63]. At infinite time (meaning days) the last term in the equation (3.1.2) disappears.

The measurement conditions and the cases investigated are listed in **Table 3.1.1**. The table shows that we varied the MgO(s) content in the melt and the gas flow rate, keeping the electrolyte carbonate melt composition equal to the eutectic.

The phase analysis of the electrolyte mixture was carried out before and after thermocell measurements, using Bruker-D8 ADVANCE X-ray diffraction (XRD) with CuKα radiation ($\lambda = 1.5406$ Å). The elemental composition was also determined on the same samples by Energy Dispersive Spectroscopy (EDS) using an Oxford instrument Aztec EDS system attached to a Hitachi S-3400N Scanning Electron Microscopy (SEM). The front beryllium window in the detector absorbs low-energy X-rays. Thus, EDS cannot detect the presence of elements with atomic number less than 5 which includes Li, while all other possible elements in the electrolyte mixture were detected. The particle size distribution of the solid-state MgO powder was measured in Horiba LA-960 laser scattering particle size distribution analyzer, by dispersing the MgO powder in ethanol using ultrasonic bath.

3.1.4 Results and discussion

The results are presented in **Table 3.1.2** and **Table 3.1.3**, and **Figure 3.1.2** - **Figure 3.1.6**. The tables summarize results from the figures, for the case studies A-G listed in **Table 3.1.1**. We consider first the structure information on the system to have a background for discussion of the experimental results for the Seebeck coefficient variations.

Homogeneity of the electrolyte mixture:

The X-ray diffraction results of the electrolyte samples of Cells D and G, collected from various regions in the cell after the experiments are shown in **Figure 3.1.2 a** and **b**. The indistinguishable XRD patterns for the samples from the different regions (top, middle, bottom) confirm that the whole electrolyte mixture is homogeneous. A significant reduction in peak intensity of the molten carbonate can, however, be seen when we compare results from before (**Figure 3.1.2 c**) and after (**Figure 3.1.2 a**) the thermocell experiment. This can be understood as a poorer crystallinity of the carbonate mixture, attained during re-solidification in the presence of solid oxide. The absence of additional peaks before (**Figure 3.1.2 c**) and after (**Figure 3.1.2 a**) the thermocell measurements, suggests also that impurities are absent. That is, they have not been added in the melting or cooling process. From this absence, we can also conclude that electrolyte decomposition or carbonate reactions with MgO do not happen to any significant degree [80].

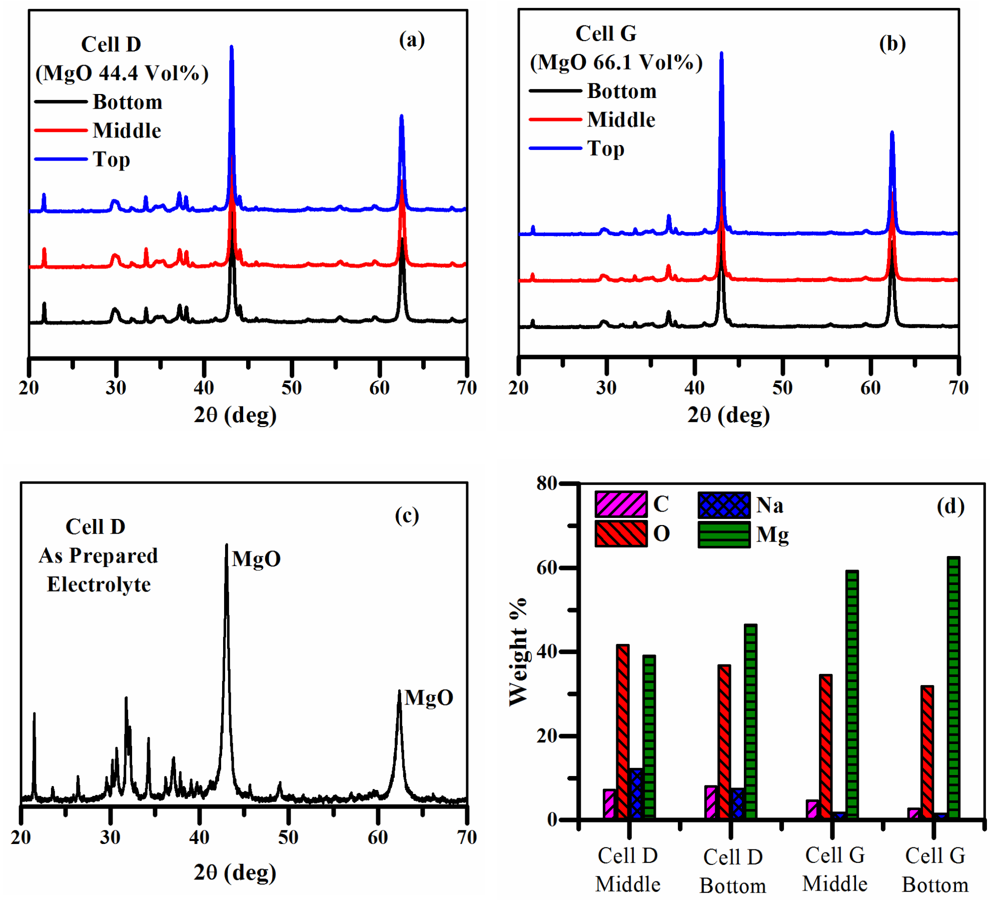

Figure 3.1.2 X-ray diffraction patterns for the electrolyte mixer after **(a,b)** and before **(c)** thermocell measurement. **(d)** EDS elemental analysis of the electrolyte after thermocell measurement (respective 1 sigma wt% error value was mentioned in the brackets).

The results from the EDS analysis on the used electrolyte are shown in **Figure 3.1.2 d**. They present more accurate information about elemental distribution than the XRD analysis. The

EDS results in **Figure 3.1.2 d** are average values from the analysis, over at least two different locations of each sample. Observations after the experiment in cell G indicate a ~ 3-5 wt % higher concentration of MgO at the bottom of the cells. This cell has a MgO content of 66.1%, see **Table 3.1.2**. But at the concentration used in most cells, 44.3% MgO (Cell D), the concentration is uniform. The extra solid phase at the bottom of cell G indicates that the dispersion has reached a solubility limit. Homogeneity seems to be maintained throughout the measurement with moderate content of MgO(s), < 66.1% with gas flow rates below 21 ml/min.

Table 3.1.2 Seebeck coefficient of the cells with varying electrode gas flow rate and average temperature 550 °C.

Cell Label	**CO_2|O_2 Flow rate (ml/min)**	**Volume %**		**Seebeck Coefficient (mV/ K)**	
		MgO	**Eutectic Mixture Li_2CO_3 + Na_2CO_3**	**Slope**	**Standard Error**
A	14.7	44.3	55.7	-1.1	0.03
B	16.1			-1.2	0.02
C	18.6			-1.6	0.03
D	21.0			-1.7	0.05
E	23.4			-1.0	0.03

These data altogether support the idea that there are no side reactions or concentration gradients in the electrolyte during the experiments listed in **Table 3.1.2**, and that equation (3.1.2) applies. Further support for equation (3.1.2) is obtained from the estimated time to reach Soret equilibrium. Recent simulations provide a diffusion coefficient of Li^+ in Li_2CO_3 at 550 °C equal to D = 1.4 10^{-9} m^2/s [81]. The distance between the electrodes h = 3.8 cm. The system characteristic relaxation time is therefore $\theta = h^2 /(\pi^2 D)$ = 29 hrs, cf. Kang *et al.* [63]. The stationary state value is reached after a time several times this value, i.e. several days. The steady state was obtained in our experiments within an order of magnitude 50 minutes, which then can be seen as an initial time measurement, compatible with the finding of uniform concentrations (see above).

Reversibility of the electrodes:

Table 3.1.3 Seebeck coefficient of the cells with different ratio MgO in electrolyte and average temperature 550 °C.

Cell Label	**CO_2|O_2 Flow rate (ml/min)**	**Volume %**		**Seebeck Coefficient (mV/K)**	
		MgO	**Eutectic Mixture Li_2CO_3 + Na_2CO_3**	**Slope**	**Standard Error**
D	21.0	44.3	55.7	-1.7	0.05
F		54.7	45.3	-1.7	0.04
G		66.1	33.9	-1.7	0.06

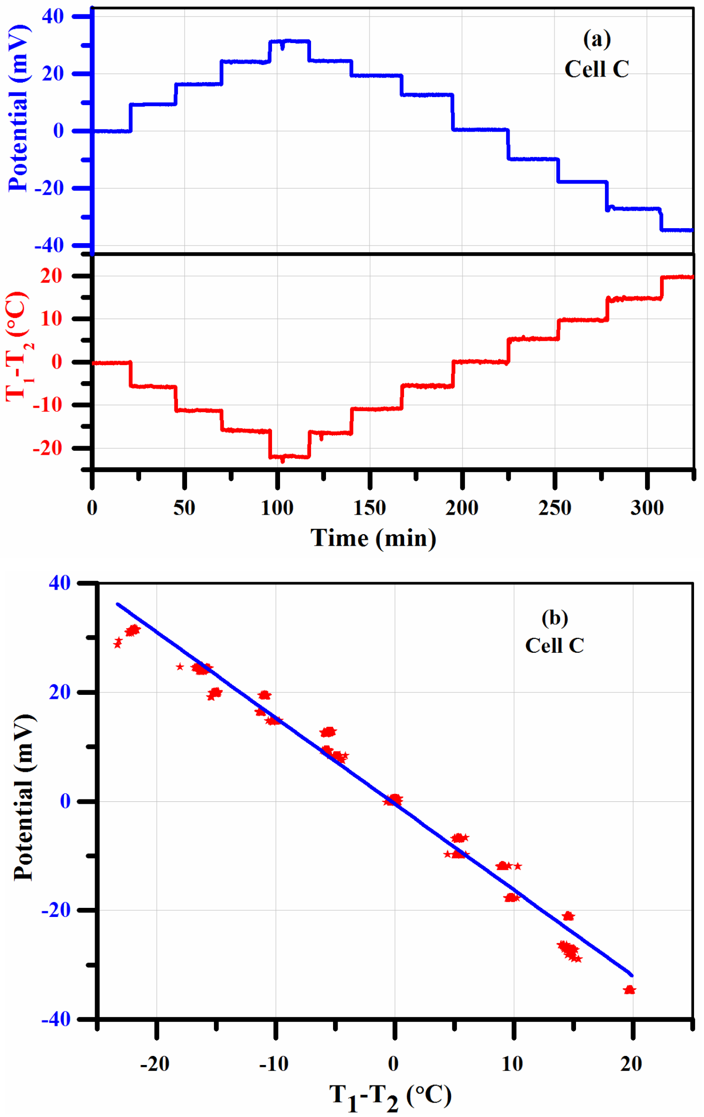

Figure 3.1.3 (a) The measured potential and temperature difference and, **(b)** Seebeck coefficient plot for cell C with electrode gas flow rate of 18.6 ml/min.

We have further found by inspecting the raw data, like the ones pictured in **Figure 3.1.3 a** and processes in **Figure 3.1.3 b**, that the thermoelectric potential measurement could be reversed by reversing the temperature difference, and that there was no bias potential between the gold electrodes at moderate flows of gas to the electrode. Gold was chosen to avoid interference of oxide layers, which are common on Pt. The straight line in **Figure 3.1.3 b** allows us to conclude that the potential measurement is sound (reversible, well defined); and that the standard deviation between 3 and 6% in **Table 3.1.2** and **Table 3.1.3** in the line reflects the accuracy of the experiment.

The Seebeck coefficient and the electrode gas flow rate:

The thermoelectric potentials, recorded for cells A-E at an average operating temperature of 550 °C, are presented in **Table 3.1.2**. All the potentials were plotted against the respective temperature difference, as in **Figure 3.1.3 b**, and the Seebeck coefficient was calculated from the slope of the linear fit. The Seebeck coefficient at a slow flow rate of electrode gas (16.1 ml/min) was similar to a previously reported value, ~ -1.2 mV/K, cf. **Table 3.1.2** [28, 63].

When we exclude the results for cell E in **Table 3.1.2**, reasons will be discussed later, the Seebeck coefficient of **Table 3.1.2** and **Figure 3.1.3** varied systematically from cell A (-1.1 mV/K) to cell D (-1.7 mV/K) with an increasing gas flow rate. Each result was stable for more than an hour, see **Figure 3.1.4**. **Figure 3.1.5** shows an experiment with constant temperature difference, held over 3 h. Some fluctuations in the temperature were observed. We attribute them to changes in bubble coverage at times when the gas flow rate was changed. A huge change in initial potential was, however, observed by increasing the gas flow stepwise from 0 to 70 ml/min. This is the origin of the varying Seebeck coefficient in **Table 3.1.2**.

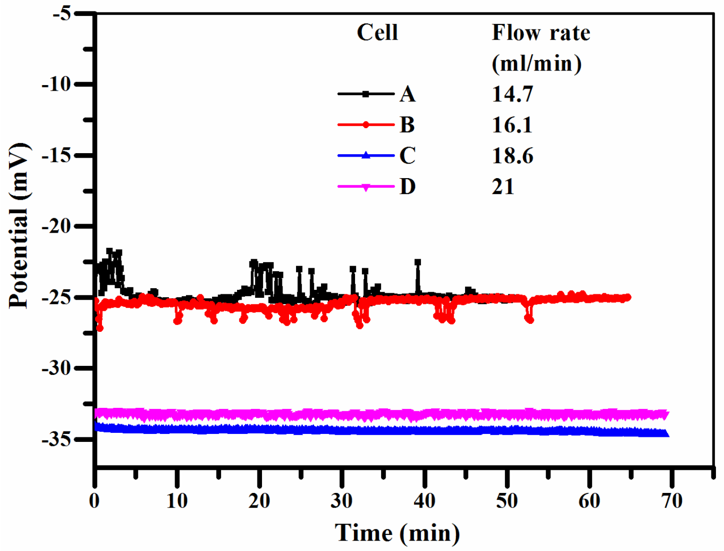

Figure 3.1.4 Measured potential versus time for electrode temperature difference of 20 °C with varying electrode gas flow rate (Cell A-D).

This systematic dependence of the potential on the gas flow rate is, however, difficult to understand, since we found no significant bias potential (see discussion above). Normally an increased flow gives a better stirring and elimination of concentration polarization or thermal polarization (Soret effects). However, in this situation, there is no concentration polarization to reduce. There is a zero-bias potential at zero temperature difference. The well-behaved thermoelectric potential measurements (**Figure 3.1.3**) indicate that the electrode gas seems to have achieved the temperature of the gold electrodes. Any lack of electric contact and ill-defined electrode reactions, cannot explain these results which seem to be reversible. Similar cells, with halide electrolyte and halogen electrodes, have shown similar behavior. Metz *et al.* [15], suggested that the Seebeck coefficient varied with gas flow rate because of lack of contact area at the electrode interface and depolarization effects. This may be so in the case of cell E which breaks down (see below), but not in cells A-D. At this moment, we have therefore no scientifically justified explanation for the effect.

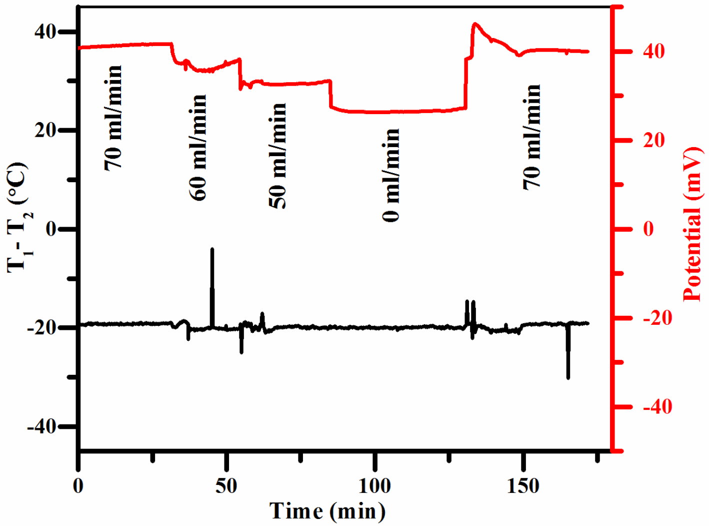

Figure 3.1.5 Potential measured with a thermocell, at constant electrode position with change in gas flow rates.

The three-phase contact area at the electrode-gas-electrolyte interface needs to be well equilibrated and mixed to give a reliable potential reading. It is, however, difficult if not impossible, to stir the molten electrolyte with 44.3 vol% of MgO dispersed. This fact could, however, lead to *flow-dependent systematic differences* between the two electrodes. A tentative explanation is then that *electrokinetic* effects arise. Such effects may add to the electric potential, for instance, if the gas pressure differs between the two sides. Gas flow over a heated sensing plate is known to give a difference in electric potential between the ends of the plate, meaning that the gas flow velocity can be found with high precision and quick response time from a Seebeck coefficient [82, 83]. More research is needed to investigate these variables.

Inhomogeneities of electrolyte mixture and lack of reversibility of electrodes:

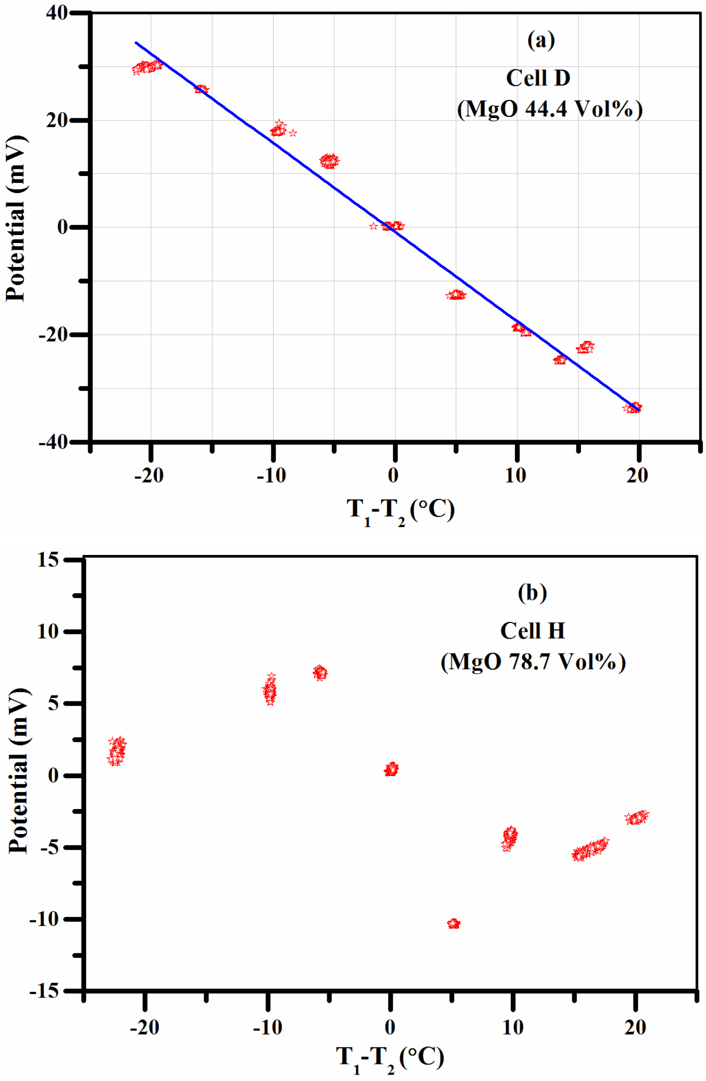

Figure 3.1.6 (a) Seebeck coefficient plot for cell D, and **(b)** Measured potential versus temperature difference in the cell H.

From **Figure 3.1.2 a-c** and **Figure 3.1.3 a, b** we concluded above that the system responded in a predictable way, for an initial time measurement (absence of Soret effects). The results from

Cell G (**Figure 3.1.2 d**) and **Table 3.1.3** confirmed that there is an optimal concentration of MgO(s) in the dispersion. The value should be < 66.1%. It is known from the literature (Jacobsen *et al.* [62]), and we have also confirmed this, that the system is more stable with than without the solid oxide dispersed [28]. The value 44.3% MgO was used in the original work by Jacobsen *et al.* [62]. The Seebeck coefficient with pure Li-carbonate was -0.88 mV/K, while with MgO(s) dispersed in the Li-carbonate it rose to -1.04 mV/K [28]. The presence of MgO has clearly an impact on the Seebeck coefficient.

In order to investigate this, further, we studied the effect of increasing the content of MgO. **Table 3.1.3** shows results for increasing content of MgO(s), from 44.3 to 66.1 % (cells D, F, G). The mixture is no longer homogeneous at the higher concentration (**Figure 3.1.2 d**). However, the Seebeck coefficient is unchanged (-1.7 mV/K). Going beyond the value of 66.1%, to 78.7%, has a detrimental effect. The electric potential is then no longer a linear function of the temperature difference. **Figure 3.1.6** shows how we move from a predictable (**Figure 3.1.6 a**) to an unpredictable cell behavior (**Figure 3.1.6 b**) by overloading the dispersion with MgO(s). We may speculate that an overload may obstruct the electrode reactions i.e. by preventing contact of components, leading again to ill-defined electrode reactions.

The high Seebeck coefficient (-1.7 mV/K) makes it interesting to pursue the track of adding solid state compounds. Shahi *et al.* [79] reported that the ionic conductivity increased with the addition of Al_2O_3 in molten AgI until 30 mole%, but decreased on further additions. An increase in thermoelectric power was also observed for Al_2O_3 dispersed in AgI, compared to pure AgI [79]. Clearly, this is a topic for further research.

3.1.5 Conclusions

The Seebeck coefficient of molten carbonate thermocells with suitable gas electrodes was measured at 550 ^oC, and with MgO(s) dispersed in a Li-Na eutectic mixture of carbonates. The Seebeck coefficient of -1.7 mV/K remains unchanged for different electrolyte mixtures with 44 to 66 vol% of MgO(s) dispersed in the eutectic carbonates. An optimal gas flow rate will help maintain electrolyte homogeneity, as evidenced by XRD and EDS studies, as well as good electrolyte/electrode contacts.

Acknowledgment

The authors wish to acknowledge the Research Council of Norway and industrial partners Hydro Aluminium, Boliden, Glencore, and Permascand for financial support in the research project “Sustainable and Energy Efficient Electrochemical Production and Refining of Metals (SUPREME)”.

3.2 Paper 2

Electrolyte Melt Compositions for Low Temperature Molten Carbonate Thermocells

Sathiyaraj Kandhasamy[†], Asbjørn Solheim[‡], Signe Kjelstrup[§], and Geir Martin Haarberg[†]

[†] *Department of Materials Science and Engineering, Norwegian University of Science and Technology (NTNU), 7491Trondheim, Norway*
[‡] *SINTEF Industry, SINTEF, 7491Trondheim, Norway*
[§] *PoreLab, Department of Chemistry, NTNU, 7491Trondheim, Norway*

Abstract

Industrial processes for the production of metals and alloys by metallurgical and electrochemical methods generate a great deal of waste heat due to irreversible losses. This waste heat may be used as a power source to generate electricity. A thermocell with noncritical and inexpensive molten carbonate based electrolyte mixtures with reversible ($CO_2|O_2$) gas electrodes was reported recently. It demonstrates the possibility of utilizing the waste heat (> 550 °C) as a power source. A thermocell is an electrochemical cell with two identical electrodes placed in an ionic conducting electrolyte solution with a temperature gradient between the electrodes. The heat source will be used to create the temperature gradient between the electrodes, which will lead to a potential difference by executing ionic diffusion in the electrolyte. In this work, the thermophysical and chemical properties of the electrolyte mixture were tuned by multicomponent mixing with molten (K and Ca) carbonate and LiF additives into the binary (Li,Na) carbonate mixture. It reduces the liquidus temperature to ~ 400 °C and enables the molten carbonate thermocells to recover the high-grade waste heat available at even low temperatures well below 550 °C. Still, the Seebeck coefficient of the thermocells remains large (in the range of -1.5 mV/K).

ACS Appl. Energy Mater., (2018). DOI: 10.1021/acsaem.8b00984

3.2.1 Introduction

Many industrial metal production processes require high-temperature operating conditions. Almost half of the heat is emitted as high grade (≥ 400 °C) waste heat into the environment by irreversible losses. The risk of global warming and possible scarcity of the non-renewable energy sources in the near future demands us to use the available waste heat as renewable energy source. Recently, thermocells using symmetrical gas (66 % CO_2 in O_2) electrodes and molten carbonate electrolyte mixtures demonstrated the chance of converting the high grade waste heat (550 - 850 °C) into power [28, 63, 68]. One candidate target is waste heat (~ 700 °C) recovery from the industrial silicon-producing furnaces operating at 1800 °C [63]. The electrodes with ($CO_2|O_2$) gas mixture offer reversibility and fast reactivity with the electrolyte carbonate ions. The change in entropy due to the gas-liquid phase transition of the electrode gas also contributes to the large Seebeck coefficient. The constant supply of the CO_3^{2-} anion source to the melt through the electrode gas mixture keeps the operation continuous. This thermocell shows a predicted increase in the Seebeck coefficient (more negative) with a decrease in the partial pressure of $CO_2|O_2$ in the electrode gas mixture [28]. This suggests an opportunity to also use the industrial off-gases containing CO_2 and O_2 in the mixture with other gases [28, 63].

The melting point of molten carbonate in the electrolyte mixture is the key factor to enable the conditions for thermoelectric conversion. It limits the thermocell operation to be above 550 °C with binary eutectic carbonates. This restricts accessing the waste heat (~ 450 °C) from the industrial aluminum production [84]. The production of aluminum is the second largest amount of metal produced worldwide, next to the iron and steel. At present the primary aluminum is produced by the Hall-Héroult electrolysis process [85] with molten cryolite containing the dissolved alumina (Al_2O_3) raw material as an electrolyte. The cells are operated at temperatures from 950 - 980 °C. Dissolved Al_2O_3 reacts with the consumable carbon anodes to produce aluminum metal along with CO_2 gas:

$$\frac{1}{2}\mathrm{Al_2O_3(dissolved)} + \frac{1}{2}\mathrm{C(s)} = \mathrm{Al(l)} + \frac{3}{4}\mathrm{CO_2(g)} \tag{3.2.1}$$

Nearly 50 % of the input energy is lost as waste heat to the surroundings [85]. As an integral part of the reaction process, the CO_2 gas emission is unavoidable but could be reduced [86, 87]. Empowering the molten carbonate thermocells to operate below 450 °C will permit the access to avail the dual sources of waste heat and CO_2-rich off-gases from the industrial aluminum production cells.

The lattice structure and ionic arrangement of the molten salts will change during the solid to liquid phase transition due to the dissociation of anion-cation pairs [88, 89]. The salt possesses a high electrical conductivity in the molten phase, which increases with the temperature [90]. On the other hand, thermal conductivity decreases with increasing temperature. It is thus easier to maintain a stable temperature gradient between the electrodes. The physical properties of the molten salts such as density, viscosity, surface tension, and liquidus temperature are easily tunable by multicomponent mixing [91-94]. Addition of new salts with less lattice energy [95] (**Table 3.2.1**) will lower the lattice chemical energy of the mixture and liquidus temperature (**Table 3.2.2**) [92].

Table 3.2.1 The melting point and lattice energy [95] of the molten salts in the electrolyte mixture.

Molten Salt	**Melting Point (°C)**	**Lattice energy (kJ/mol)**
Li_2CO_3	723	2523
Na_2CO_3	851	2301
K_2CO_3	891	2084
$CaCO_3$	825	2804
LiF	845	1030

In addition to the liquidus temperature, the decomposition temperature of the mixture will also be shifted. So, the possible stable temperature window of the electrolyte mixtures in the molten phase is determined by thermal analysis.

Table 3.2.2 The electrolyte molten melt composition dispersed in 55 vol % of solid MgO.

Electrolyte Mixture	**Melt Composition *MX***					**Melting Point without MgO from literature (°C)**
	Eutectic Carbonates (mol %)			**Addtivies (wt %)**		
	Li_2CO_3	**Na_2CO_3**	**K_2CO_3**	**$CaCO_3$**	**LiF**	
LNC	53	47	---	---	---	496
LNKC	43.5	31.5	25	---	---	397
LNKC-CC	43.5	31.5	25	14	---	376
LNKC-LF	43.5	31.5	25	---	14	368

In the present work we investigate the ternary eutectic $(Li,Na,K)_2CO_3$, with and without $CaCO_3$ and LiF additives, as an electrolyte mixture for reduced temperature operation (< 450 °C). The thermocell experiments are conducted with the same conditions as in our previous work, [68] except for difference in electrolyte composition and a wider range of operating temperatures.

3.2.2 Experimental

High purity (> 99%) carbonates of lithium, sodium, potassium, and calcium and lithium fluoride and magnesium oxide powders from Sigma-Aldrich were used in electrolyte mixture preparation as purchased. The composition specification of the electrolyte mixtures is listed in **Table 3.2.2**. The mixtures were prepared in a mortar by hand mixing and dried in a hot air oven for 48 h at 200 °C. Pure metal sheet and wire for making the electrodes (Au) and type S thermocouples (Pt-Pt/Rh10%) were purchased from K.A. Rasmussen, Norway. The necessary alumina components for thermocell (**Figure 3.2.1**) construction, such as 5-bore tubes (one center bore dia 2.3 mm and four other bores with dia 0.75 mm) and a tubular crucible (inner diameter of 38 mm with 200 mm length), were bought from MTC Haldenwanger, Germany. The electrodes were made of a gold sheet point-welded to the gold wire inserted into the alumina tubes center bore, and the thermocouples (Pt-Pt10%Rh) were inserted into two other holes of the tube. The thermocouple junctions were positioned close to the gold electrode to measure the accurate temperature at the electrode surface.

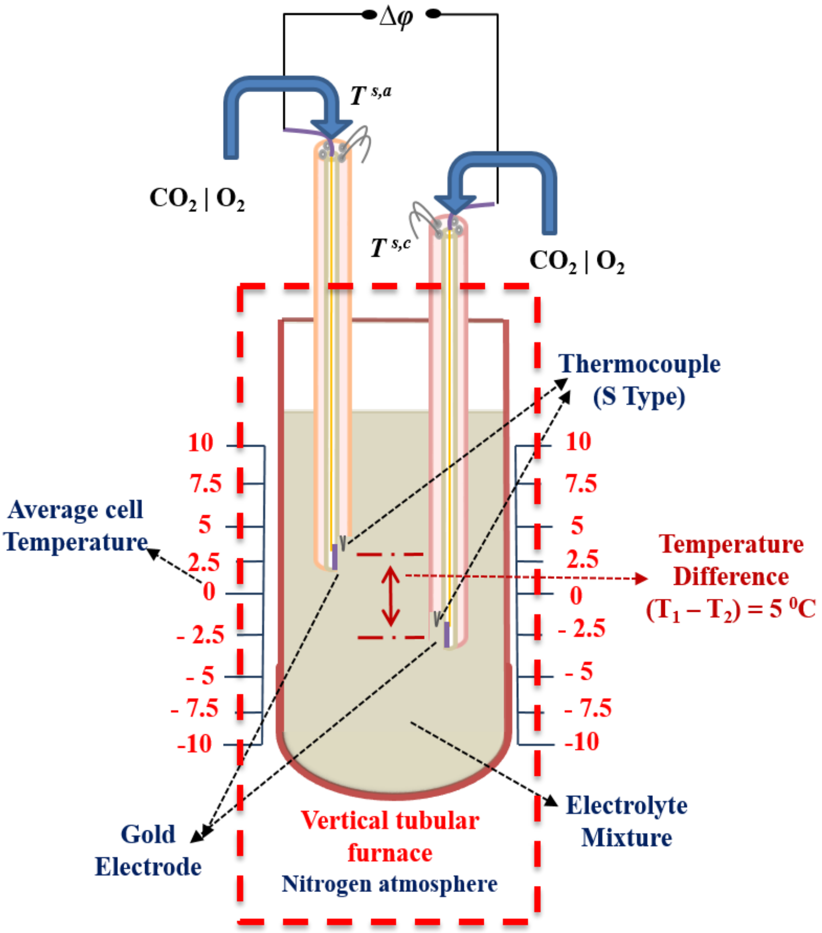
$\Delta\varphi$
$T^{s,a}$
CO_2 | O_2
$T^{s,c}$
CO_2 | O_2
Thermocouple
(S Type)
Average cell
Temperature
10
7.5
5
2.5
0
- 2.5
- 5
- 7.5
-10
10
7.5
5
2.5
0
- 2.5
- 5
- 7.5
-10
Temperature
Difference
$(T_1 - T_2) = 5\ ^0C$
Gold
Electrode
Vertical tubular
furnace
Nitrogen atmosphere
Electrolyte
Mixture

Figure 3.2.1 Cross-sectional schematic representation of the molten carbonate thermocell.

The electrodes are positioned to establish the temperature gradient of 5 °C, while the cell was maintained at the average cell temperature above the liquidus temperature.

The thermocell was assembled by placing the two alumina tubes (with the electrode and thermocouple) in the cylindrical crucible containing the electrolyte mixture. Then the cell was transferred (**Figure 3.2.1**) to a standard laboratory vertical cylindrical furnace under N_2 atmosphere. First, the electrolyte mixture was melted at the average cell temperature in the vertical tube furnace for at least 48 h to ensure homogeneous melt conditions. Premixed 34% oxygen in carbon dioxide gas mixture from AGA, Norway was supplied to electrode tubes at a flow rate of 21 mL/min. The gas mixture flow was controlled by a pair of Brooks instrument Sho-Rate flow meters with ± 5% accuracy. This molten carbonate electrolyte mixture thermocell can be represented as follows

$$\mathrm{Au}(T^{s,a})\ |\ \mathrm{CO_2,O_2(g)}\ |\ 45\mathrm{vol\%\ MX(l)},\ 55\mathrm{vol\%\ MgO(s)}\ |\ \mathrm{CO_2,O_2(g)}\ |\ \mathrm{Au}(T^{s,c})$$

where MX is the molten salt melt in the electrolyte mixture, listed in **Table 3.2.2**. The reversible ($CO_2|O_2$) gas electrode reaction in the carbonate electrolyte melt is

$$2\mathrm{CO_2(g)} + \mathrm{O_2(g)} + 4\mathrm{e^-} = 2\mathrm{CO_3^{2-}(l)} \qquad (3.2.2)$$

with the reverse reaction at the electrolyte interface of the other electrode.

The electrodes temperature and potential difference were continuously recorded by an Agilent, 34972A data acquisition unit. Positioning the electrodes at different heights in the electrolyte creates the temperature gradient (ΔT) between them by the difference in heating zones of the furnace. Meantime the average cell temperature was maintained to be constant. An equilibration time of 15-20 min from the positioning of the electrodes was used to make sure the measured potentials were stable. Then the cell potential was measured at least for 30 min at each temperature gradient.

The Seebeck coefficient of the thermocell with homogeneous binary electrolyte mixture LNC at the initial state (short time) is

$$\left(\frac{\Delta\varphi}{(T^{s,c}-T^{s,a})}\right) = \alpha_{S,0} = -\frac{1}{F}\left[\frac{1}{2}S_{CO_2} + \frac{1}{4}S_{O_2} + S_e^* - \frac{1}{2}S^*_{CO_3^{2-}} + \left(\frac{t_2}{x_2} - \frac{t_1}{x_1}\right)\frac{q^*}{T}\right] \qquad (3.2.3)$$

The Seebeck coefficient of the same LNC electrolyte mixture at steady Soret equilibrium state is:

$$\alpha_{S,\alpha} = -\frac{1}{F}\left[\frac{1}{2}S_{CO_2} + \frac{1}{4}S_{O_2} + S_e^* - \frac{1}{2}S^*_{CO_3^{2-}}\right] \qquad (3.2.4)$$

where S_j is the entropy of component j at an average temperature of the electrodes T and pressure p_j. The terms S_e^* and $S^*_{CO_3^{2-}}$ are the transported entropies of the electron and carbonate ion, respectively. This equation applies also to multicomponent mixtures.

The entropies and the transported entropies are generally functions of temperature. The gas entropies are expected to be larger than the transported entropies. These terms have then a negative contribution to the Seebeck coefficient. Then t_1 and t_2 are the transference coefficients and x_1 and x_2 are the mole fractions of Li_2CO_3 and Na_2CO_3. The ratio $\frac{q^*}{T}$ may be interpreted in terms of enthalpy changes across the layer, but it is difficult to interpret the sign of this last term. The last term in the initial state is not included at the Soret equilibrium state. A detailed theoretical derivation of the equations (3.2.3 and 3.2.4) based on nonequilibrium thermodynamics is explained in our previous work [28, 63]. The reported Seebeck coefficients in this paper are considered as to be at initial state, which means the measurement was made a short time after the establishment of the temperature gradient.

Table 3.2.3 Experimental algorithm used for the DSC/TGA thermal analysis.

Segment	Mode	Temperature Range (ºC)	Heating/Cooling Rate (ºC/min)	Hold Time (min)
1	Heating	50 - 300	20	---
2	Isothermal	300	---	10
3	Heating	300 - 530	10	---
4	Heating	530 - 900	20	---
5	Isothermal	900	---	10
6	Cooling	900 - 50	20	---

The chemical and phase stability was analyzed by determining the phase of the as-prepared and resolidified (i.e., before and after thermocell measurement) electrolyte mixture by X-ray diffraction (Bruker-D8 ADVANCE with a CuKα source of λ = 1.5406 Å). The thermal stability and liquidus/solidification temperature of the electrolyte mixtures were determined by TGA/DSC thermal analysis (NETZSCH STA449C Jupiter). Thermal analysis was performed by heating an alumina pan gently pressed with the powders of an as-prepared electrolyte mixture in reference to a similar empty alumina pan under N_2 atmosphere. Different segments of the temperature profile (**Table 3.2.3**) were used to improve the accuracy and minimize the analysis time.

3.2.3 Results and discussion

For comparison, the DSC was also performed for a pure single lithium carbonate mixture (LC) with 55 vol% solid MgO along with the proposed electrolyte mixtures in **Table 3.2.2**. **Figure 3.2.2** shows the change in thermal behavior of multicomponent mixtures from the pure single salt system. The LC mixture DSC heating curve (**Figure 3.2.2 a**) shows a sharp endothermic peak at 718 ºC representing the melting point of the mixture, which is slightly lower than for the pure Li_2CO_3 [96]. The presence of solid MgO could help in the early melting of the carbonates due to the decrease in enthalpy of fusion [93, 97]. It suggests that the presence of solid MgO stabilizes the Li_2CO_3 below its liquidus temperature. Then the carbonates begin to melt from the region near the solid MgO surface as an affected solid state in this heterophase mixture [80].

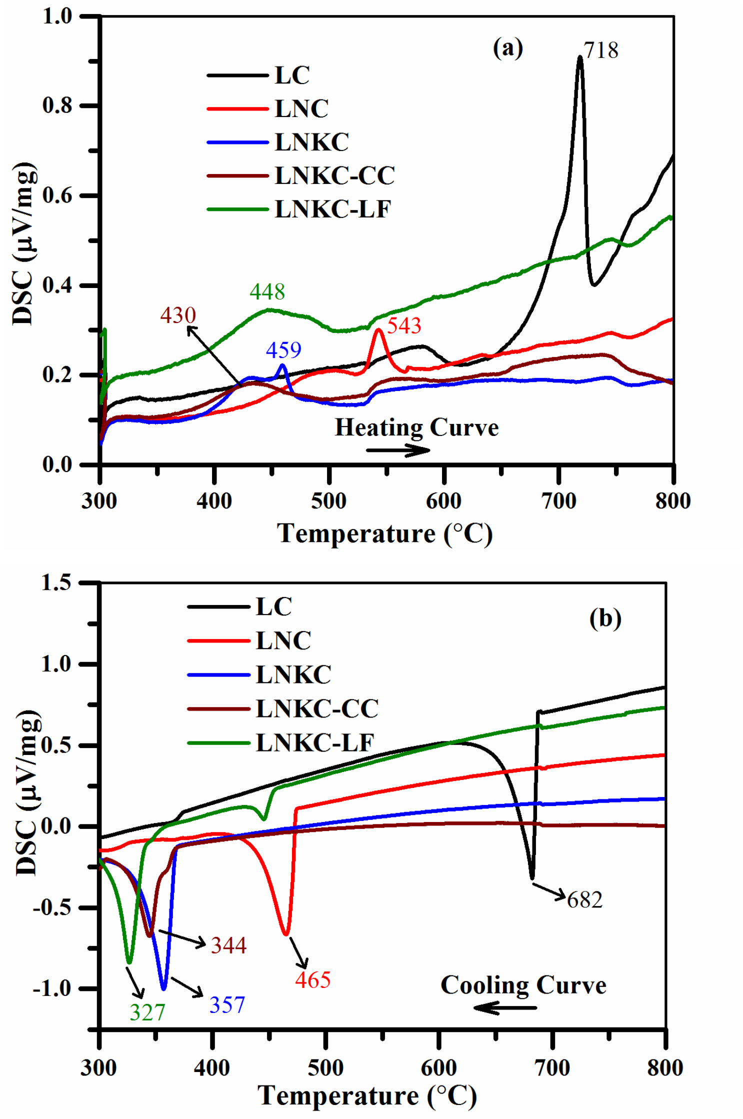

Figure 3.2.2 DSC analysis to show the change in **(a)** liquidus and **(b)** solidification temperatures of the electrolyte mixtures in **Table 3.2.2**.

In all other electrolyte mixtures, a broad endothermic peak covering a wide temperature range with less intensity is observed. The endothermic peak begins once the first liquid is formed, and due to the low thermal conductivity of the mixture, a wide range of temperature is required to melt the last fraction of carbonates in the mixture. Even two endothermic peaks are seen in the case of LNC and LNKC mixtures. The formation of a metastable solid state by solid-solid phase transformation may lead to an additional endothermic peak before melting [98]. After the solid-solid phase transition the absorption of heat leads to a rapid endothermic peak, which represents the liquidus temperature of the eutectic mixture. Also the inhomogeneity of the multicomponent mixture may lead to an additional endothermic peak. However, the peak maximum is higher than the expected liquidus temperature in **Table 3.2.2** (molten carbonates without MgO). The large thermal contact resistance between the solid sample and alumina pan container at this heating rate (10 ºC/min) affects the homogeneous temperature distribution in the sample and shifts the melting point [98]. Using a slow heating rate (below 5 ºC/min) may improve the data accuracy [91].

The improved thermal contact between the alumina pan and the sample after melting shows a sharp exothermic peak on resolidification in the DSC cooling curves (**Figure 3.2.2 b**). The change in the sharp peak position in the cooling curves confirms the reduction in liquidus temperature in multicomponent mixing, in the order of (LC > LNC > LNKC > LNKC-CC > LNKC-LF), this drift is identical to the literature [92, 99]. The steady baseline in the cooling curves displays the enhanced homogeneity [100] after melting. This makes it certain that the melting procedure with average cell temperature for 48 h in the tubular furnace before the thermocell measurement will improve the electrolyte melt homogeneity. The presence of the two well distinguishable separate exothermic peaks in the LNKC-LF cooling curve will be discussed later.

The recorded potentials after 20 min of equilibrium time from the establishment of each temperature gradient are shown as raw data in time scale (inset plot in **Figure 3.2.3 a**) for the LNKC thermocell. The negative temperature steps show a positive increase in potential which is reversed by reversing the temperature gradient between the electrodes. A negative potential is observed for the thermocell measurements with the hot electrode as a negative terminal. Then the potential changes to positive on reversing the hot and cold electrodes (the positive terminal becomes hot). A negligible bias potential is observed when both the electrodes are close to the average cell temperature (ΔT is ~ 0) [28, 63, 101].

The recorded raw data is plotted as potential against the temperature gradient (**Figure 3.2.3 a**), and the slope of the straight line determines the Seebeck coefficient. It displays a well-defined thermoelectric condition for the LNKC thermocell at 415 ºC. This behavior is identical to the reports with a binary or single carbonate electrolyte mixture at 550 ºC [28, 63, 68]. The thermocell Seebeck coefficients of all the electrolyte mixtures listed in **Table 3.2.2** are shown in **Figure 3.2.3 b**. A lower melting point of the ternary eutectic carbonate electrolyte mixtures makes the thermocell measurement possible at 415 ºC. However, the Seebeck coefficient is also measured at 550 ºC to make a comparative scale with the reported binary LNC electrolyte mixture in identical experimental conditions [68].

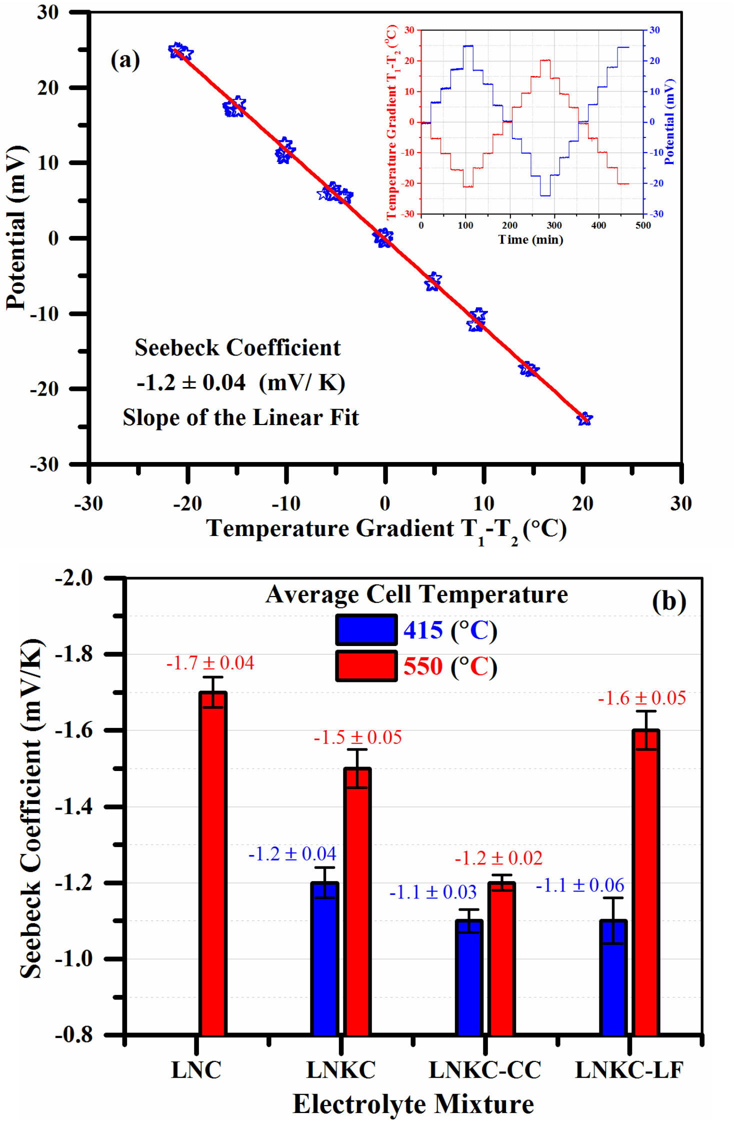

Figure 3.2.3 **(a)** Thermocell measurement with the LNKC electrolyte mixture at 415 °C and **(b)** the Seebeck coefficient of the thermocells different electrolyte mixtures in **Table 3.2.2**.

The ionic framework and transport behavior of the molten carbonates electrolyte mixture dispersed with solid MgO will be discussed before considering the changes in the Seebeck coefficient for different electrolyte mixtures. Mizuhata *et al.* [65, 80, 102] reported a lower electrical conductivity of similar molten carbonate electrolyte mixtures dispersed with different solid oxides, compared to pure molten carbonates. They also confirmed that the dispersed solid oxide behaves more as an insulator and that the electric conductivity of the mixture depended mostly on the ionic conductivity of the molten phase. The presence of dispersed solid oxide interface influences different transport properties. Nafe [64] supported this observation; the reduction in conductivity of a carbonate based composite electrolyte was due to anion-conduction rather than cation on dispersed solid oxides in carbonate melts.

In **Figure 3.2.4**, a scheme is proposed to illustrate the ionic environment of the binary molten carbonate electrolyte mixture (LNC) with solid MgO above the liquidus temperature. According to molten salt chemistry, the cation-anion pairs begin to dissociate at the liquid phase transition and increase the ionic degrees of freedom. However, in the liquid phase near the melting point a short-range lattice order remains as a memory effect of the solid lattice [2, 3]. Here the cation sits next to the respective anion or vice versa, such as in a quasi-crystal [89, 96]. Upon further increase in temperature, the ionic pair dissociation-distance increases and the concentration of ionic charge carriers increases with temperature [2, 3, 94, 103]. Reaching the complete dissociation of ion pairs at a higher temperature (boiling point), decomposition will be initiated [104].

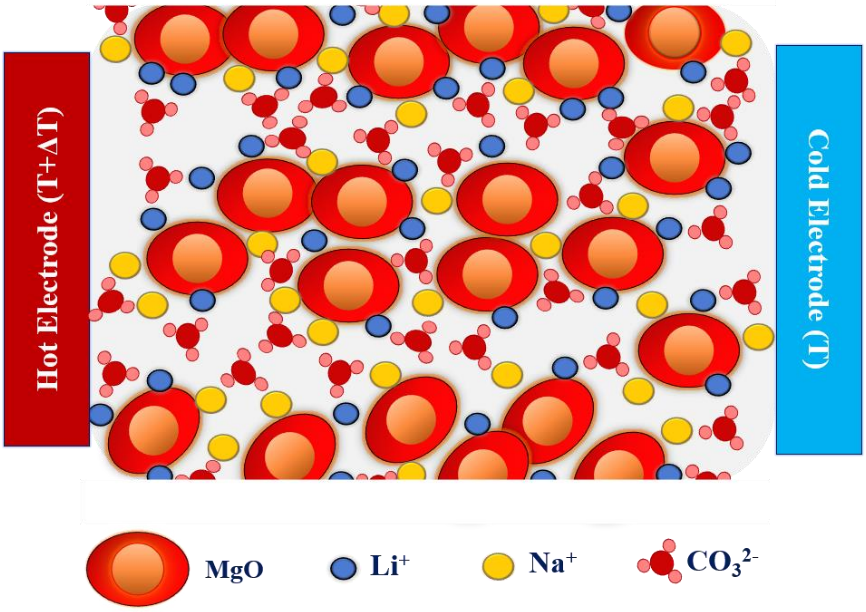

Figure 3.2.4 Schematic to illustrate the ionic arrangement in the LNC electrolyte mixture at initial conditions.

Identical melting behavior is expected in the molten carbonate electrolyte mixtures in thermocells. Ionic movement occurs in electrolyte melt due to thermal diffusion setup by the temperature gradient between the electrodes. In pure molten salts without solid oxide, the fast-moving small cations are the predominant charge carriers rather than the large anions. However the dispersion of solid oxides turns the larger anions into being the charge carriers due to the interface (solid MgO/M^+ cations) composite effect [64]. Thus, the randomly arranged solid MgO particles wrapped with a negative surface charge attract the small metal (Li, Na) cations and withhold its mobility, thus the anions become a dominant carrier. Also, the MgO interface effect on the carbonate melt will reduce the heat flux [105]. The theoretical expression for the Seebeck coefficient of these thermocells derived by irreversible thermodynamics depends on the transported entropy of the carbonate ions, rather than the metal ions, in agreement with the illustrated transport behavior [28, 63]. Also, in high-temperature molten carbonate fuel cells with solid oxide matrix and carbonate melt electrolyte, the negative carbonate ions are considered as a major charge carrier [99, 106].

In this thermocell, the large carbonate anions diffuse from the cold to the hot electrode in the electrolyte mixture. The ionic arrangement in the electrolyte mixture may influence the carbonate ions' degree of diffusion [64, 94]. Even though the cations are immobilized on the solid MgO surface, the addition of larger cations could alter the carbonate ion mobility. The change in anion-cation Coulombic force of attraction and polarization power on the change in cation size varies the activation energy for conduction and diffusion of the carbonate ions [28, 94]. The thermocell Seebeck coefficient, directly depends on the transported entropy carried along with the charge carrier (transported entropy is an energy from the lattice order-disorder transition).

Thus, the transported entropy of the carbonate ions is reduced while moving from the pure LC to the binary LNC electrolyte mixture due to the lattice defects by multicomponent mixing and will increase the Seebeck coefficient, but the substitution of sodium cation by large potassium in the binary melt, reduces the Seebeck coefficient [63]. Also, in the present study (**Figure 3.2.3 b**), the Seebeck coefficient (average cell temperature 550 °C) of the binary LNC thermocell reduces from -1.7 mV/K to -1.5 mV/K for the LNKC. The Seebeck coefficient reduces further to -1.2 mV/K for the electrolyte mixture LNKC-CC due to the strong lattice energy between the asymmetric divalent calcium (Ca^{2+}) cation and carbonate anion in the monovalent cations melt. The LNKC-LF mixture results show a slightly higher Seebeck coefficient than the ternary LNKC mixture, even though the concentration of carbonates is reduced by fluorides addition in the melt.

The illustrated ionic framework and the dependency of the Seebeck coefficient on cation composition in the electrolyte mixture, suggest that the preferred path for carbonate ion diffusion is associated with cations that are attracted to the solid MgO surface, rather than to the core of carbonate melt. Mizuhata *et al.* [80] reported an increase in electrical conductivity upon increasing the amount of solid oxide content, or its surface area in the carbonate melt, which makes the claim reasonable.

A high chemical and phase stability of the dispersed solid MgO in LNC electrolyte melt was reported [68]. The addition of other carbonates into the LNC mixture should retain the stability of the MgO phase [96, 97]. The stability of MgO in electrolyte (LNKC-LF) melt with LiF additive is studied by XRD (**Figure 3.2.5**). The sharp and intense diffraction peaks of MgO are at the same position before and after thermocell measurement, but the peaks related to carbonates and fluoride show reduced intensity for the resolidified electrolyte melt cooled from 550 °C [68]. Phases other than the phases due to the known melt composition are not observed. The lag in crystallinity on resolidification from the completely disordered melt phase reduces the diffraction peak intensity of the molten salts. Also, no evidence for recombination of the fluoride anions to the Na/K cations is seen, and the strong lattice force of small Li^+ is in favor of the LiF formation [107].

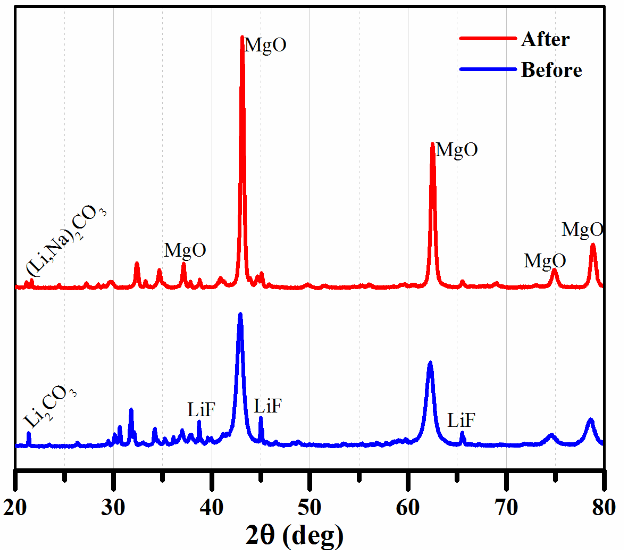

Figure 3.2.5 XRD phase analysis of the LNKC-LF electrolyte mixture, before and after the thermocell measurement at 550 °C.

Meanwhile, the Li^+ rich melt leads to a cation phase separation on resolidification showing a splitting in peak position corresponding to pure Li_2CO_3 with an additional peak for binary $(Li,Na)_2CO_3$ phase. Such splitting was not observed previously in an LNC electrolyte mixture [68, 107, 108]. In the LNKC-LF mixture DSC cooling curve, the occurrence of a small additional exothermic peak in the resolidification range of LNC supports this cation phase separation observed using XRD. However, it couldn't be an impurity phase, thus the multicomponent mixing just leads to a doping effect without any chemical side reaction [92]. The solid MgO phase remains stable throughout the thermocell operation even in the presence of LiF in the electrolyte.

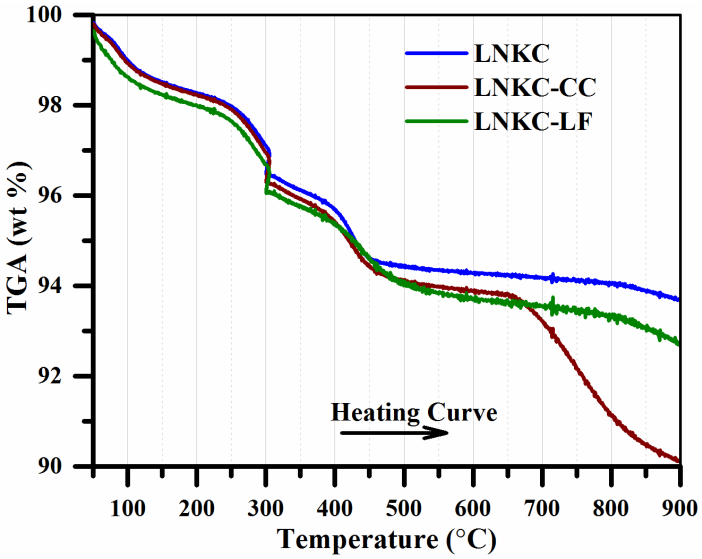

Figure 3.2.6 Thermochemical stablility of the different electrolyte mixtures by TGA analysis.

The decomposition temperature of the electrolytes beyond the melting point, where the dissociated CO_3^{2-} ions begin to escape as CO_2 and affect the melt homogeneity, [104] determines the stable liquid phase temperature upper window for the thermocell operation. So, the thermochemical stability of the electrolyte mixtures is analyzed by TGA along with the DSC measurements. In **Figure 3.2.6** the decomposition process is monitored by measuring the change in electrolyte weight on heating to 900 ºC under N_2 atmosphere. The weight loss observed before 200 ºC is due to the removal of moisture [91] and the sudden drop around 300 ºC is attributed to the implemented isothermal condition followed by the different heating rates used in the measurement algorithm (**Table 3.2.3**). The electrolyte mixtures solid to liquid phase transition shows the respective change in TGA curve around 400 ºC for the ternary carbonate mixtures (LNKC, LNKC-CC, LNKC-LF).

As mentioned in the DSC discussion the high interface thermal resistance between the solid sample and alumina pan in high heating rate can shift the corresponding liquid weight change in TGA to high/low temperatures [91]. The lattice energy and cation polarization power of the salt have strong effects on their thermal stability [109]. As shown in **Table 3.2.1**, the larger lattice energy of the $CaCO_3$ prompts the early decomposition in LNKC-CC [100, 107]. However, the presence of Na, K carbonates with low lattice and ionization energies establishes a short range of stable melt phase in LNKC-CC between the melting and decomposition temperatures [110]. The ternary eutectic carbonate electrolyte mixtures with and without LiF offer a chemical stability at higher temperatures along with the reduced liquidus temperature [92, 93].

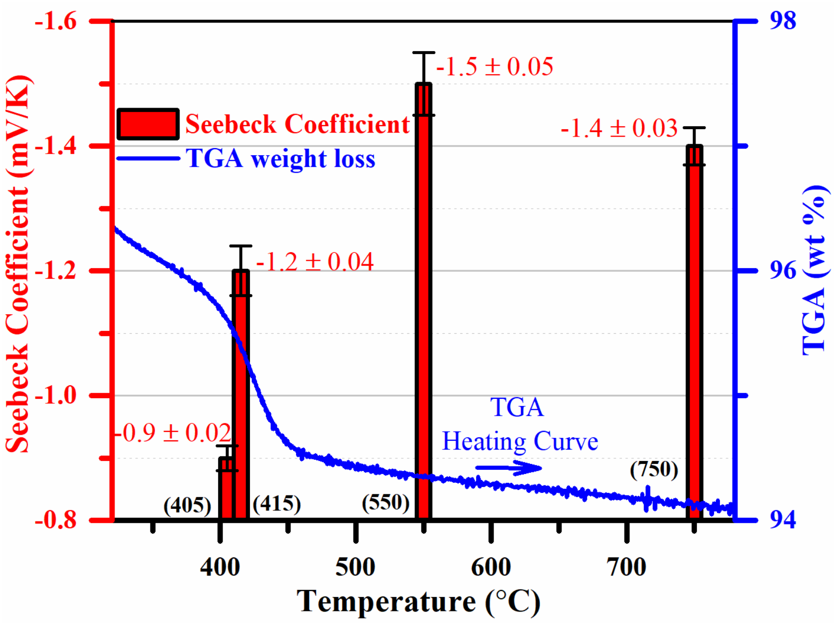

Figure 3.2.7 Seebeck coefficient of the LNKC thermocell at different average cell temperatures merged with the TGA weight loss profile.

The thermocell measurements with the LNKC ternary molten carbonate electrolyte mixture were performed in the determined stable temperature window (from 405 to 750 ºC). Along with the Seebeck coefficients, the TGA weight loss of the corresponding electrolyte mixture on increase in temperature is also merged in **Figure 3.2.7**. An increase in the carbonate ion degree of freedom by enhanced cation-anion pair dissociation by raising the thermocell temperature lowers the activation energy required for carbonate ion migration [64, 103]. Also, the transported entropy of carbonate ions reduces due to large lattice disorder by an increase in the average cell temperature. Thus, the Seebeck coefficient increases from -0.9 mV/K (405 °C) to -1.5 mV/K (550 °C).

The dependence of the Seebeck coefficient on the operating temperature is similar to the behavior reported previously (increase in the Seebeck coefficient with average cell temperature) [63]. Existence of short-range lattice order (quasi-crystalline nature) [108] in the melt phase near the liquidus temperature results in a drastic change in the Seebeck coefficient for a small rise (10 ºC) with the average cell temperature (405 to 415 ºC). The further increase in thermocell temperature to 750 ºC, slightly reduces the Seebeck coefficient to -1.2 mV/K. There is no significant decomposition weight loss observed during TGA measurement under N_2 atmosphere at this temperature; but during the thermocell measurements, the availability of O_2 electrode-gas along with CO_2 could initiate carbonate decomposition a bit earlier, around 730 ºC [93]. Then the dissociated CO_3^{2-} ions begin to escape as CO_2 and affect the homogeneity of the electrolyte mixture by a decrease in CO_3^{2-} ions concentration and reduced Seebeck coefficient at 750 °C.

However, the LNKC mixture enables thermocell operation at 405 ºC which is well below the desired reduced temperature (450 ºC). The electrolyte mixture with LiF will likely corrode the metal electrodes which demands an extensive study for higher temperature operation, [111] but the gold and platinum metals are stable in this regards. The morphology of the Au electrodes is not modified during the thermocell measurements. Also change in electrolyte composition has no impact on the surface morphology of the Au electrodes. The SEM images showing the surface morphology of the electrodes are provided in the supporting information (Chapter 3.2.5). Also, the addition of the low melting temperature salts like molten chlorides, nitrates, and hydroxides will liquidize the ternary carbonate mixture even sooner, but the complex ionic melt will affect the solid MgO phase and melt chemical stability [93, 107, 110].

3.2.4 Conclusions

A low liquidus temperature of the ternary eutectic LNKC electrolyte mixture can be achieved by multicomponent mixing with low lattice energy salts. This permits the operation of molten carbonate thermocell at a reduced temperature range (< 450 ºC). The high-temperature thermochemical stability of the mixture widens the operating temperature window of the thermocell. Addition of $CaCO_3$ and LiF into the ternary eutectic carbonates shifts the liquid phase-transition to even lower temperatures, but the higher lattice energy of $CaCO_3$ brings down the stable temperature window by early decomposition. While the LiF-addition demonstrates a better stability at high-temperatures, the corrosion effect of the electrodes and other cell components should be investigated before warranting the better performance. XRD analysis shows that the dispersed solid MgO remains stable in the LNKC-LF electrolyte mixture at 550 ºC. Thus, the stable and suitable reduced temperature is optimized for the molten carbonate thermocell operation to recover the waste heat (< 450 ºC) from primary aluminum production industries.

Acknowledgment

The authors wish to acknowledge the Research Council of Norway for financial support of the research project “Sustainable and Energy Efficient Electrochemical Production and Refining of Metals (SUPREME)” project no. 228296 and the industrial partners Hydro Aluminium, Boliden, Glencore, and Permascand for support. Kjelstrup is thanking the Research Council of Norway for is Center of Excellence Funding scheme for Porelab, project no. 262644.

3.2.5 Supporting information

Electrolyte Melt Compositions for Low Temperature Molten Carbonate Thermocells

Sathiyaraj Kandhasamy[†], Asbjørn Solheim[‡], Signe Kjelstrup[§], and Geir Martin Haarberg[†]

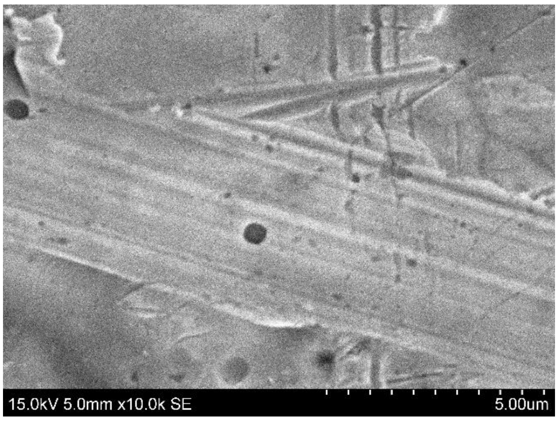

Figure 3.2.8 SEM surface morphology of the gold electrodes before thermocell measurements.

ACS Appl. Energy Mater., (2018). DOI: 10.1021/acsaem.8b00984

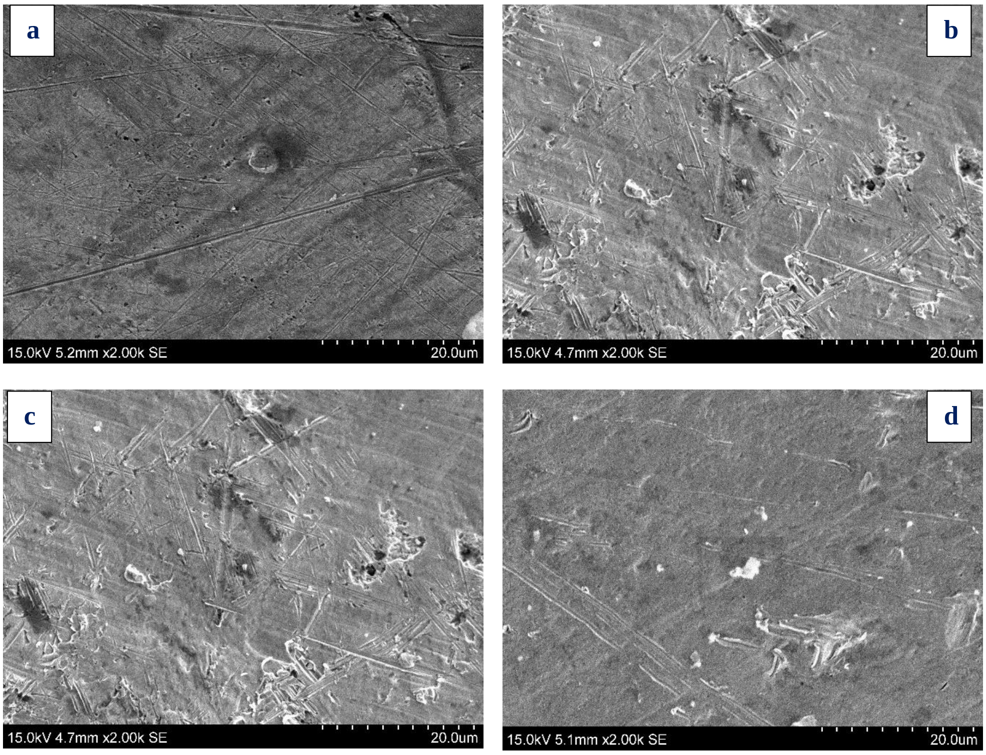
a
b
c
d
15.0kV 5.2mm x2.00k SE
20.0um
15.0kV 4.7mm x2.00k SE
20.0um
15.0kV 4.7mm x2.00k SE
20.0um
15.0kV 5.1mm x2.00k SE
20.0um

Figure 3.2.9 SEM surface morphology of the gold electrodes used in thermocells with different electrolyte mixtures at 550 °C.

(**a** - LNC, **b** - LNKC, **c** - LNKC-CC, **d** - LNKC-LF)

Papers 3, 4 and 5 are awaiting publication
and are not included in NTNU Open

Chapter 4 Suggestions for Future Work

In the latter part of this thesis the possibilities for configuring the molten carbonate thermocells as identical to the cathode side half-cell of the MCFC were examined. In this regard the suggestions for further work on the molten carbonate thermocell towards adopting the existing MCFC technology will be,

- The stability and lifetime of electrodes under thermocell operating conditions.
- Probabilities to alter the electrodes arrangement to establish the temperature gradient.
- Effective electrodes orientation and cell stacking to improve the power output (i.e. subsequent positioning of hot and cold electrodes).

In addition to a stand-alone power production system, a lot of opportunities are conceivable to combine this thermocell operation with the existing high temperature power production plants. Recently the feasibility of using the traditional molten carbonate fuel cells (MCFC) for carbon capture and storage (CCS) is explored. The MCFC power generation unit integrated with CCS operation has been found to increase the total efficiency of the plant. Similarly, the molten carbonate thermocell can be combined with MCFC and intermediate temperature solid oxide fuel cells (IT-SOFC) operating at a similar high temperature (> 500 °C) and with CO_2 rich gas. However, the possibilities to probe the potential difference arise due to the temperature gradient between two identical electrodes (i.e. cathode and cathode) of the fuel cells should be studied. This suggests that the real-time applications of these high temperature thermocells are not too far away.

Other than the thermocell, the reported simple heat flux DSC method to measure the thermal conductivity of the molten salt mixtures will be interesting for the applications using molten salts. For example, in solar power plants the molten salts are used as heat transfer fluid and heat storage medium, which is mainly dependent on the thermal properties of the molten salt. Finding a suitable measurement program for using the proposed modified DSC approach will make it possible to determine all the required thermal properties in a single thermal (DSC/TGA) measurement. Thermal properties of interest are liquidus temperature, thermal stability, specific heat capacity and thermal conductivity. Also, making the highly homogeneous alloys available with similar purity as the DSC metals standard could enable this approach to measure the thermal conductivity at any required temperature. If the liquidus temperature of the standard alloy/metal is matching the temperature of the application, the thermal conductivity of the molten mixture can be determined at the exact temperature.

Chapter 5 Conclusions

The thermocells demonstrated with molten carbonate electrolyte mixtures and ($CO_2|O_2$) gas electrodes possess the opportunity to generate electricity from high temperature waste heat. Optimizations reported in this thesis accomplishes the thermocell with enhanced Seebeck coefficients. The combination of electrolyte mixture (binary eutectic $(Li,Na)_2CO_3$ dispersed with 55 vol% MgO(s)) and the ($CO_2|O_2$) gas electrode (flow rate 21 ml/min) delivered the larger Seebeck coefficient (-1.7 mV/K) at 550 °C. Densification of the electrolyte mixture by randomly close packed solid MgO (55 vol%) particles with large surface area (123 m^2/g) limits the heat flux. It provided a steady temperature gradient between the electrodes. The optimal electrode gas flow rate (21 ml/min) established an equilibrated electrolyte-electrode interfacial contact to probe the potential difference.

Also, the influence of the physicochemical and thermochemical properties of the electrolyte mixture with solid oxide was explored to understand its impact on the thermocell behavior. The physicochemical properties show that the change in an acid-base property of the molten carbonate and solid oxide disturbs the electrolyte stability (structural transformation, chemical reactivity and homogeneity). Accordingly, the existence of MgO or CeO_2 achieves a higher stability of the electrolyte mixture than the Al_2O_3 or $LiAlO_2$, the corresponding change in thermocell Seebeck coefficients was also shown. So, the Seebeck coefficient of the electrolyte containing MgO at the Soret equilibrium state (-1.8 mV/K) remains essentially the same as at the initial time (-1.7 mV/K). The thermochemical property showed that the dense dispersion of MgO (with the large surface area) reduces the liquidus temperature of the molten carbonate along with the reduction in heat flux. Thus, in addition to a larger thermocell Seebeck coefficient this combination gives a reasonable figure of merit (ZT = 1.1), which is comparable to the semiconductor thermoelectric materials. Also, in term of the power output this combination was superior to the other type of thermocells with liquid electrolytes, but lower than the semiconductor thermoelectric due to high ohmic losses.

The ternary eutectic $(Li,Na,K)_2CO_3$ molten carbonate mixture with MgO lowers the liquidus temperature and enables the thermocell operation at reduced temperatures. The multi-cationic molten carbonate mixture enables the thermocell to recover the waste heat (< 450 °C) from primary aluminum production industries. Still, the thermocell Seebeck coefficient remains larger (-1.5 mV/K) even after substituting the larger K cation with smaller Li, Na ions in the electrolyte mixture. The feasibility of an inexpensive nickel based current collector to operate the thermocell was also demonstrated. Even the NiO phase exposes a high electrical resistivity the thermocell Seebeck coefficient still remains above -1.2 mV/K (more negative). Using the NiO current collectors could reduce the energy generation cost further in addition to the inexpensive molten carbonates electrolyte. Other than the thermocell measurements, simple, cost-effective and reliable approaches to acquire the electrical and thermal conductivity of the molten electrolyte at elevated temperature could add further novelty to this work. The conductivity cell with two capillary electrodes acquires the electrical conductivity with high precision due to the long current path. Then a simple heat flux DSC was used to measure the thermal conductivity of the molten samples with high accuracy.

Bibliography

[1] E. Bouty, Phénomènes Thermo-Électriques Et Électro-Thermiques au Contact D'un Métal et D'un Liquide, *Journal de Physique Théorique et Appliquée,* 9 (**1880**) 229-241.

[2] K. Cornwell, The Thermoelectric Potential of Molten Salt Thermocells, *Journal of Physics D: Applied Physics,* 5 (**1972**) 1199-1211.

[3] K. Cornwell, The Possibility of Using Molten Salts for Thermoelectric Generation, *Journal of Physics D: Applied Physics,* 1 (**1968**) 173-178.

[4] T.I. Quickenden, Y. Mua, A Review of Power-Generation in Aqueous Thermogalvanic Cells, *J Electrochem Soc,* 142 (**1995**) 3985-3994.

[5] A. Al-zubaidi, X.X. Ji, J. Yu, Thermal Charging of Supercapacitors: A Perspective, *Sustain Energ Fuels,* 1 (**2017**) 1457-1474.

[6] R. Haase, U. Pruser, J. Richter, Evaluation of Measurements on Thermocells Containing Molten-Salt Mixtures, *Ber Bunsen Phys Chem,* 81 (**1977**) 577-584.

[7] P. Mazur, Thermopotentials in Thermocells, *J Phys Chem-Us,* 58 (**1954**) 700-702.

[8] H.F. Hunger, Silver-Silver Iodide-Silver Thermocell, *J Electrochem Soc,* 120 (**1973**) 1157-1161.

[9] B.R. Sundheim, J. Rosenstreich, Molten Salt Thermocells, *The Journal of Physical Chemistry,* 63 (**1959**) 419-422.

[10] S. Senderoff, R.I. Bretz, Ionic Transport Entropy in Nonisothermal Molten Silver Chloride Cells, *J Electrochem Soc,* 109 (**1962**) 56-61.

[11] A. Gunawan, C.H. Lin, D.A. Buttry, V. Mujica, R.A. Taylor, R.S. Prasher, P.E. Phelan, Liquid Thermoelectrics: Review of Recent and Limited New Data of Thermogalvanic Cell Experiments, *Nanosc Microsc Therm,* 17 (**2013**) 304-323.

[12] T.J. Abraham, D.R. MacFarlane, R.H. Baughman, L.Y. Jin, N. Li, J.M. Pringle, Towards Ionic Liquid-Based Thermoelectrochemical Cells for the Harvesting of Thermal Energy, *Electrochim Acta,* 113 (**2013**) 87-93.

[13] M.F. Dupont, D.R. MacFarlane, J.M. Pringle, Thermo-Electrochemical Cells for Waste Heat Harvesting - Progress and Perspectives, *Chem Commun (Camb),* 53 (**2017**) 6288-6302.

[14] H. Holtan, On the Energetic Treatment of Non-Isothermal Processes - the Principle of Thermal Interaction, *J Chem Phys,* 19 (**1951**) 519-525.

[15] C.R. Metz, R.L. Seifert, Emf of Isothermal and Nonisothermal Formation Cells of Molten Silver Halides, *J Electrochem Soc,* 117 (**1970**) 49-56.

[16] K.S. Pitzer, Thermodynamics of Thermocells with Fused or Solid Electrolytes, *J Phys Chem-Us,* 65 (**1961**) 147-150.

[17] S. Senderoff, Thermocell Battery, *Google Patents*, **1966**.

[18] B.F. Markov, E.B. Kuzyakin, Thermogalvanic Cells with a Single Fused Salt, *Russian Chemical Reviews,* 41 (**1972**) 250-257.

[19] R. Zito, Thermogalvanic Energy Conversion, *Aiaa J,* 1 (**1963**) 2133-2138.

[20] C. Sinistri, E. Pezzati, Notizen: The Thermoelectric Power of the Molten System (Ag + K)Cl, *Zeitschrift für Naturforschung A,* 22 (**1967**) 590-591.

[21] E. Pezzati, Thermoelectric Properties in Silver Bromide-Alkali Bromide Fused Mixtures, *Zeitschrift für Naturforschung A,* 25 (**1970**) 898-900.

[22] E. Pezzati, A. Schiraldi, A. Magistris, Thermoelectric Power of the Molten Systems (Ag + Me)I and (Cu + Me) I (Me = Na, K, Rb, Cs), *Zeitschrift für Naturforschung A,* 28 (**1973**) 1334-1337.

[23] A. Kvist, A. Randsalu, Thermoelectric Power of Molten and Solid Silver Sulphate, *Zeitschrift für Naturforschung A,* 21 (**1966**) 278-281.

[24] A.R. Nichols, C.T. Langford, Entropy of the Moving Cuprous Ion in Molten Cuprous Chloride from Thermogalvanic Potentials, *J Electrochem Soc,* 107 (**1960**) 842-847.

[25] E. Pezzati, A. Magistris, A. Schiraldi, Thermoelectric Power of the Molten Systems (Cu, Me)Cl and (Cu,Me)Br (Me = Na, K, Rb, Cs), *Zeitschrift für Naturforschung A,* 30 (**1975**) 388-390.

[26] W. Fischer, Die Thermokraft Einiger Zellen Des Typs Cl_2/T Geschmolzenes Clorid/T+Deltat Cl_2, *Z Naturforsch Pt A,* A 21 (**1966**) 281-286.

[27] J. Greenberg, L.H. Thaller, D.E. Weber, Thermopotential Measurements for Molten Cadmium Chloride, Cadmium Bromide, and Lead Chloride, *J Phys Chem-Us,* 67 (**1963**) 2488-2491.

[28] M.T. Børset, X. Kang, O.S. Burheim, G.M. Haarberg, Q. Xu, S. Kjelstrup, Seebeck Coefficients of Cells with Lithium Carbonate and Gas Electrodes, *Electrochim Acta,* 182 (**2015**) 699-706.

[29] C. Sinistri, The Thermoelectric Power in Molten and Solid Silver Nitrate, *Zeitschrift für Naturforschung A,* 20 (**1965**) 1045-1047.

[30] V. Backlund, J. Dupuy, Gustafss.S, A. Lunden, Thermal Diffusion in Molten Binary Mixtures of Silver Nitrate with Alkali Nitrates, *Z Naturforsch Pt A,* A 22 (**1967**) 471-476.

[31] R. Blachnik, H.A. Dreisbach, The Phase Diagrams of Ag_2X-AgY (X = S, Se, Te; Y = Cl, Br, I): Mixtures and the Structure of Ag_5Te_2Cl, *Journal of Solid State Chemistry,* 60 (**1985**) 115-122.

[32] R. Blachnik, G. Kudermann, Silberhalogenid-Silberchalkogenidsysteme / Silverhalide-Silverchalkogenidesystems, *Zeitschrift für Naturforschung B,* 28 (**1973**) 1-4.

[33] W. Fuchs, J. Richter, Soret Coefficients and Transported Entropies of Non-Isothermal Liquid Alkali Nitrate + Silver-Nitrate Mixtures, *Ber Bunsen Phys Chem,* 86 (**1982**) 46-51.

[34] J. Richter, A. Heller, W. Vreuls, Investigations of Nonisothermal Molten-Salts - Initial Values of Thermoelectric-Power for Systems $AgNo_3$, $LiNO_3$ + $AgNO_3$, and $NaNO_3$ + $AgNO_3$ as a Function of Temperature and Composition, *Ber Bunsen Phys Chem,* 81 (**1977**) 374-380.

[35] J. Richter, U. Prüser, Untersuchungen des stationären Zustandes der Thermodiffusion in Thermoketten mit Nitratschmelzen, *Berichte der Bunsengesellschaft für physikalische Chemie,* 81 (**1977**) 508-514.

[36] C. Sinistri, E. Pezzati, Thermoelectric Properties in Silver Chloride-Alkali Chloride Fused Mixtures, *Z Naturforsch Pt A,* A 25 (**1970**) 893-897.

[37] C. Sinistri, The Thermoelectric Power of the Molten Systems $(Ag+Li)NO_3$, $(Ag+Na)NO_3$, and $(Ag+K)NO_3$, *Zeitschrift für Naturforschung A,* 21 (**1966**) 753-755.

[38] A. Kvist, Transport Properties of Solid and Molten sulphates, *Universitetet*, **1967**.

[39] A. Schiraldi, E. Pezzati, Thermoelectric Power of the Molten Systems $PbCl_2$ - MeCl (Me = Li, Na, K, Rb, Cs), *Zeitschrift für Naturforschung A,* 32 (**1977**) 624-626.

[40] K. Wallin, A. Lunden, Notizen: The Thermoelectric Power of the Molten System Silver Nitrate - Lithium Nitrate, *Zeitschrift für Naturforschung A,* 22 (**1967**) 591-592.

[41] Y. Ito, S. Horikawa, J. Oishi, Y. Ogata, Concentration-Dependence of Thermoelectric-Power in a Molten-Salt System, *Electrochim Acta,* 30 (**1985**) 799-804.

[42] T. Murakami, T. Nishikiori, T. Nohira, Y. Ito, Thermoelectric power of M-H systems in molten salts and application to M-H thermogalvanic cell, *J Electrochem Soc,* 150 (**2003**) A928-A932.

[43] K. Ishida, S. Ohno, T. Okada, Electrical Properties of Molten AgCl–AgI Mixtures, *Journal of Non-Crystalline Solids,* 250-252 (**1999**) 488-491.

[44] J. Keuning, J.A.A. Ketelaar, Thermoelectric Coefficients of Silver-Molten Silver-Halide and Silver-Nitrate Mixtures, *P K Ned Akad B Phys,* 84 (**1981**) 269-286.

[45] K. Ichikawa, M. Shimoji, Thermoelectric Power of Molten Salt — Metal Solutions II. Bi + BiI_3 and Bi + $BiCl_3$ solutions, *Berichte der Bunsengesellschaft für physikalische Chemie,* 73 (**1969**) 302-306.

[46] K. Ichikawa, M. Shimoji, Thermoelectric Power of Molten Salt - Metal Solutions, I, Bi + $BiBr_3$ Solutions, *Berichte der Bunsengesellschaft für physikalische Chemie,* 71 (**1967**) 1149-1155.

[47] G.M. Haarberg, J. Thonstad, Electrochemical Properties of Metal-Molten Salt Mixtures, *J Appl Electrochem,* 19 (**1989**) 789-801.

[48] M. Cassir, A. Ringuedé, V. Lair, Molten Carbonates from Fuel Cells to New Energy Devices, in: H. Groult (Ed.) Molten Salts Chemistry, *Elsevier*, Oxford, **2013**, pp. 355-371.

[49] S. Ohno, K. Ishida, M. Togashi, A.C. Barnes, J.E. Enderby, The Electrical Properties of Molten $AgX-Ag_2Se$ (X = Br, I) Mixtures, *Journal of Physics: Condensed Matter,* 12 (**2000**) 1297-1314.

[50] S. Ohno, M. Togashi, A.C. Barnes, J.E. Enderby, Electrical Properties of Liquid Ag_2Se Containing Silver Halides, *Molten Salts Forum,* 5-6 (**1998**) 291-294.

[51] K. Ishida, S. Ohno, T. Okada, Electrical Properties of Liquid NiTe Alloys with Ni Halides, *Journal of Non-Crystalline Solids,* 312-14 (**2002**) 396-399.

[52] S. Ohno, A.C. Barnes, J.E. Enderby, The Electrical and Magnetic Properties of Molten AgCl-Ag_2S Mixtures, *J Phys-Condens Mat,* 8 (**1996**) 3785-3794.

[53] S. Ohno, K. Ishida, S. Tahara, T. Okada, Electrical Properties of Molten CuCl-Cu_2Se Mixtures, in: T. Scopigno, S. DePanfilis, A. DiCicco (Eds.) Lam14 - Xiv Liquid and Amorphous Metals Conference, **2011**, pp. 01003-01001-01006.

[54] S. Ohno, K. Ishida, M. Togashi, T. Okada, Electrical Properties of Molten AgI-Ag_2S Mixtures, *J Phys Soc Jpn,* 69 (**2000**) 1443-1448.

[55] S. Ohno, S. Tahara, T. Okada, Electrical Properties of Molten CuCl-Cu_2Te Mixtures, *J Phys Soc Jpn,* 79 (**2010**) 114702-114701-114705.

[56] S. Ohno, M. Togashi, A.C. Barnes, J.E. Enderby, Electrical Properties of Molten AgCl-Ag_2Te Mixtures, *J Phys Soc Jpn,* 68 (**1999**) 2338-2343.

[57] J.E. Enderby, A.C. Barnes, Liquid Semiconductors, *Reports on Progress in Physics,* 53 (**1990**) 85-179.

[58] J.E. Enderby, Molten Salts and Liquid Semiconductors: Structure and Electrical Properties, in: J.V. Acrivos, N.F. Mott, A.D. Yoffe (Eds.) Physics and Chemistry of Electrons and Ions in Condensed Matter, *Springer Netherlands*, Dordrecht, **1984**, pp. 231-253.

[59] A. Schiraldi, E. Pezzati, Thermoelectric Power of the Systems AgI-Ag_2XO_4 (X=Mo,W), *Zeitschrift für Naturforschung A,* 31 (**1976**) 1077-1080.

[60] K. Shahi, J.B. Wagner, Ionic-Conductivity and Thermoelectric-Power of Pure and Alumina-Dispersed AgI, *J Electrochem Soc,* 126 (**1979**) C319-C319.

[61] A. Schiraldi, E. Pezzati, P. Baldini, Thermoelectric-Power of the High Ionic-Conductivity Glasses AgI-$Ag_2O.B_2O_3$, *J Phys Chem,* 89 (**1985**) 1528-1531.

[62] T. Jacobsen, G.H.J. Broers, Single Electrode Heat Effects .1. Peltier Entropies of Gas Electrodes in Carbonate Paste Electrolytes, *J Electrochem Soc,* 124 (**1977**) 207-210.

[63] X. Kang, M.T. Borset, O.S. Burheim, G.M. Haarberg, Q. Xu, S. Kjelstrup, Seebeck Coefficients of Cells with Molten Carbonates Relevant for the Metallurgical Industry, *Electrochim Acta,* 182 (**2015**) 342-350.

[64] H. Nafe, Conductivity of Alkali Carbonates, Carbonate-Based Composite Electrolytes and IT-SOFC, *ECS J Solid State Sci Technol,* 3 (**2014**) N7-N14.

[65] M. Mizuhata, T. Ohashi, A.B. Beleke, Electrical Conductivity of the Coexisting System Containing Molten Carbonates and Rare-earth Oxide, in: D.M. Fox, M. Mizuhata, H.C. DeLong, R.A. Mantz, P.C. Trulove (Eds.) Molten Salts and Ionic Liquids 17, **2010**, pp. 439-447.

[66] E. Flem Belinda, Q. Xu, S. Kjelstrup, Å. Sterten, Thermoelectric Powers of Cells With NaF-AlF_3-Al_2O_3 Melts, Journal of Non-Equilibrium Thermodynamics, **2001**, pp. 125-151.

[67] A. Schiraldi, E. Pezzati, Thermoelectric Power of the Molten Systems (Cu, Ag) X (X=Cl, Br, I), *Zeitschrift für Naturforschung A,* 33 (**1978**) 42-44.

[68] S. Kandhasamy, L. Calandrino, O.S. Burheim, A. Solheim, S. Kjelstrup, G.M. Haarberg, Influence of Electrode Gas Flow Rate and Solid Oxide Ratio in Electrolyte on the Seebeck Coefficient of Molten Carbonate Thermocell, *J Electrochem Soc,* 164 (**2017**) H5271-H5276.

[69] U. Trolle, A. Kvist, The Thermoelectric Power of the Molten Chlorides, Bromides and Iodides of Lead, Tin and Zinc with Reversible Molten Metal Electrodes, *Zeitschrift für Naturforschung A,* 24 (**1969**) 469-470.

[70] V. Blinov, S. Kjelstrup, D. Bedeaux, V. Sharivker, The Role of the Transported Entropy of Lead Ions in Partially Thermostated and Adiabatic Cells, *J Electrochem Soc,* 148 (**2001**) E364-E371.

[71] H.P. Meissner, D.C. White, G.D. Uhlrich, Thermocells; Effect of Pressure on Voltage, *Advanced Energy Conversion,* 5 (**1965**) 205-216.

[72] H.S. Kim, W. Liu, G. Chen, C.W. Chu, Z. Ren, Relationship Between Thermoelectric Figure of Merit and Energy Conversion Efficiency, *Proc Natl Acad Sci U S A,* 112 (**2015**) 8205-8210.

[73] B. Sundheim, in Thermoelectric Materials and Devices, I. B. Cadoff, E. Miller, Eds. (Reinhold, New York, **1960**), pp. 194–198.

[74] M. Hamid Elsheikh, D.A. Shnawah, M.F.M. Sabri, S.B.M. Said, M. Haji Hassan, M.B. Ali Bashir, M. Mohamad, A Review on Thermoelectric Renewable Energy: Principle Parameters that Affect their Performance, *Renewable and Sustainable Energy Reviews,* 30 (**2014**) 337-355.

[75] B. Burrows, Discharge Behavior of Redox Thermogalvanic Cells, *J Electrochem Soc,* 123 (**1976**) 154-159.

[76] Y. Ito, T. Nohira, Non-Conventional Electrolytes for Electrochemical Applications, *Electrochim Acta,* 45 (**2000**) 2611-2622.

[77] Y.V. Kuzminskii, V.A. Zasukha, G.Y. Kuzminskaya, Thermoelectric Effects in Electrochemical Systems - Nonconventional Thermogalvanic Cells, *J Power Sources,* 52 (**1994**) 231-242.

[78] J.L. Weininger, Thermogalvanic Cells with Silver Iodide as a Solid Electrolyte, *J Electrochem Soc,* 111 (**1964**) 769-774.

[79] K. Shahi, J.B. Wagner, Ionic-Conductivity and Thermoelectric-Power of Pure and Al_2O_3-Dispersed Agl, *J Electrochem Soc,* 128 (**1981**) 6-13.

[80] M. Mizuhata, Y. Harada, G.J. Cha, A.B. Beleke, S. Deki, Physicochemical Properties of Molten Alkali Metal Carbonates Coexisting with Inorganic Powder, *J Electrochem Soc,* 151 (**2004**) E179-E185.

[81] D.L. Roest, P. Ballone, D. Bedeaux, S. Kjelstrup, Molecular Dynamics Simulations of Metal/Molten Alkali Carbonate Interfaces, *J Phys Chem C,* 121 (**2017**) 17827-17847.

[82] D. Li, Encyclopedia of Microfluidics and Nanofluidics, *Springer US,* **2008**.

[83] A.K. Sood, S. Ghosh, Direct Generation of a Voltage and Current by Gas Flow Over Carbon Nanotubes and Semiconductors, *Phys Rev Lett,* 93 (**2004**) 086601-086601-086604.

[84] C. Nowicki, L. Gosselin, An Overview of Opportunities for Waste Heat Recovery and Thermal Integration in the Primary Aluminum Industry, *Jom-Us,* 64 (**2012**) 990-996.

[85] P. Fellner, G.M. Haarberg, J. Hives, H. Kvande, A. Sterten, J. Thonstad, Aluminium Electrolysis: Fundamentals of the Hall-Héroult Process, *Beuth Verlag GmbH*, **2011**.

[86] B. Welch, M. Iffert, M. Skyllas-Kazacos, Applying Fundamental Data to Reduce the Carbon Dioxide Footprint of Aluminum Smelters, *Jom-Us,* 60 (**2008**) 17-24.

[87] A. Agnihotri, S. Rai, N. Warhadpande, Carbon Dioxide Management—Aluminium Industry Perspective, in: M. Goel, M. Sudhakar (Eds.) Carbon Utilization, *Springer Singapore*, Singapore, **2017**, pp. 217-229.

[88] S. Okazaki, M. Matsumoto, I. Okada, Study of Rotational and Vibrational Relaxation of the CO$_2^-$ ^{3}ion in Molten Alkali Carbonates by Raman Spectroscopy, *Molecular Physics,* 79 (**1993**) 611-621.

[89] G.J. Janz, F. Saegusa, Molten Carbonates as Electrolytes - Viscosity and Transport Properties, *J Electrochem Soc,* 110 (**1963**) 452-456.

[90] T. Kojima, Y. Miyazaki, K. Nomura, K. Tanimoto, Electrical Conductivity of Molten Li_2CO_3-X_2CO_3 (X : Na, K, Rb, and Cs) and Na_2CO_3-Z_2CO_3 (Z : K, Rb, and Cs), *J. Electrochem. Soc.,* 154 (**2007**) F222-F230.

[91] M.J. Glenn, J.A. Allen, S.W. Donne, Thermal Investigation of a Doped Alkali-Metal Carbonate Ternary Eutectic for Direct Carbon Fuel Cell Applications, *Energ Fuel,* 29 (**2015**) 5423-5433.

[92] Z.L. Zhang, Y.P. Yuan, N. Zhang, Q.R. Sun, X.L. Cao, L.L. Sun, Thermal Properties Enforcement of Carbonate Ternary via Lithium Fluoride: A Heat Transfer Fluid for Concentrating Solar Power Systems, *Renew Energ,* 111 (**2017**) 523-531.

[93] R.I. Olivares, C. Chen, S. Wright, The Thermal Stability of Molten Lithium–Sodium–Potassium Carbonate and the Influence of Additives on the Melting Point, *Journal of Solar Energy Engineering,* 134 (**2012**) 041002-041001-041008.

[94] T. Kojima, Y. Miyazaki, K. Nomura, K. Tanimoto, Physical Properties of Molten Li_2CO_3-Na_2CO_3 (52:48 mol%) and Li_2CO_3-K_2CO_3 (62:38 mol%) Containing Additives, *J. Electrochem. Soc.,* 160 (**2013**) H733-H741.

[95] D.R. Lide, CRC Handbook of Chemistry and Physics, 88th Edition, *Taylor & Francis*, **2007**.

[96] G.J. Janz, Molten Carbonate Electrolytes as Acid-Base Solvent Systems, *J Chem Educ,* 44 (**1967**) 581-590.

[97] S. Frangini, S. Scaccia, Thermal Stability and Oxidizing Properties of Mixed Alkaline Earth-Alkali Molten Carbonates: A Focus on the Lithium-Sodium Carbonate Eutectic System with Magnesium Additions, *Thermochim Acta,* 574 (**2013**) 55-62.

[98] T. Wang, D. Mantha, R.G. Reddy, Novel High Thermal Stability LiF–Na_2CO_3–K_2CO_3 Eutectic Ternary System for Thermal Energy Storage Applications, *Solar Energy Materials and Solar Cells,* 140 (**2015**) 366-375.

[99] S. Frangini, A. Masi, Molten Carbonates for Advanced and Sustainable Energy Applications: Part I. Revisiting Molten Carbonate Properties from a Sustainable Viewpoint, *Int J Hydrogen Energ,* 41 (**2016**) 18739-18746.

[100] S. Frangini, S. Scaccia, Influence of Lanthanum Carbonate Additions on Thermal Stability of Eutectic Lithium–Sodium Carbonate Near its Melting Point, *Thermochim Acta,* 551 (**2013**) 33-39.

[101] M. Bonetti, S. Nakamae, M. Roger, P. Guenoun, Huge Seebeck Coefficients in Nonaqueous Electrolytes, *J Chem Phys,* 134 (**2011**) 114513-114511-114518.

[102] M. Mizuhata, T. Ohashi, A.B. Beleke, Electrical Conductivity and Related Properties of Molten Carbonates Coexisting with Ceria-Based Oxide Powder for Hybrid Electrolyte, *Int J Hydrogen Energ,* 37 (**2012**) 19407-19416.

[103] C. Yang, R. Takagi, K. Kawamura, I. Okada, Internal Cation Mobilities in the Molten Binary System Li_2CO_3-K_2CO_3, *Electrochim Acta,* 32 (**1987**) 1607-1611.

[104] G.J. Janz, M.R. Lorenz, Molten Carbonate Electrolytes - Physical Properties, Structure, and Mechanism of Electrical Conductance, *J Electrochem Soc,* 108 (**1961**) 1052-1058.

[105] N. Gokon, D. Nakano, S. Inuta, T. Kodama, High-Temperature Carbonate/MgO Composite Materials as Thermal Storage Media for Double-Walled Solar Reformer Tubes, *Sol Energy,* 82 (**2008**) 1145-1153.

[106] A.L. Dicks, Molten Carbonate Fuel Cells, *Curr Opin Solid St M,* 8 (**2004**) 379-383.

[107] L.X. Sang, M. Cai, Y.B. Zhao, N. Ren, Y.T. Wu, C. Burda, Mixed Metal Carbonates/Hydroxides for Concentrating Solar Power Analyzed with DSC and XRD, *Solar Energy Materials and Solar Cells,* 140 (**2015**) 167-173.

[108] J.B. Bates, G.E. Boyd, M.H. Brooker, A.S. Quist, Raman Spectra of Molten Alkali-Metal Carbonates, *J Phys Chem-Us,* 76 (**1972**) 1565-1571.

[109] N. Pfleger, T. Bauer, C. Martin, M. Eck, A. Worner, Thermal Energy Storage - Overview and Specific Insight into Nitrate Salts for Sensible and Latent Heat Storage, *Beilstein J Nanotechnol,* 6 (**2015**) 1487-1497.

[110] C.L. Chen, T. Tran, R. Olivares, S. Wright, S.Y. Sun, Coupled Experimental Study and Thermodynamic Modeling of Melting Point and Thermal Stability of Li_2CO_3-Na_2CO_3-K_2CO_3 Based Salts, *Journal of Solar Energy Engineering-Transactions of the Asme,* 136 (**2014**).

[111] M. Kawase, Y. Mugikura, Y. Izaki, T. Watanabe, Y. Ito, Effects of Fluoride on the Performance of MCFCs, *J Power Sources,* 124 (**2003**) 52-58.

[112] M. Mizuhata, A.B. Beleke, H. Watanabe, Y. Harada, S. Deki, Effect of Gamma-$LiAlO_2$ Powder on Ionic Conductivity of Coexisting Single Alkali Carbonates, *Electrochim Acta,* 53 (**2007**) 71-78.

[113] M. Mizuhata, S. Deki, Effect of Surface Properties of Porous Solid Materials on Physicochemical Properties of Molten Carbonate, *J Rare Earth,* 23 (**2005**) 1-15.

[114] S.L. Schiefelbein, N.A. Fried, K.G. Rhoads, D.R. Sadoway, A High-Accuracy, Calibration-Free Technique for Measuring the Electrical Conductivity Of Liquids, *Rev Sci Instrum,* 69 (**1998**) 3308-3313.

[115] J.Y. Kim, Y.S. Choi, S.E. Bae, I. Yum, D.H. Kim, J.W. Yeon, K. Song, Electrical Conductivity Measurement of Molten Salts Using a Two-Electrode Alternative Current Impedance Method, *Asian J Chem,* 25 (**2013**) 7028-7030.

[116] S. Tanase, Y. Miyazaki, M. Yanagida, T. Kodama, Corrosion Study on Ceramics for Conductance Measurements of Molten Carbonates, *Ceramics International,* 11 (**1985**) 71-72.

[117] K.B. Kim, Electrical Conductivity Measurements of Molten Alkaline-Earth Fluorides, *J Electrochem Soc,* 139 (**1992**) 1027-1033.

[118] Y. Miyazaki, M. Yanagida, K. Tanimoto, T. Kodama, S. Tanase, An Apparatus for Electrical Conductance Measurements with Molten Carbonates, *J Electrochem Soc,* 133 (**1986**) 1402-1404.

[119] A.E. Gheribi, J.A. Torres, P. Chartrand, Recommended Values for the Thermal Conductivity of Molten Salts Between the Melting and Boiling Points, *Solar Energy Materials and Solar Cells,* 126 (**2014**) 11-25.

[120] V. Khokhlov, I. Korzun, V. Dokutovich, E. Filatov, Heat Capacity and Thermal Conductivity of Molten Ternary Lithium, Sodium, Potassium, and Zirconium Fluorides Mixtures, *J Nucl Mater,* 410 (**2011**) 32-38.

[121] R. Serrano-Lopez, J. Fradera, S. Cuesta-Lopez, Molten Salts Database for Energy Applications, *Chem Eng Process,* 73 (**2013**) 87-102.

[122] X. Zhang, M. Fujii, Simultaneous Measurements of the Thermal Conductivity and Thermal Diffusivity of Molten Salts with a Transient Short-Hot-Wire Method, *Int J Thermophys,* 21 (**2000**) 71-84.

[123] M. Hoshi, T. Omotani, A. Nagashima, Transient Method to Measure the Thermal-Conductivity of High-Temperature Melts Using a Liquid-Metal Probe, *Rev Sci Instrum,* 52 (**1981**) 755-758.

[124] A.E. Gheribi, S. Poncsak, R. St-Pierre, L.I. Kiss, P. Chartrand, Thermal Conductivity of Halide Solid Solutions: Measurement and Prediction, *J Chem Phys,* 141 (**2014**) 104508-104501-104512.

[125] A.E. Gheribi, M. Salanne, P. Chartrand, Thermal Transport Properties of Halide Solid Solutions: Experiments vs Equilibrium Molecular Dynamics, *J Chem Phys,* 142 (**2015**) 124109-124101-124108.

[126] Y. Tada, M. Harada, M. Tanigaki, W. Eguchi, Laser Flash Method for Measuring Thermal-Conductivity of Liquids - Application to Molten-Salts, *Ind Eng Chem Fund,* 20 (**1981**) 333-336.

[127] X. An, J. Cheng, P. Zhang, Z. Tang, J. Wang, Determination and Evaluation of the Thermophysical Properties of an Alkali Carbonate Eutectic Molten Salt, *Faraday Discuss,* 190 (**2016**) 327-338.

[128] D. Sanchez-Rodriguez, J.P. Lopez-Olmedo, J. Farjas, P. Roura, Determination of thermal conductivity of powders in different atmospheres by differential scanning calorimetry, *J Therm Anal Calorim,* 121 (**2015**) 469-473.

[129] G. Hakvoort, L.L. Vanreijen, A.J. Aartsen, Measurement of the Thermal-Conductivity of Solid Substances by DSC, *Thermochim Acta,* 93 (**1985**) 317-320.

[130] E.T. Measurements, Standard Terminology Relating to Thermal Analysis and Rheology, **2011**.

[131] C.P. Camirand, Measurement of Thermal Conductivity by Differential Scanning Calorimetry, *Thermochim Acta,* 417 (**2004**) 1-4.

[132] J.H. Flynn, D.M. Levin, A Method for the Determination of Thermal-Conductivity of Sheet Materials by Differential Scanning Calorimetry (DSC), *Thermochim Acta,* 126 (**1988**) 93-100.

[133] S.M. Marcus, R.L. Blaine, Thermal Conductivity of Polymers, Glasses and Ceramics by Modulated DSC, *Thermochim Acta,* 243 (**1994**) 231-239.

[134] D. Sánchez-Rodríguez, J.P. López-Olmedo, J. Farjas, P. Roura, Determination of Thermal Conductivity of Powders in Different Atmospheres by Differential Scanning Calorimetry, *J Therm Anal Calorim,* 121 (**2015**) 469-473.

[135] M. Pujula, D. Sanchez-Rodriguez, J.P. Lopez-Olmedo, J. Farjas, P. Roura, Measuring Thermal Conductivity of Powders with Differential Scanning Calorimetry A Simplified Method, *J Therm Anal Calorim,* 125 (**2016**) 571-577.

[136] M. Hu, D.M. Yu, J.B. Wei, Thermal conductivity Determination of Small Polymer Samples by Differential Scanning Calorimetry, *Polym Test,* 26 (**2007**) 333-337.

[137] X.H. An, J.H. Cheng, H.Q. Yin, L.D. Xie, P. Zhang, Thermal Conductivity of High Temperature Fluoride Molten Salt Determined by Laser Flash Technique, *Int J Heat Mass Tran,* 90 (**2015**) 872-877.

[138] Y.X. Zhang, Y.L. Wang, Y. Wang, F.L. Chen, C.R. Xia, Random-Packing Model for Solid Oxide Fuel Cell Electrodes with Particle Size Distributions, *J Power Sources,* 196 (**2011**) 1983-1991.

[139] EIS Equivalent Circuits, Electrochemical Impedance Spectroscopy in PEM Fuel Cells, *Springer London,* London, **2010**, pp. 139-192.

[140] J.L. Trinstancho-Reyes, M. Sanchez-Carrillo, R. Sandoval-Jabalera, V.M. Orozco-Carmona, F. Almeraya-Calderon, J.G. Chacon-Nava, J.G. Gonzalez-Rodriguez, A. Martinez-Villafane, Electrochemical Impedance Spectroscopy Investigation of Alloy Inconel 718 in Molten Salts at High Temperature, *Int J Electrochem Sc,* 6 (**2011**) 419-431.

[141] S.A. Muhammed Ali, R.E. Rosli, A. Muchtar, A.B. Sulong, M.R. Somalu, E.H. Majlan, Effect of Sintering Temperature on Surface Morphology and Electrical Properties of Samarium-Doped Ceria Carbonate for Solid Oxide Fuel Cells, *Ceramics International,* 41 (**2015**) 1323-1332.

[142] L.D. Fan, C.X. He, B. Zhu, Role of Carbonate Phase in Ceria-Carbonate Composite for Low Temperature Solid Oxide Fuel Cells: A Review, *Int J Energ Res,* 41 (**2017**) 465-481.

[143] S. Shawuti, M.A. Gulgun, Solid Oxide-Molten Carbonate Nano-Composite Fuel Cells: Particle Size Effect, *J Power Sources,* 267 (**2014**) 128-135.

[144] R. Pal, On the Electrical Conductivity of Particulate Composites, *Journal of Composite Materials,* 41 (**2007**) 2499-2511.

[145] J.C. Maxwell, A Treatise on Electricity and Magnetism, *Clarendon press,* London, **1881**.

[146] G.R. Gavalas, Comparison of Effective Conductivities Calculated by the Effective Medium Approximation and the Self Consistent Approximation for Core-Shell Particulate Composites, *AIP Advances,* 7 (**2017**) 095222-095221-095226.

[147] M. Mizuhata, S. Suganuma, Y. Harada, S. Deki, Anomalous Properties of LiK_2CO_3 Melts Coexisting with Porous Inorganic Powder, *Electrochemistry,* 73 (**2005**) 680-685.

[148] T. Wang, D. Mantha, R.G. Reddy, Novel High Thermal Stability LiF–Na_2CO_3–K_2CO_3 Eutectic Ternary System for Thermal Energy Storage Applications, *Solar Energy Materials and Solar Cells,* 140 (**2015**) 366-375.

[149] J. Trahan, S. Kuravi, D.Y. Goswami, M. Rahman, E. Stefanakos, Thermal Characterization of High Temperature Inorganic Phase Change Materials for Thermal Energy Storage Applications, (**2012**) 623-630.

[150] A.T. Ward, G.J. Janz, Molten carbonate electrolytes: Electrical Conductance, Density and Surface Tension of Binary and Ternary Mixtures, *Electrochim Acta,* 10 (**1965**) 849-857.

[151] M.R. Kessler, Advanced Topics in Characterization of Composites, *Trafford,* **2004**.

[152] G.J. Snyder, A.H. Snyder, Figure of Merit ZT of a Thermoelectric Device Defined from Materials Properties, *Energ Environ Sci,* 10 (**2017**) 2280-2283.

[153] X. Zhang, L.D. Zhao, Thermoelectric Materials: Energy Conversion Between Heat and Electricity, *J Materiomics,* 1 (**2015**) 92-105.

[154] H. Nafe, Conductivity of Alkali Carbonates, Carbonate-Based Composite Electrolytes and IT-SOFC, *Ecs J Solid State Sc,* 3 (**2013**) N7-N14.

[155] B. Zhu, X. Liu, P. Zhou, X. Yang, Z. Zhu, W. Zhu, Innovative Solid Carbonate–Ceria Composite Electrolyte Fuel Cells, *Electrochemistry Communications,* 3 (**2001**) 566-571.

[156] E. Antolini, The Stability of $LiAlO_2$ Powders and Electrolyte Matrices in Molten Carbonate Fuel Cell Environment, *Ceramics International,* 39 (**2013**) 3463-3478.

[157] Z.W. Ge, F. Ye, H. Cao, G.H. Leng, Y. Qin, Y.L. Ding, Carbonate-Salt-Based Composite Materials for Medium- and High-Temperature Thermal Energy Storage, *Particuology,* 15 (**2014**) 77-81.

[158] N. Gokon, S. Nakamura, K. Matsubara, T. Kodama, Carbonate Molten-Salt Absorber/Reformer: Heating and Steam Reforming Performance of Reactor Tubes, *Enrgy Proced,* 49 (**2014**) 1940-1949.

[159] T. Jacobsen, Single Electrode Heat Effects, *J Electrochem Soc,* 124 (**1977**) 207-210.

[160] D. Cederkrantz, A. Saramat, G.J. Snyder, A.E.C. Palmqvist, Thermal Stability and Thermoelectric Properties of P-type $Ba_8Ga_{16}Ge_{30}$ Clathrates, *J Appl Phys,* 106 (**2009**) 074509-074501-074507.

[161] J. Josserand, V. Devaud, G. Lagger, H. Jensen, H.H. Girault, Hydrovoltaic Cells. Part II: Thermogalvanic Cells and numerical Simulations of Thermal Diffusion Potentials, *J Electroanal Chem,* 565 (**2004**) 65-75.

[162] M.A. Lazar, D. Al-Masri, D.R. MacFarlane, J.M. Pringle, Enhanced Thermal Energy Harvesting Performance of a Cobalt Redox Couple in Ionic Liquid-Solvent Mixtures, *Phys Chem Chem Phys,* 18 (**2016**) 1404-1410.

[163] H. Timm, J. Janek, On the Soret Effect in Binary Nonstoichiometric Oxides—Kinetic Demixing of Cuprite in a Temperature Gradient, *Solid State Ionics,* 176 (**2005**) 1131-1143.

[164] T.J. Salez, B.T. Huang, M. Rietjens, M. Bonetti, C. Wiertel-Gasquet, M. Roger, C.L. Filomeno, E. Dubois, R. Perzynski, S. Nakamae, Can Charged Colloidal Particles Increase the Thermoelectric Energy Conversion Efficiency?, *Phys Chem Chem Phys,* 19 (**2017**) 9409-9416.

[165] F.J.A. Loureiro, S. Rajesh, F.M.L. Figueiredo, F.M.B. Marques, Stability of Metal Oxides Against Li/Na Carbonates in Composite Electrolytes, *RSC Advances,* 4 (**2014**) 59943-59952.

[166] E. Bordes-Richard, P. Courtine, Optical Basicity: a Scale of Acidity/Basicity of Solids and its Application to Oxidation Catalysis, in: J.L.G. Fierro (Ed.) Metal Oxides: Chemistry and Applications, *CRC Press LLC (Boca Raton, FL, United States),* **2006**, pp. 319-352.

[167] J.R.H. Ross, Chapter 4 - Catalyst Preparation, Heterogeneous Catalysis, *Elsevier*, Amsterdam, **2012**, pp. 65-96.

[168] N. Andreu, I. Baraille, H. Martinez, R. Dedryvère, M. Loudet, D. Gonbeau, New Investigations on the Surface Reactivity of Layered Lithium Oxides, *The Journal of Physical Chemistry C,* 116 (**2012**) 20332-20341.

[169] S. Scaccia, S. Frangini, Effect of Various Electrolyte Compositions on the NiO Degradation in Molten Carbonates, (**2005**) 347-350.

[170] H. Metiu, S. Chrétien, Z. Hu, B. Li, X. Sun, Chemistry of Lewis Acid–Base Pairs on Oxide Surfaces, *The Journal of Physical Chemistry C,* 116 (**2012**) 10439-10450.

[171] J. Hu, L. Chen, R. Richards, Properties, Synthesis and Applications of Highly Dispersed Metal Oxide Catalysts, **2009**.

[172] A. Ali, A. Rafique, M. Kaleemullah, G. Abbas, M. Ajmal Khan, M.A. Ahmad, R. Raza, Effect of Alkali Carbonates (Single, Binary, and Ternary) on Doped Ceria: A Composite Electrolyte for Low-Temperature Solid Oxide Fuel Cells, *ACS Applied Materials & Interfaces,* 10 (**2018**) 806-818.

[173] S.J. Heo, B. Hu, V. Manthina, A. Hilmi, C.-Y. Yuh, A. Surendranath, P. Singh, Stability of Lithium Aluminate in Reducing and Oxidizing Atmospheres at 700 °C, *Int J Hydrogen Energ,* 41 (**2016**) 18884-18892.

[174] K. Matsuzawa, G. Tatezawa, Y. Matsuda, S. Mitsushima, N. Kamiya, K. Ota, Effects of Rare-Earth Additives in Li/Na Eutectic Carbonate for Decreasing the Solubility of NiO, *J Electrochem Soc,* 152 (**2005**) A1116-A1120.

[175] M. Sulaiman, A.A. Rahman, N.S. Mohamed, Sol-gel Synthesis and Characterization of Li_2CO_3-Al_2O_3 Composite Solid Electrolytes, *Ionics,* 22 (**2016**) 327-332.

[176] L.L. Yang, H. Sun, S.L. Wang, L.H. Jiang, G.Q. Sun, A Solid State Thermogalvanic Cell Harvesting Low-Grade Thermal Energy, *Int J Hydrogen Energ,* 42 (**2017**) 25877-25881.

[177] A.I.B. Rondao, S.G. Patricia, F.M.L. Figueiredo, F.M.B. Marques, Composite Electrolytes for Fuel Cells: Long-Term Stability Under Variable Atmosphere, *Int J Hydrogen Energ,* 39 (**2014**) 5460-5469.

[178] V. Chauvaut, Study of cerium species in molten Li_2CO_3–Na_2CO_3 in the Conditions used in Molten Carbonate Fuel Cells. Part I: Thermodynamic, Chemical and Surface Properties, *J Appl Electrochem,* 30 (**2000**) 1405-1413.

[179] H.J. Choi, J.J. Lee, S.H. Hyun, H.C. Lim, Phase and Microstructural Stability of Electrolyte Matrix Materials for Molten Carbonate Fuel Cells, *Fuel Cells,* 10 (**2010**) 613-618.

[180] R. Dronskowski, Reactivity and Acidity of Li in Lithium Aluminum Oxide ($LiAlO_2$) Phases, *Inorganic Chemistry,* 32 (**1993**) 1-9.

[181] L. Lei, D.W. He, Y.T. Zou, W. Zhang, Z. Wang, M. Jiang, M.L. Du, Phase Transitions of $LiAlO_2$ at High Pressure and High Temperature, *Journal of Solid State Chemistry,* 181 (**2008**) 1810-1815.

[182] I.D. Zakir'yanova, I.V. Korzun, V.A. Khokhlov, V.N. Dokutovich, E.V. Nikolaeva, B.D. Antonov, Specific Features of the Interaction of α- and γ-Modifications of Al_2O_3 with Carbonate and Carbonate-Chloride Melts, *Russian Journal of Applied Chemistry,* 89 (**2016**) 1066-1071.

[183] T.I. Quickenden, Y. Mua, The Power Conversion Efficiencies of a Thermogalvanic Cell Operated in 3 Different Orientations, *J Electrochem Soc,* 142 (**1995**) 3652-3659.

[184] D.P. Dong, H.T. Guo, G.Y. Li, L.F. Yan, X.T. Zhang, W.H. Song, Assembling Hollow Carbon Sphere-Graphene Polylithic Aerogels for Thermoelectric Cells, *Nano Energy,* 39 (**2017**) 470-477.

[185] S.H. Park, Y. Jin, J. Cha, K. Hong, Y. Kim, H. Yoon, C.-Y. Yoo, I. Chung, High-Power-Density Skutterudite-Based Thermoelectric Modules with Ultralow Contact Resistivity Using Fe–Ni Metallization Layers, *ACS Applied Energy Materials,* 1 (**2018**) 1603-1611.

[186] T.A. Siddique, S. Balamurugan, S.M. Said, N.A. Sairi, W.M.D.W. Normazlan, Synthesis and Characterization of Protic Ionic Liquids as Thermoelectrochemical Materials, *Rsc Advances,* 6 (**2016**) 18266-18278.

[187] S. LeBlanc, Thermoelectric generators: Linking Material Properties and Systems Engineering for Waste Heat Recovery Applications, *Sustainable Materials and Technologies,* 1-2 (**2014**) 26-35.

[188] S. LeBlanc, S.K. Yee, M.L. Scullin, C. Dames, K.E. Goodson, Material and Manufacturing Cost Considerations for Thermoelectrics, *Renew Sust Energ Rev,* 32 (**2014**) 313-327.

[189] K. Yazawa, A. Shakouri, Cost-efficiency Trade-Off and the Design of Thermoelectric Power Generators, *Environ Sci Technol,* 45 (**2011**) 7548-7553.

[190] T.J. Abraham, D.R. MacFarlane, J.M. Pringle, Seebeck Coefficients in Ionic Liquids--Prospects for Thermo-Electrochemical Cells, *Chem Commun (Camb),* 47 (**2011**) 6260-6262.

[191] K. Ota, S. Mitsushima, S. Kato, S. Asano, H. Yoshitake, N. Kamiya, Solubilities of Nickel Oxide in Molten Carbonate, *J Electrochem Soc,* 139 (**1992**) 667-671.

[192] E. Antolini, The Stability of Molten Carbonate Fuel Cell Electrodes: A Review of Recent Improvements, *Appl Energ,* 88 (**2011**) 4274-4293.

[193] E. Antolini, A New Way of Obtaining $Li_xNi_{1-x}O$ Cathodes for Molten-Carbonate Fuel Cells, *J Power Sources,* 40 (**1992**) 265-270.

[194] E. Antolini, Behaviour of Ni, NiO and $Li_xNi_{1-x}O$ in Molten Alkali Carbonates, *Journal of Materials Science,* 35 (**2000**) 1501-1505.

[195] M. Mohamedi, Y. Hisamitsu, T. Kudo, T. Itoh, I. Uchida, Explicit Study on the Oxidation Mechanism of Nickel in Molten Li_2CO_3-K_2CO_3, *J Solid State Electr,* 5 (**2001**) 538-545.

[196] Y. Izaki, Y. Mugikura, T. Watanabe, M. Kawase, J.R. Selman, Direct Observation of the Oxidation Nickel in Molten Carbonate, *J Power Sources,* 75 (**1998**) 236-243.

[197] M.S. Yazici, J.R. Selman, Oxidation-Lithiation of Nickel, Iron and Cobalt in Contact with Molten Carbonate, *Solid State Ionics,* 124 (**1999**) 149-160.

[198] J. Youn, B. Ryu, M. Shin, H. Kang, H. Kim, I. Chang, T. Lee, H. Kwon, Effect of CO_2 Partial Pressure on the Cathode Lithiation in Molten Carbonate Fuel Cells, *Int J Hydrogen Energ,* 37 (**2012**) 19289-19294.

[199] Z. Li, C. Wang, X. Ma, L. Yuan, J. Sun, Synthesis, Structures and Electrochemical Properties of $Li_xNi_{1-x}O$, *Materials Chemistry and Physics,* 91 (**2005**) 36-39.

[200] S. Iinou, N. Motohira, N. Kamiya, K.-i. Ota, Formation of Li-Doped NiO and $LiNiO_2$ in Molten Carbonate, *Bulletin of the Chemical Society of Japan,* 72 (**1999**) 321-326.

[201] K.F. Du, K.Y. Zheng, Z.G. Chen, H. Zhu, F.X. Gan, D.H. Wang, Unusual temperature effect on the stability of nickel anodes in molten carbonates, *Electrochim Acta,* 245 (**2017**) 402-408.

[202] C. Belhomme, M. Cassir, J. Devynck, G. Gregoire, Synthesis by a Soft Chemistry Route and Characterization of $Li_xNi_{1-x}O$ ($0 < x < 0.5$) Compounds: Behavior in Molten Carbonates, *Journal of Materials Science,* 35 (**2000**) 2683-2688.

[203] H.-H. Parkt, C.-I. Jang, H.-S. Shin, K.-T. Lee, Fabrication and Characteristics of Porous Ni and NiO(Li) Cathodes for MCFC, *Korean Journal of Chemical Engineering,* 13 (**1996**) 35-39.

[204] R. Sanchez-Tovar, M.T. Montanes, J. Garcia-Anton, Thermogalvanic Corrosion and Galvanic Effects of Copper and AISI 316L Stainless Steel Pairs in Heavy LiBr Brines Under Hydrodynamic Conditions, *Corros Sci,* 60 (**2012**) 118-128.

[205] H.A.H. Alzahrani, J.J. Black, D. Goonetilleke, J. Panchompoo, L. Aldous, Combining Thermogalvanic Corrosion and Thermogalvanic Redox Couples for Improved Electrochemical Waste Heat Harvesting, *Electrochemistry Communications,* 58 (**2015**) 76-79.

[206] M.J. Escudero, T. Rodrigo, J. Soler, L. Daza, Electrochemical Behaviour of Lithium–Nickel Oxides in Molten Carbonate, *J Power Sources,* 118 (**2003**) 23-34.

[207] H. Im, T. Kim, H. Song, J. Choi, J.S. Park, R. Ovalle-Robles, H.D. Yang, K.D. Kihm, R.H. Baughman, H.H. Lee, T.J. Kang, Y.H. Kim, High-Efficiency Electrochemical Thermal Energy Harvester Using Carbon Nanotube Aerogel Sheet Electrodes, *Nat Commun,* 7 (**2016**) 10600.

[208] C.-G. Lee, K. Yamada, T. Nishina, I. Uchida, In Situ NiO Dissolution Behavior in $(Li + Na)CO_3$ Melts Under Pressurized Oxidant Gas Atmospheres, *J Power Sources,* 62 (**1996**) 145-147.

[209] K. Du, K. Zheng, Z. Chen, H. Zhu, F. Gan, D. Wang, Unusual temperature effect on the stability of nickel anodes in molten carbonates, *Electrochim Acta,* 245 (**2017**) 410-416.

[210] E. Antolini, M. Leonini, V. Massarotti, A. Marini, V. Berbenni, D. Capsoni, On the Role of Lithium Carbonate in the Preparation of Doped Nickel Oxide Cathodes for Molten Carbonate Fuel Cells, *Solid State Ionics,* 39 (**1990**) 251-261.

[211] J. P. T. Vossen, L. Plomp, J.H.W. Dewit, Corrosion of Nickel in Molten Carbonate, **1994**.

[212] S. Kjelstrup, D. Bedeaux, Non-Equilibrium Thermodynamics of Heterogeneous Systems, *World Scientific*, Hackensack, NJ, **2008**.

[213] K.S. Førland, T. Førland, S.K. Ratkje, Irreversible Thermodynamics: Theory and Applications, *Wiley*, **1989**.

List of Figures

Figure 1.1.1 (Top) Schematic representation of thermocell and **(bottom)** five subsystems of thermocell and the notation used for transport properties. 1

Figure 1.3.1 The change in the Seebeck coefficient of binary AgCl – LiCl electrolyte with Ag electrodes **(a)** function of temperature and **(b)** function of AgCl concentration at 800 ºC [36]. 10

Figure 1.3.2 The transport phenomenon of $AgNO_3$ - $LiNO_3$ electrolyte mixture with Ag electrodes at 260 ºC [6]. 12

Figure 1.3.3 Thermocell Seebeck coefficient for eutectic (LiCl-KCl) electrolyte mixture with a different concentration of **(a)** silver or copper **c**hloride [41] and **(b)** lithium hydride [42]. 13

Figure 1.3.4 The Seebeck coefficient and electrical conductivity as a function of Ag*X* (*X* = I, Cl, Br) concentration in Ag_2Se at 900 ºC [49, 50]. 16

Figure 1.3.5 The Seebeck coefficient as a function of AgI concentration in the electrolyte mixture at 1000 K [59]. 17

Figure 1.3.6 Thermocell Seebeck coefficient of electrolyte mixtures with **(a)** $PbCl_2$-LiCl and **(b)** NaF-AlF_3-Al_2O_3 in the presence of liquid metal or gas electrodes [66]. 20

Figure 1.3.7 Initial thermoelectric power of the electrolyte mixture (Cu,Ag)X where X = I, Br, Cl with copper or silver electrodes [67]. 21

Figure 1.3.8 Seebeck coefficient of thermocells with $PbCl_2$-LiCl electrolyte mixtures and with both liquid metal or gas electrodes [39]. 22

Figure 1.3.9 Schematic of the different thermocell setups with molten salt electrolyte. 23

Figure 2.1.1 The gas electrode fabrication **(a)** 5-bored alumina tube and **(b)** the metal current collector and S-type thermocouple arrangement in the alumina tube. 29

Figure 2.1.2 In-situ lithiation of the Ni electrodes to attain ($Li_xNi_{1-x}O$) phase. 31

Figure 2.1.3 The laboratory thermocell construction and apparatus. 32

Figure 2.1.4 The cross-sectional schematic representation of the molten carbonate thermocell. 34

Figure 2.1.5 The cross-sectional schematic representation of the thermocell connected with external resistance in parallel for power output measurement. 35

Figure 2.3.1 The DSC sampling for the thermal conductivity measurement **(a)** blank measurement, **(b,c,d)** with different quantity of electrolyte mixtures (30, 45, 60 mg). 41

Figure 2.3.2 Schematic of the conductivity cell and capillary electrode used to measure the conductivity of the electrolyte mixtures by AC impedance spectroscopy. 45

Figure 3.1.1 Cross sectional view of the thermocell with reference scale for positioning the electrode to create the required temperature gradient.. 51

Figure 3.1.2 X-ray diffraction patterns for the electrolyte mixer after **(a,b)** and before **(c)** thermocell measurement. **(d)** EDS elemental analysis of the electrolyte after thermocell measurement (respective 1 sigma wt% error value was mentioned in the brackets).. 53

Figure 3.1.3 **(a)** The measured potential and temperature difference and, **(b)** Seebeck coefficient plot for cell C with electrode gas flow rate of 18.6 ml/min. 55

Figure 3.1.4 Measured potential versus time for electrode temperature difference of 20 °C with varying electrode gas flow rate (Cell A-D). 56

Figure 3.1.5 Potential measured with a thermocell, at constant electrode position with change in gas flow rates.. 57

Figure 3.1.6 **(a)** Seebeck coefficient plot for cell D, and **(b)** Measured potential versus temperature difference in the cell H.. 58

Figure 3.2.1 Cross-sectional schematic representation of the molten carbonate thermocell. 64

Figure 3.2.2 DSC analysis to show the change in **(a)** liquidus and **(b)** solidification temperatures of the electrolyte mixtures in **Table 3.2.2**. 67

Figure 3.2.3 **(a)** Thermocell measurement with the LNKC electrolyte mixture at 415 °C and **(b)** the Seebeck coefficient of the thermocells different electrolyte mixtures in **Table 3.2.2**. 69

Figure 3.2.4 Schematic to illustrate the ionic arrangement in the LNC electrolyte mixture at initial conditions. 70

Figure 3.2.5 XRD phase analysis of the LNKC-LF electrolyte mixture, before and after the thermocell measurement at 550 °C. 72

Figure 3.2.6 Thermochemical stablility of the different electrolyte mixtures by TGA analysis.......... 73

Figure 3.2.7 Seebeck coefficient of the LNKC thermocell at different average cell temperatures merged with the TGA weight loss profile.. 74

Figure 3.2.8 SEM surface morphology of the gold electrodes before thermocell measurements........ 76

Figure 3.2.9 SEM surface morphology of the gold electrodes used in thermocells with different electrolyte mixtures at 550 °C... 77

Figure 3.3.1 Schematic of the conductivity cell and capillary electrode used to measure the conductivity of the electrolyte mixtures by AC impedance spectroscopy. 83

Figure 3.3.2 A cross-sectional view of the thermocell setup, with molten carbonate electrolyte mixtures and ($CO_2|O_2$) gas electrodes.. 85

Figure 3.3.3 The solid MgO particle size distribution measured by the laser diffraction particle size analyzer. 87

Figure 3.3.4 The AC-Impedance spectroscopy measurement to determine the electrical conductivity of the different electrolyte mixtures. 88

Figure 3.3.5 Influence of the MgO surface area on melting behavior of the electrolyte mixtures. 89

Figure 3.3.6 (a) Recorded DSC heat flow and TGA weight loss profiles (numbering along the temperature profile are the segments listed in **Table 3.3.1**) and **(b)** Influence the thermal cycles and reduction in thermal contact resistance. 90

Figure 3.3.7 (a) The endothermic peak (segment 8 - Al disk melting) of measurements with different quantity of LNC-MO(3) and **(b)** estimation of the absolute thermal conductivity. 92

Figure 3.3.8 (a) The measured potential and temperature difference between the electrodes and, **(b)** the estimation of thermocell Seebeck coefficient. 94

Figure 3.3.9 (a-c) Long-term potential measurement at the same temperature difference between the electrodes and **(d)** the thermocell Seebeck coefficient with different electrolyte mixtures. 95

Figure 3.3.10 Dilatometer measurement to determine the change in density. 98

Figure 3.3.11 DSC measurement to determine the C_p of LNC-MO(3). 99

Figure 3.4.1 The cross-sectional schematic representation of the thermocell. Open circuit potential is measured to estimated the Seebeck coefficient and potential across the load resistance is measured to determine the power output. 104

Figure 3.4.2 Short time thermocell potential (Δφ) and respective temperature difference (ΔT) between the electrodes for all the electrolyte mixtures with different solid oxides. 106

Figure 3.4.3 Change in melting behavior of the eutectic $(Li,Na)_2CO_3$ in mixture with different solid oxides. 107

Figure 3.4.4 XRD diffraction of the electrolyte mixtures dispersed with CeO_2 or Al_2O_3, before (as-prepared) and after (re-solidified) the short time thermocell measurement at 550 °C, and the JCPDS standard of the solid oxide. 108

Figure 3.4.5 XRD diffraction of the electrolyte mixtures dispersed with $LiAlO_2$ or MgO, before (as-prepared) and after (re-solidified) the short time thermocell measurement at 550 °C, and the JCPDS standard of the solid oxide. 109

Figure 3.4.6 Suitable standard X-ray diffraction pattern of pure and eutectic binary (Li, Na) carbonates. 110

Figure 3.4.7 Long-term thermocells potential measurement with different electrolyte mixtures. 112

Figure 3.4.8 The thermocell Seebeck coefficient of the long-term measurements with different electrolyte mixtures. 112

Figure 3.4.9 XRD diffraction pattern of the LNC-LAO and LNC-AO electrolyte mixtures before (as-prepared) and after (re-solidified) long-term thermocell measurement at 550 °C. 113

Figure 3.4.10 XRD phase analysis on the re-solidified electrolyte mixture (containing $LiAlO_2$) after a water wash. 114

Figure 3.4.11 XRD phase analysis on the re-solidified electrolyte mixture (containing Al_2O_3) after a water wash. 115

Figure 3.4.12 The power output of the thermocells with the electrolyte mixture containing MgO or CeO_2. 117

Figure 3.5.1 (Top) Cross-sectional view of the thermocell and **(bottom)** the five subsystems of the cell, the notation used for transport properties. 123

Figure 3.5.2 In-situ lithiation of the Ni electrodes to attain ($Li_xNi_{1-x}O$) phase. 125

Figure 3.5.3 X-ray diffraction patterns for the nickel-based current collectors before the thermocell measurement. 128

Figure 3.5.4 SEM surface morphology of the Ni-based current collectors before thermocell measurement (**left** - low & **right** - high magnification of the same sample). 129

Figure 3.5.5 Thermocell Seebeck coefficient measurement as a function of time. 131

Figure 3.5.6 The direct current measurement to determine the power output density of the thermocells with different current collectors. 132

Figure 3.5.7 X-ray diffraction patterns for the nickel-based current collectors after the thermocell measurement. 134

Figure 3.5.8 SEM surface morphology of (**a-c**) the in-situ oxidized $Li_{0.1}Ni_{0.9}O$ and **(d-f)** the ex-situ oxidized NiO current collectors after thermocell measurement. 135

Figure 3.5.9 SEM surface morphology of the gold current collector **a** - before and **b** - after the thermocell measurements at 550 °C in electrolyte mixture with 45 vol% of $(Li,Na)_2CO_3$ in MgO. .. 137

Figure A1.1 (Top) Cross-sectional view of the thermocell and **(bottom)** the five subsystems of the cell, the notation used for transport properties [28, 63, 68]. 166

List of Tables

Table 1.3.1 Seebeck coefficient of thermocells with various single molten salt electrolytes and metal electrodes. 4

Table 1.3.2 Seebeck coefficient of thermocells with various single molten salt electrolytes and gas electrodes. 5

Table 1.3.3 Calculated heat of transport for thermocell with chlorine gas electrodes [26]. 6

Table 1.3.4 The transported entropy of ions in single molten salt electrolytes thermocells with both metal and gas electrode pairs. 7

Table 1.3.5 Seebeck coefficient of thermocells with binary electrolyte mixtures (common anion and different cations) 9

Table 1.3.6 Seebeck coefficient of the electrolyte mixture with common cations and different anions [43, 44]. 14

Table 1.3.7 Transport quantities of molten metal – molten salt electrolyte thermocells [45, 46]. 15

Table 1.3.8 Seebeck coefficient of thermocells with molten carbonates and solid oxide electrolyte mixture with gas electrodes. 18

Table 2.2.1 Details of the samples subjected to laser particle size analyzer. 38

Table 2.3.1 The DSC temperature program used for thermal conductivity measurement. 42

Table 3.1.1 Electrode gas flow rate and MgO to carbonate ratio used in the experiments. 50

Table 3.1.2 Seebeck coefficient of the cells with varying electrode gas flow rate and average temperature 550 °C. 54

Table 3.1.3 Seebeck coefficient of the cells with different ratio MgO in electrolyte and average temperature 550 °C. 54

Table 3.2.1 The melting point and lattice energy [95] of the molten salts in the electrolyte mixture. 63

Table 3.2.2 The electrolyte molten melt composition dispersed in 55 vol % of solid MgO. 63

Table 3.2.3 Experimental algorithm used for the DSC/TGA thermal analysis. 66

Table 3.3.1 The DSC temperature program used for thermal conductivity measurement. 84

Table 3.3.2 The composition of the electrolyte mixtures and the electrical conductivity measured by using AC impedance spectroscopy with capillary electrodes. 86

Table 3.3.3 The thermal conductivities measured by DSC analysis. 93

Table 3.3.4 Effect of MgO surface area in the electrical and thermal conductivity of the electrolyte mixture. 93

Table 3.3.5 Effect of MgO surface area in thermocell Seebeck coefficient (initial/short time). 96

Table 3.3.6 The dimensionless figure of merit (ZT) of the thermocell containing LNC-MO(3). 96

Table 3.3.7 DSC temperature program used in determining the C_p. 99

Table 3.4.1 The thermocell Seebeck coefficient of the different electrolyte mixtures at short time. . 105

Table 3.4.2 Transport properties estimated from the thermocell Seebeck coefficient measured at short time (steady temperature gradient) and long time (Soret equilibrium). 113

Table 3.4.3 Estimation of the conversion efficiency for the thermocells from the power output measurement. 117

Table 3.4.4 Comparison of the molten carbonate electrolyte based thermocell power output to the other thermoelectric systems from recent literature. 118

Table 3.5.1 Structural parameters obtained from the XRD patterns shown in **Figure 3.5.3**. 128

Table 3.5.2 Thermocell measurements with different current collectors in the gas electrodes. 130

Table 3.5.3 Structural parameters obtained from the XRD patterns shown in **Figure 3.5.7**. 134

Conferences and Publications

Conference presentations

- "Molten carbonate thermocells for high-temperature waste heat recovery", Energy Research Conference**,** organized by The Norwegian Research Council, **2018** Oslo, Norway.
- "Molten carbonate electrolyte based thermocells for high-temperature waste heat recovery", *International Conference on Organic and Hybrid Thermoelectrics (ICOT),* **2018** Valencia, Spain.
- "Thermocell performance with molten carbonate electrolytes", *RSC Molten Salt Discussion Group – Christmas meeting,* **2017** London, UK.
- "Thermocell with molten carbonate electrolyte to recover waste heat", *15th UK Heat Transfer Conference,* **2017** London, UK.
- "Impact of electrolyte composition on the Seebeck coefficient of molten carbonate thermocell", *231st ECS meeting,* **2017** New Orleans, US.
- "High Seebeck coefficient thermocell with molten carbonate electrolyte", *RSC Molten Salt Discussion Group - summer meeting,* **2017** Nottingham, UK.
- "Impact of electrolyte composition on the Seebeck coefficient of molten carbonate thermocell", *CANOPENER,* **2017** Trondheim, Norway.
- "Molten carbonate thermocell for industrial waste heat harvesting and off-gas utilization", *KIFEE-9,* **2017** Kyoto, Japan.
- "Influence of Electrode Gas Flow Rate and Electrolyte Composition on Thermoelectric Power in Molten Carbonate Thermocell", *PRiME ECS,* **2016** Honolulu, *Hawaii.*
- "Influence of Electrolyte Composition on Operating Temperature of Molten Carbonate Thermo-electrochemical cell", *National Conference for Materials Technology,* **2016** Trondheim, Norway.
- "Effect of electrolyte composition and temperature in molten carbonate thermocell", *Thermoelectrics riding the wave – International Thermoelectric Society,* **2016** Norway.

List of publications

- **S Kandhasamy**, L Calandrino, OS Burheim, A Solheim, S Kjelstrup, GM Haarberg, “Influence of electrode gas flow rate and solid oxide ratio in electrolyte on the Seebeck coefficient of molten carbonate thermocell”, *ECS Transactions.,* 75 **(2016)** 171. DOI: 10.1149/07515.0171ecst
- GM Haarberg, **S Kandhasamy**, S Kjelstrup, A Solheim, “Thermoelectrochemical Cell with Molten Carbonate Electrolyte”, *Molten Salt Committee of the Electrochemical Society of Japan.,* 60 **(2017)** 23. J-Global ID: 201702263953019815
- **S Kandhasamy**, L Calandrino, OS Burheim, A Solheim, S Kjelstrup, GM Haarberg, “Influence of electrode gas flow rate and solid oxide ratio in electrolyte on the Seebeck coefficient of molten carbonate thermocell”, *J Electrochem. Soc.,* 164 **(2017)** H5271. DOI:10.1149/2.0391708jes
- GM Haarberg, **S Kandhasamy**, S Kjelstrup, MT Borset, OS Burheim, X Kang, “Thermoelectrochemical Cells with Molten Carbonate Electrolytes and Gas Electrodes”, *In Proceedings of the 12th Pacific Rim Conference on Ceramic and Glass Technology,* Hoboken, USA, John Wiley & Sons, Inc., **(2018)** 225. DOI: 10.1002/9781119494096.ch23
- **S Kandhasamy,** A Solheim, S Kjelstrup, GM Haarberg, “Electrolyte Melt Compositions for Low Temperature Molten Carbonate Thermocells”, *ACS Appl. Energy Mater.,* **(2018).** DOI: 10.1021/acsaem.8b00984
- **S Kandhasamy,** A Støre, S Kjelstrup, A Solheim, GM Haarberg, “Thermocell Electrolyte Mixture with Molten Carbonates and Solid MgO. Seebeck Coefficient and Figure of Merits” *Manuscript.*
- **S Kandhasamy,** S Kjelstrup, A Solheim, GM Haarberg, “Thermocell Performance and Physicochemical Properties of the Molten Carbonate Electrolyte Mixtures Dispersed with Different Solid Oxides” *Manuscript.*
- **S Kandhasamy,** S Kjelstrup, A Solheim, GM Haarberg, “Gas Electrodes with Nickel Based Metallic Current Collector for Molten Carbonate Electrolyte Thermocells” *Manuscript.*

Appendix A

Theory of molten carbonate thermocells

Kang *et al.* [63] and Børset *et al.* [28] derived the expression for the Seebeck coefficient (α_S) of thermocells containing molten carbonate-based electrolyte mixtures by using the non-equilibrium thermodynamics theory for heterogeneous systems. Here the derivation from the original articles are provided as supplementary material.

A1.1 System description

The thermocell containing molten carbonate electrolyte with two symmetrical gas electrodes reversible to the carbonate ion is shown in **Figure A1.1**. The electrode gas is bubbled over metallic (gold) conductors immersed in the homogeneous electrolyte mixture. The reversible ($CO_2|O_2$) gas electrode reaction in the molten carbonate electrolyte is,

$$2\mathrm{CO_2(g)} + \mathrm{O_2(g)} + 4\,\mathrm{e^-} = 2\,\mathrm{CO_3^{2-}(l)} \qquad \text{(A1.1)}$$

with the reverse reaction occure at the other electrode-electrolyte interface.

To facilitate a detailed theoretical description of the thermocell, it is dived into five subsystems as shown in **Figure A1.1** (bottom). It is divided into three subsystems with homogeneous phases and two subsystems at the electrode-electrolyte interface. The suffix means the subsystem, anode current collector (a), the two electrode surfaces (s,a and s,c), the electrolyte (e) and the cathode current collector (c). The thermocell emf will be the sum of the potential difference across each subsystem,

$$\Delta\varphi = \varphi_c - \varphi_a = \Delta_a\varphi + \Delta_{a,e}\varphi + \Delta_e\varphi + \Delta_{e,c}\varphi + \Delta_c\varphi \qquad \text{(A1.2)}$$

To establish the expression for the Seebeck coefficient, we need an expression for the emf measured between two Cu wires lead attached to the Au current collectors at room temperature ($T^{a,o} = T^{a,o} = T^0$) when the two electrodes are at temperatures $T^{s,a}$ and $T^{s,c}$.

The Seebeck coefficient is defined as the potential difference divided by the temperature difference between the electrodes in the limits $j \rightarrow 0$ and $T^{s,c} - T^{s,a} = \Delta T \rightarrow 0$,

$$\alpha_S = \left(\frac{\Delta\varphi}{\Delta T}\right)_{j\rightarrow 0,\Delta T\rightarrow 0} = \left(\frac{\Delta_a\varphi + \Delta_c\varphi}{\Delta T}\right) + \left(\frac{\Delta_{a,e}\varphi + \Delta_{e,c}\varphi}{\Delta T}\right) + \left(\frac{\Delta_e\varphi}{\Delta T}\right) \tag{A1.3}$$

where we assumed a constant temperature across each surface i.e. $T^{a,e} = T^{s,a} = T^{e,a}$ and $T^{e,c} = T^{s,c} = T^{c,e}$.

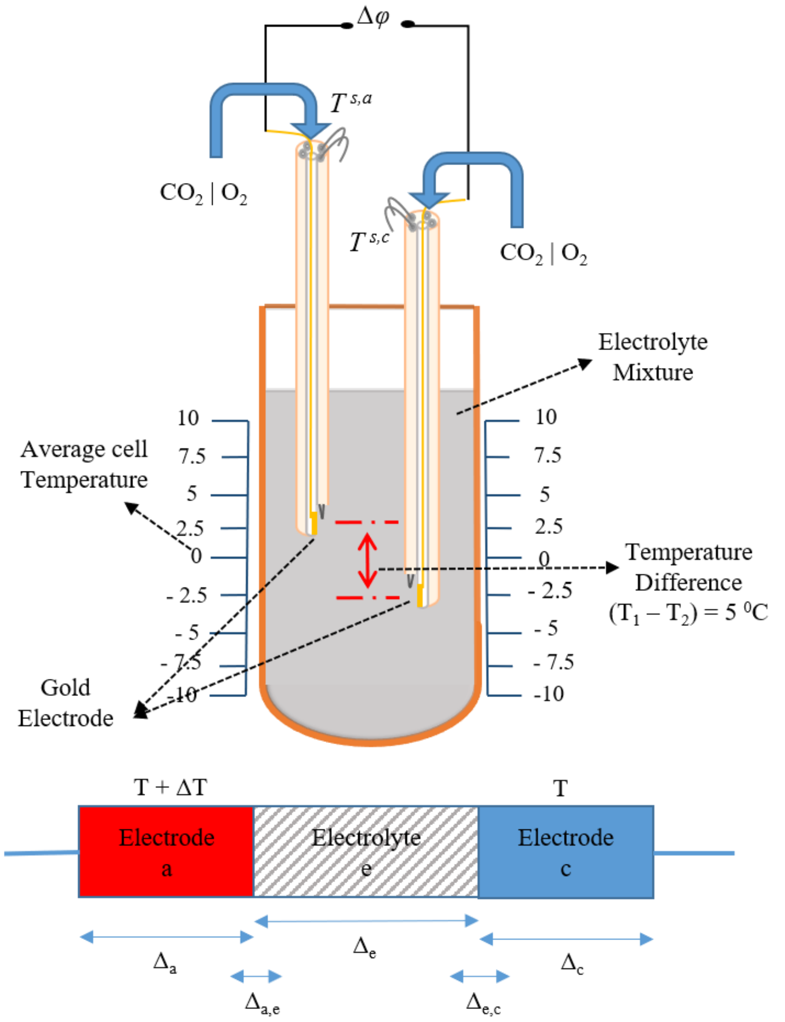
$\Delta\varphi$
$T^{s,a}$
$CO_2 \mid O_2$
$T^{s,c}$
$CO_2 \mid O_2$
Electrolyte Mixture
Average cell Temperature
10
7.5
5
2.5
0
- 2.5
- 5
- 7.5
-10
10
7.5
5
2.5
0
- 2.5
- 5
- 7.5
-10
Temperature Difference
$(T_1 - T_2) = 5\ ^0C$
Gold Electrode
T + ΔT
T
Electrode a
Electrolyte e
Electrode c
Δ_a
Δ_e
Δ_c
$\Delta_{a,e}$
$\Delta_{e,c}$

Figure A1.1 (Top) Cross-sectional view of the thermocell and **(bottom)** the five subsystems of the cell, the notation used for transport properties [28, 63, 68].

A1.2 Seebeck coefficient and non-equilibrium thermodynamics

For simplicity, first we consider the thermocell A containing the pure single molten carbonate (Li_2CO_3) electrolyte and a pair of reversible ($CO_2|O_2$) gas electrode,

Thermocell A:

Au($T^{s,a}$) | CO_2,O_2(g) | *Li_2CO_3* | CO_2,O_2(g) | Au($T^{s,c}$)

The expressions (α_S) for the thermocell A is determined from the non-equilibrium thermodynamics theory for heterogeneous systems.

Then the derivation is extended to obtain the Seebeck coefficient expression for thermocell B containing same ($CO_2|O_2$) gas electrodes but the electrolyte is a mixture of single molten carbonate (Li_2CO_3) with solid oxide (*MO*),

Thermocell B:

Au($T^{s,a}$) | CO_2,O_2(g) | *45 vol% Li_2CO_3(l), 55 vol% MO(s)* | CO_2,O_2(g) | Au($T^{s,c}$)

Finally the expression for Seebeck coefficient for thermocell C is derived by following the expressions for the thermocells A and B.

The thermocell C contains binary eutectic molten carbonates (45 vol% $(Li,Na)_2CO_3$) electrolyte mixed with (55 vol% *MO*), while the electrode gas composition and the pressure remain same to thermocell A and B. For this thesis most of the experiments are conducted with similar electrolyte mixtures in thermocell C,

Thermocell C:

Au($T^{s,a}$) | CO_2,O_2(g) | *45 vol% $(Li,Na)_2CO_3$(l), 55 vol% MO(s)* | CO_2,O_2(g) | Au($T^{s,c}$)

The (*MO*) represents the solid oxides MgO, CeO_2 or $LiAlO_2$. The detail derivation of the Seebeck coefficient (α_S) expressions for the above-mentioned thermocells A-C are established by using the non-equilibrium thermodynamics theory for heterogeneous systems [28, 63, 66, 212, 213].

A1.2.1 Seebeck coefficient of the thermocell A

To estimate the thermoelectric potential of the thermocell, the entropy production and the flux equations for all the subsystems are determined separately. Then by using these equations, the expression for Seebeck coefficient is derived.

The Au metal current collectors

The equations to show the contribution of Au(s) current collectors (Δ_a and Δ_c) for the Seebeck coefficient is well known [212]. The expression for the electric potential is integrated from the temperature of the surroundings, T^0, to the electrode temperature $T^{s,a}$ on the left-hand side, and from the electrode temperature on the right-hand side, $T^{s,c}$, to T^0, the related expression for the Seebeck coefficient,

$$\left(\frac{\Delta_a\varphi + \Delta_c\varphi}{\Delta T}\right) = -\frac{1}{F}S_e^* \tag{A1.4}$$

Here S_e^* is the transported entropy of the electron, it is assumed to be constant in the temperature interval (ΔT).

The electrode surfaces

The equations showing the contribution of the electrode surfaces ($\Delta_{s,a}$ and $\Delta_{s,c}$) at the electrolyte interface is determined. The surfaces ($\Delta_{s,a}$ and $\Delta_{s,c}$) can be regarded as independent thermodynamic systems. The excess entropy production in the anode surface ($\Delta_{s,a}$) has contributions from heat fluxes into and out of the surface, from fluxes of oxygen and carbon dioxide out of the surface, from a flux of lithium carbonate into the surface, from the electric current density across the surface and the electrochemical reaction in the surface,

$$\begin{aligned}\sigma^{s,a} = {} & J_q^{\prime a,e}\Delta_{a,s}\left(\frac{1}{T}\right) + J_q^{\prime e,a}\Delta_{s,e}\left(\frac{1}{T}\right) - \frac{1}{T^{s,a}}J_{O_2}^{e,a}\Delta_{s,e}\mu_{O_2,T}\left(T^{s,a}\right) - \\ & \frac{1}{T^{s,a}}J_{CO_2}^{e,a}\Delta_{s,e}\mu_{CO_2,T}\left(T^{s,a}\right) - \frac{1}{T^{s,a}}J_{Li_2CO_3}^{e,a}\Delta_{s,e}\mu_{Li_2CO_3,T}\left(T^{s,a}\right) - \frac{1}{T^{s,a}}j\,\Delta_{a,e}\varphi - \\ & r^s\left(-\frac{1}{T^{s,a}}\Delta_n G^{s,a}\right)\end{aligned} \tag{A1.5}$$

Here J_q' is the measurable heat flux and J_j is the flux of component j, $\mu_{j,T}$ is the chemical potential of component j evaluated at constant temperature T, j is the electric current density and $\Delta_{a,e}\varphi$ is the potential drop across the surface. With thermostatted electrodes, we have constant temperature across each surface (i.e. for s,a we have $T^{a,e} = T^{s,a} = T^{e,a}$). We assume also chemical equilibrium for adsorbed components (i.e. $\mu_j^{s,a} = \mu_j^{e,a}$). Both conditions apply to reversible conditions ($\sigma^{s,a} = 0$). We measure the emf when a very small electric current is passing the electrode, and the surface reaction rate is $r^s = j/F$.

For $\sigma^{s,a} = 0$ the potential drop across the anode surface is,

$$\Delta_{a,e}\varphi = -\frac{1}{F}\Delta_n G^{s,a} \tag{A1.6}$$

Here $\Delta_n G^{s,a}$ has contributions from the neutral gas components CO_2 and O_2 to the electrode reaction,

$$\Delta_{\mathrm{n}} G^{s,a} = \frac{1}{2}\mu_{CO_2}^{s,a}\ (T^{s,a}) + \frac{1}{4}\mu_{O_2}^{s,a}\ (T^{s,a}) \tag{A1.7}$$

By using (A1.7) in (A1.6), the expression for the potential drop across the anode surface in terms of the chemical potentials of the neutral components is written as

$$\Delta_{\mathrm{a,e}}\varphi = -\frac{1}{\mathrm{F}}\left(\frac{1}{2}\mu_{CO_2}^{s,a}\ (T^{s,a}) + \frac{1}{4}\mu_{O_2}^{s,a}\ (T^{s,a})\right) \tag{A1.8}$$

The same analysis applies to the other electrode surface and the total contribution from the electrode reactions to the cell potential can be written as,

$$\begin{aligned}\Delta_{\mathrm{a,e}}\varphi + \Delta_{\mathrm{c,e}}\varphi &= -\frac{1}{\mathrm{F}}\left[\frac{1}{2}\left(\mu_{CO_2}^{s,a}\ (T^{s,a}) - \mu_{CO_2}^{s,c}\ (T^{s,c})\right) + \frac{1}{4}\left(\mu_{O_2}^{s,a}\ (T^{s,a}) - \mu_{O_2}^{s,c}\ (T^{s,c})\right)\right] \\ &= -\frac{1}{\mathrm{F}}\left[\frac{1}{2}\ S_{CO_2} + \frac{1}{4}S_{O_2}(T^{s,c} - T^{s,a})\right]\end{aligned} \tag{A1.9}$$

Using the relation $(\partial\mu_j/\ \partial\mathrm{T})_{p,n_i} = -S_j$, the last equality is obtained. We shall evaluate S_j for the average cell temperature. The contribution from the electrodes surface to the Seebeck coefficient is,

$$\left(\frac{\Delta_{\mathrm{a,e}}\varphi + \Delta_{\mathrm{c,e}}\varphi}{\Delta\mathrm{T}}\right) = -\frac{1}{F}\left(\frac{1}{2}\ S_{CO_2} + \frac{1}{4}S_{O_2}\right) \tag{A1.10}$$

Here, the S_{CO_2} and S_{O_2} are the entropy of the electrode gases ($CO_2|O_2$) and F is Faraday's constant.

Electrolyte pure lithium carbonate

Since the electrolyte is pure molten lithium carbonate and the pressure is constant throughout the system. Then the only two thermodynamic forces like thermal force and gradient in electric potential contribution to the entropy production in the electrolyte (Δ_e). The entropy production is,

$$\sigma^e = J_q^{\prime e}\left(\frac{\partial}{\partial\mathrm{x}}\frac{1}{\mathrm{T}}\right) + j\left(-\frac{1}{\mathrm{T}}\frac{\partial\varphi}{\partial\mathrm{x}}\right) \tag{A1.11}$$

The flux equations for transport of heat and charge in the electrolyte follow from the entropy production can be written as,

$$J_q^{\prime e} = L_{qq}^e\left(-\frac{1}{T^2}\frac{\mathrm{dT}}{\mathrm{dx}}\right) + L_{q\varphi}^e\left(-\frac{1}{\mathrm{T}}\frac{\mathrm{d}\varphi}{\mathrm{dx}}\right) \tag{A1.12}$$

$$j = L_{\varphi q}^e\left(-\frac{1}{T^2}\frac{\mathrm{dT}}{\mathrm{dx}}\right) + L_{\varphi\varphi}^e\left(-\frac{1}{\mathrm{T}}\frac{\mathrm{d}\varphi}{\mathrm{dx}}\right) \tag{A1.13}$$

The coefficients (L's) depend on state variables but are independent of the forces. They are related through the Onsager relations as $L_{q\varphi} = L_{\varphi q}$. The coefficients are phenomenological and must therefore be determined from experiments. The equation (A1.13) is solved for $\frac{\mathrm{d}\varphi}{\mathrm{dx}}$ by integrate across the electrolyte for $j \approx 0$, and express for the contribution of the electrolyte to the Seebeck coefficient is obtained

$$\left(\frac{\Delta_{\mathrm{e}}\varphi}{\Delta \mathrm{T}}\right) = -\frac{\pi^e}{TF} \tag{A1.14}$$

The ratio $\frac{\pi^e}{T}$ is constant over the temperature interval. The Peltier coefficient (π^e) of the electrolyte describes the heat transported with the current at uniform temperature and composition (*i.e.* at *reversible* conditions),

$$\pi^e \equiv \left(\frac{J_q'^e}{j/F}\right)_{dT=0, d\mu_T=0} = F\frac{L_{q\varphi}}{L_{\varphi\varphi}} = \left(\frac{T(J_S^e - S_{Li_2CO_3} J_{Li_2CO_3})}{j/F}\right)_{dT=0, d\mu_T=0} \tag{A1.15}$$

where J_S^e is the entropy flux in absence of a flux of Li_2CO_3 when the charge is transported in the electrolyte. The transference coefficient of Li_2CO_3 is defined as,

$$t_{Li_2CO_3} \equiv \left(\frac{J_{Li_2CO_3}}{j/F}\right)_{dT=0, d\mu_T=0} = \frac{L_{q\varphi}^e}{L_{\varphi\varphi}^e} \tag{A1.16}$$

In a cation frame of reference $t_{Li^+} = 0$, the transport number of the carbonate ion is unity and the transference coefficient of the salt, $t_{Li_2CO_3} = 0$. Then, all entropy, or equivalently, heat is transported by the carbonate ion and the Peltier coefficient can be expressed by the transported entropy of the carbonate ion, like

$$\pi^e = -T\frac{1}{2}S_{CO_3^{2-}}^* \tag{A1.17}$$

Here the convention used for transport of charge gives the minus sign. In an anion frame of reference $t_{CO_3^{2-}} = 0$, the transport number of the lithium ion is unity and the transference coefficient $t_{Li_2CO_3} = 1/2$.

Then the Peltier coefficient equals the difference between the entropy transported with Li^+, $S_{Li^+}^*$, and the entropy transferred with Li_2CO_3,

$$\pi^e = T\left(S_{Li^+}^* - \frac{1}{2}S_{Li_2CO_3}\right) \tag{A1.18}$$

From (A1.17 and A1.18) transported entropy of the ions and the thermodynamic entropy of the Li_2CO_3 is related as

$$S^*_{CO_3^{2-}} + 2S^*_{Li^+} = S_{Li_2CO_3} \tag{A1.19}$$

The expression for Seebeck coefficient in Thermocells A

Summing up the contribution from the five subsystems, the Seebeck coefficient of the thermocell A is expressed as,

$$\begin{aligned}\alpha_S &= \left(\frac{\Delta\varphi}{\Delta T}\right)\\ &= -\frac{1}{F}\left[\frac{1}{2}\,S^0_{CO_2} + \frac{1}{4}\,S^0_{O_2} - \frac{R}{2}\,lnp^u_{CO_2} - \frac{R}{4}\,lnp^u_{O_2} - \left(\frac{1}{2}\,S^*_{CO_3^{2-}} - S^*_{e,Au}\right)\right]\end{aligned} \tag{A1.20}$$

The cation frame of reference for the electrolyte is chosen. However, at reversible conditions, the choice of frame of reference for the mass fluxes will not have an impact on the expression for the potential drop across the surface. Also, by assuming the ideal gas and used the relation $S_j = S_j^0 + lnp_j^u$ for the entropies of the gases.

The p_j^u is the fraction of the partial pressure and the standard pressure p^0 of component j and S_j^0 is the partial molar entropy of component j at temperature T and standard pressure p^0. The entropies and the transported entropies are generally functions of temperature. The transported entropy of the carbonate ion can be calculated by known the values of the entropies, the gas partial pressures and the transported entropy of the electron in gold current collector.

A1.2.2 Seebeck coefficient of the thermocell B

In thermocell B, the metal current collector and electrode gas composition are identical to the thermocell A. Then the Seebeck coefficient expression by the contribution of the current collector (Δ_a and Δ_c) and its surface ($\Delta_{s,a}$ and $\Delta_{s,c}$) will be same as thermocell A. The contribution from the electrolyte (Δ_e) to the Seebeck coefficient may vary in thermocell B, which will be discussed.

Electrolyte mixture with lithium carbonate and solid oxide

According to the Gibbs phase rule, as long as the solid phase of solid oxides (*MO*) exists there is only one *independent* component. Then the chemical potential of *MO*(s) is $\left(\mu_{\mathrm{MO,T}}\,(s) = \mu^0_{\mathrm{MO,T}}(s)\right)$. Combining the Gibbs-Duhem relation for electrolyte $\left(\mathrm{n_1 d\mu_{1,T}} + \mathrm{n_2 d\mu_{2,T}} = 0\right)$; $d\mu_{Li_2CO_3,T} = \mathrm{d\mu_{1,T}} = -\,\mathrm{n_2 d\mu_{2,T}}\,/\mathrm{n_1}$.

Therefore, the expression for the entropy production will be the same as the entropy production for the pure lithium carbonate electrolyte (thermocell A). This gives the same expression for the Seebeck coefficient for thermocell A and B. Thus, the presence of the solid *MO* in the electrolyte will have no effect on the theoretical expression of the Seebeck coefficient but will change the value of the coefficient, even its solubility is negligible. The addition of oxide could affect the solubility of the gas in the electrolyte, however, only the gas state of carbon dioxide and oxygen enters the overall electrochemical reaction.

A1.2.3 Seebeck coefficient of the thermocell C

As well as in thermocell C the metal current collector and electrode gas composition are identical to the thermocell A and B. Then the expression for the contribution of the current collector (Δ_a and Δ_c) is same as thermocell A. The change in contribution from the current collector ($\Delta_{s,a}$ and $\Delta_{s,c}$) and electrolyte (Δ_e) to the Seebeck coefficient in thermocell C will be derived.

The electrode surfaces

The excess entropy production in the anode surface (s,a) has contributions from heat fluxes into and out of the surface, from fluxes of O_2 and CO_2 out of the surface, from a flux of eutectic $(Li,Na)_2CO_3$ salt into the surface, from the electric current density across the surface and the electrochemical reaction in the surface.

$$\begin{aligned}\sigma^{s,a} = {} & J_q^{\prime a,e}\Delta_{\mathrm{a,s}}\left(\frac{1}{\mathrm{T}}\right) + J_q^{\prime e,a}\Delta_{\mathrm{s,e}}\left(\frac{1}{\mathrm{T}}\right) - \frac{1}{\mathrm{T}^{s,a}}J_{O_2}^{e,a}\Delta_{\mathrm{s,e}}\mu_{O_2,T}\,(T^{s,a}) - \\ & \frac{1}{\mathrm{T}^{s,a}}J_{CO_2}^{e,a}\Delta_{\mathrm{s,e}}\mu_{CO_2,T}\,(T^{s,a}) - \frac{1}{\mathrm{T}^{s,a}}J_{Li_2CO_3}^{e,a}\Delta_{\mathrm{s,e}}\mu_{Li_2CO_3,T}\,(T^{s,a}) - \\ & \frac{1}{\mathrm{T}^{s,a}}J_{Li_2CO_3}^{e,a}\Delta_{\mathrm{s,e}}\mu_{Na_2CO_3,T}\,(T^{s,a}) - \frac{1}{\mathrm{T}^{s,a}}j\ \Delta_{\mathrm{a,e}}\varphi - r^s\left(-\frac{1}{\mathrm{T}^{s,a}}\Delta_{\mathrm{n}}G^{s,a}\right)\end{aligned} \quad \text{(A1.21)}$$

Appling the same process as in (A1.6 – A1.8) and combining the contribution from the other electrode surface, the contribution of the electrode surfaces to the thermocell Seebeck coefficient is,

$$\left(\frac{\Delta_{\mathrm{a,e}}\varphi + \Delta_{\mathrm{c,e}}\varphi}{\Delta\mathrm{T}}\right) = -\frac{1}{F}\left(\frac{1}{2}\ S_{CO_2} + \frac{1}{4}S_{O_2}\right) \quad \text{(A1.22)}$$

Electrolyte mixture with binary (Li, Na) carbonate and solid *MO*

The entropy production is the sum of the products of the conjugate fluxes and forces in the system. The electrolyte is a mixture of three components: Li_2CO_3, Na_2CO_3 and solid phase *MO* (MgO or $LiAlO_2$ or CeO_2 or Al_2O_3). As mentioned in electrolyte contribution for thermocell B, the *MO* has a constant chemical potential since it is present in the solid phase and does not contribute to the entropy production.

The O_2 and CO_2 gas can dissolve in the electrolyte, however the partial pressures of the gases are constant throughout the system. So, it does not contribute to the entropy production. Then the entropy production in the electrolyte is,

$$\sigma^e = J'^e_q \left(\frac{\partial}{\partial \mathrm{x}}\frac{1}{\mathrm{T}}\right) + J_1\left(-\frac{1}{\mathrm{T}}\frac{\partial \mu_{Li_2CO_3,T}}{\partial \mathrm{x}}\right) + J_2\left(\frac{m_2}{m_1}\frac{1}{\mathrm{T}}\frac{\partial \mu_{Na_2CO_3,T}}{\partial \mathrm{x}}\right) + j\left(-\frac{1}{\mathrm{T}}\frac{\partial \varphi}{\partial \mathrm{x}}\right)$$

$$= J'^e_q \left(\frac{\partial}{\partial \mathrm{x}}\frac{1}{\mathrm{T}}\right) + J_{21}\left(-\frac{m_2}{\mathrm{T}}\frac{\partial \mu_{Na_2CO_3,T}}{\partial \mathrm{x}}\right) + j\left(-\frac{1}{\mathrm{T}}\frac{\partial \varphi}{\partial \mathrm{x}}\right) \tag{A1.23}$$

The mole fractions are $m_2 = m_{Na_2CO_3} = \frac{n_{Na_2CO_3}}{n_{Li_2CO_3} + n_{Na_2CO_3}}$ and $m_1 = 1 - m_2$. The flux J_{21} is the flux of Na_2CO_3 relative to the flux of Li_2CO_3, each weighted by the respective mole fraction. The second term on the right-hand side describes the energy dissipated by inter-diffusion of the components.

From (A1.23), the flux equations for transport of heat, mass and charge in the electrolyte is,

$$J'^e_q = L^e_{qq}\left(-\frac{1}{T^2}\frac{\mathrm{dT}}{\mathrm{dx}}\right) + L^e_{q\mu}\left(-\frac{m_2}{\mathrm{T}}\frac{\mathrm{d}\mu_{Na_2CO_3,T}}{\mathrm{dx}}\right) + L^e_{q\varphi}\left(-\frac{1}{\mathrm{T}}\frac{\mathrm{d}\varphi}{\mathrm{dx}}\right) \tag{A1.24}$$

$$J_{21} = L^e_{\mu q}\left(-\frac{1}{T^2}\frac{\mathrm{dT}}{\mathrm{dx}}\right) + L^e_{\mu\mu}\left(-\frac{m_2}{\mathrm{T}}\frac{\mathrm{d}\mu_{Na_2CO_3,T}}{\mathrm{dx}}\right) + L^e_{\mu\varphi}\left(-\frac{1}{\mathrm{T}}\frac{\mathrm{d}\varphi}{\mathrm{dx}}\right) \tag{A1.25}$$

$$j = L^e_{\varphi q}\left(-\frac{1}{T^2}\frac{\mathrm{dT}}{\mathrm{dx}}\right) + L^e_{\varphi\mu}\left(-\frac{m_2}{\mathrm{T}}\frac{\mathrm{d}\mu_{Na_2CO_3,T}}{\mathrm{dx}}\right) + L^e_{\varphi\varphi}\left(-\frac{1}{\mathrm{T}}\frac{\mathrm{d}\varphi}{\mathrm{dx}}\right) \tag{A1.26}$$

The coefficients (*L*'s) depend on state variables but are independent of the forces. They are related through the Onsager relations as $\mathrm{L_{ij}} = \mathrm{L_{ji}}$. From (A1.26) the gradient in the electric potential, at any time can be expressed as

$$\left(\frac{d\varphi}{\mathrm{dx}}\right) = -\frac{\pi^e}{TF}\frac{\mathrm{dT}}{\mathrm{dx}} - \frac{t_{21}}{F} m_2 \frac{\mathrm{d}\mu_{Na_2CO_3,T}}{\mathrm{dx}} - r^e j \tag{A1.27}$$

where π^e is the Peltier coefficient of the electrolyte, t_{21} is the transference coefficient connected with the relative flux J_{21} and r^e is the electrical resistivity of the electrolyte. In (A1.27) the gradient terms may vary with time due to thermal diffusion. The Peltier coefficient is defined as the heat transported *reversibly* with the current

$$\pi^e \equiv \left(\frac{J'^e_q}{\frac{j}{F}}\right)_{dT=0, d\mu_T=0} = F\frac{L^e_{q\varphi}}{L^e_{\varphi\varphi}}$$

$$= \left(\frac{T(J^e_S - (S_{Li_2CO_3} J_{Li_2CO_3} + S_{Na_2CO_3} J_{Na_2CO_3}\ )}{j/F}\right)_{dT=0, d\mu_T=0} \tag{A1.28}$$

The measurable heat flux is expressed in term of the entropy flux J_S^e. Then the transference coefficient is the moles transferred per mole electric charge.

$$t_{21} \equiv \left(\frac{J_{21}}{j/F}\right)_{dT=0,d\mu_T=0} = \left(\frac{t_2}{m_2} - \frac{t_1}{m_1}\right) = F\,\frac{L^e_{q\varphi}}{L^e_{\varphi\varphi}} \qquad \text{(A1.29)}$$

where the coefficients t_2 and t_1 are, respectively, the transference coefficients of Na_2CO_3 and Li_2CO_3. In a mixture of uniform composition (i.e. at initial time) $d\mu_{2,T} = d\mu_{1,T} = 0$.

Integrating the equation (A1.27) across the electrolyte, from $T^{s,a}$ to $T^{s,c}$ at $j \approx 0$, the expression shows the contribution from the electrolyte to the Seebeck coefficient at an initial time (indicated by $t = 0$) is obtained as

$$\left(\frac{\Delta_e\varphi}{\Delta T}\right)_{t=0} = -\frac{\pi^e}{TF} \qquad \text{(A1.30)}$$

The ratio $\frac{\pi^e}{T}$ is constant over the temperature interval. A stationary state will develop, with a balance between the chemical and the thermal driving force. This is called *Soret equilibrium*.

The stationary state condition gives $J_2 = J_1 = J_{21} = 0$, and the emf measurement has $j \approx 0$. Then the balance condition determined from (A1.25) is

$$-m_2\,\frac{d\mu_{Na_2CO_3,T}}{dx} = \frac{q^*}{T}\frac{dT}{dx} \qquad \text{(A1.31)}$$

where the q^* is the heat of transfer due to the *inter-diffusion* of Na_2CO_3 and Li_2CO_3.

By substituting (A1.31) and (A1.29) into (A1.27) and integrate across the electrolyte for $j \approx 0$. The contribution from the electrolyte to the Seebeck coefficient at stationary state (*Soret equilibrium*, indicated by ∞) is,

$$\left(\frac{\Delta_e\varphi}{\Delta T}\right)_{t=\infty} = -\frac{1}{F}\left(\frac{\pi^e}{T} - \left(\frac{t_2}{m_2} - \frac{t_1}{m_1}\right)\frac{q^*}{T}\right) \qquad \text{(A1.32)}$$

Here we took both ratios π^e/T and q^*/T to be constant across the temperature interval. The ratio q^*/T may be interpreted in terms of enthalpy changes across the layer.

A more explicit expression for the Peltier coefficient (π^e) is determined by using the ionic frame of reference, by the similar way in (A1.17 and A1.18) for pure Li_2CO_3 electrolyte system (thermocell A). Then the contribution for Seebeck coefficient from the electrolyte at uniform composition (initial state) is rewritten as:

$$\left(\frac{\Delta_e\varphi}{\Delta T}\right)_{t=0} = -\frac{1}{F}\left(-\frac{1}{2}S^*_{CO_3^{2-}} + \left(\frac{t_2}{m_2} - \frac{t_1}{m_1}\right)\frac{q^*}{T}\right) \qquad \text{(A1.35)}$$

At Soret equilibrium, the expression for Seebeck coefficient due to the contribution from the electrolyte will be

$$\left(\frac{\Delta_e\varphi}{\Delta T}\right)_{t=\infty} = -\frac{1}{F}\left(-\frac{1}{2}S^*_{CO_3^{2-}}\right) \tag{A1.36}$$

Expression for initial state (short time) Seebeck coefficient in Thermocells C

Summing up the contributions from all the subsystems, the Seebeck coefficient at uniform melt composition (initial state) is,

$$\alpha_{S,0} = \left(\frac{\Delta\varphi}{\Delta T}\right) = -\frac{1}{F}\left[\frac{1}{2}\,S_{CO_2} + \frac{1}{4}\,S_{O_2} + S^*_e - \frac{1}{2}S^*_{CO_3^{2-}} + \left(\frac{t_2}{m_2} - \frac{t_1}{m_1}\right)\frac{q^*}{T}\right] \tag{A1.37}$$

The relation between the transported entropies of the ions are

$$2\left(S^*_{Na^+} - S^*_{Li^+}\right) = S_{Na_2CO_3} - S_{Li_2CO_3} + \left(\frac{t_{Na^+}}{m_2} - \frac{t_{Li^+}}{m_1}\right)\frac{q^*}{T} \tag{A1.38}$$

$$S^*_{CO_3^{2-}} + 2S^*_{Na^+} = S_{Na_2CO_3} + \frac{t_{Na^+}}{m_2}\frac{q^*}{T} \tag{A1.39}$$

$$S^*_{CO_3^{2-}} + 2S^*_{Li^+} = S_{Li_2CO_3} + \frac{t_{Li^+}}{m_1}\frac{q^*}{T} \tag{A1.40}$$

The two terms on the right-hand side in (A1.39 and A1.40) are unique for the two-component system. The entropy of a component in a mixture depends on the composition.

Expression for Soret equilibrium state Seebeck coefficient in Thermocells C

Adding the contributions to the Seebeck coefficient from the five subsystems; obtained the Seebeck coefficient for $J_{21} = 0$ (Soret equilibrium)

$$\alpha_{S,\infty} = \left(\frac{\Delta\varphi}{\Delta T}\right) = -\frac{1}{F}\left[\frac{1}{2}\,S_{CO_2} + \frac{1}{4}\,S_{O_2} + S^*_e - \frac{1}{2}S^*_{CO_3^{2-}}\right] \tag{A1.41}$$

The transported entropy of the carbonate ion is calculated from the measured values of $\alpha_{S,\infty}$, by using the transported entropy of the electron and of the equation of state for the gases.